Satellite Moisture Profiling of Eastern Pacific Moisture Plumes

by
Christopher A. Davey
Thomas H. Vondeer Haar
John M. Forsythe

Department of Atmospheric Science
Colorado State University
Fort Collins, Colorado

Colorado State University

Department of Atmospheric Science

Paper No. 691

Note:

This document is the Master of Science thesis of Christopher A. Davey and was prepared in collaboration with the co-authors.

SATELLITE MOISTURE PROFILING OF EASTERN PACIFIC MOISTURE PLUMES

by

Christopher A. Davey

Department of Atmospheric Science

Colorado State University

Fort Collins, CO 80523

Research supported by NASA

under Grant NAG5-3449

Spring 2000

Atmospheric Science Paper No. 691

ABSTRACT

SATELLITE MOISTURE PROFILING OF EASTERN PACIFIC MOISTURE PLUMES

Moisture plumes, depicted on satellite imagery as long bands of middle and high-level clouds, are common in the eastern Pacific Ocean during the winter and early spring. These plumes occasionally bring heavy precipitation to the west coast of North America. The spatial and temporal characteristics of water vapor in moisture plumes are discussed, using tropospheric relative humidity profiles and cloud properties retrieved from Special Sensor Microwave T-2 sensor observations. A climatology is presented, based on moisture plume activity over the eastern Pacific Ocean during the January-April period of the years 1995-1997. It identifies three classes of moisture plumes and characterizes their spatial and temporal distribution. It is found that moisture plumes occur more frequently in the western portions of the study region and that plume activity differs markedly between January-February and March-April.

The microwave-based Bayesian Water Vapor Retrieval algorithm is then described and used to determine the three-dimensional water vapor distribution for 30 selected case studies of moisture plumes. It is shown that the moisture plume axis typically has very moist conditions throughout the troposphere. A region of primarily upper-level moisture exists to the south and east of the plume axis. To the north and west of the plume axis, the atmosphere is substantial dryer at all levels. Moisture transports are also discussed. The transport associated with a plume is greatest between 500-850 mb. The

average total instantaneous tropospheric moisture transports found within moisture plumes are between 2-3X10^5 $gm^{-1}s^{-1}$. These values are several times greater than those observed in non-plume conditions. Moisture plumes are suggested to have a role in atmospheric moisture transport comparable to that of midlatitude frontal systems.

ACKNOWLEDGMENTS

Many thanks go to my advisor, Dr. Tom Vonder Haar, and committee members, Drs. Graeme Stephens and Jorge Ramirez. I would especially like to thank John Forsythe, for his many hours of technical assistance with this project. This work was sponsored by NASA Grant NAG5-3449 under the Earth Observation System (EOS) Interdisciplinary Working Group (IWG) program, entitled "Water Vapor in the Climate System."

TABLE OF CONTENTS

1. Introduction

Atmospheric tropical-extratropical interactions are an important component of the earth's climate system. Among other things, these interactions are instrumental in the poleward transport of energy and moisture from the tropics (Bjerknes, 1966). During the winter, wave energy from the midlatitude baroclinic zone often propagates equatorward, exciting various convection modes along the Intertropical Convergence Zone, or ITCZ. At the same time, poleward momentum transport from the ITCZ is often occurring in the upper troposphere (Liebmann and Hartmann, 1984; Webster and Dong, 1992). A well-known tropical-extratropical interaction is that of the El Niño-Southern Oscillation (ENSO) cycle and its indirect effects on midlatitude weather patterns (Philander, 1990). Tropical-extratropical interactions are also found with the winter monsoon events over the western Pacific (Liebmann and Hartmann, 1984; Lim and Chang, 1987).

Moisture plumes are also an example of atmospheric tropical-extratropical interactions. These features are often indicated on visible and infrared (IR) satellite imagery as long bands of mid- to high-level clouds, with lengths typically on the order of several thousands of kilometers. The cloud bands commonly originate in the tropics and subtropics, and occasionally join up with the frontal cloud bands associated with mid-latitude storms. During the winter months, moisture plumes are a relatively frequent occurrence along the West Coast of the United States. Moisture plumes frequently play a part in the development of severe weather over the Central and Eastern United States during the spring and summer months (Schroeder, 1983; Thiao et al., 1993). Like the

Hadley cell circulation and midlatitude frontal systems, moisture plumes are also believed to serve as a primary mechanism for the poleward transport of moisture and energy from the tropics (Rasmussen and Arkin, 1993).

This work investigates the characteristics of moisture plumes in the Eastern Pacific (Figure 1.1) during the months of January through April for the years 1995 to 1997. Satellite microwave radiances are used to retrieve vertical profiles of relative humidity, along with cloud liquid and ice water. These data are then combined with meridional and zonal wind data from the National Center for Environmental Prediction (NCEP) reanalysis product to determine the moisture transport characteristics within plumes.

1.1 Previous studies of moisture plumes

1.1.1 Plume development

As early as the middle part of the twentieth century, researchers were interested in the mechanisms that gave rise to enhanced poleward heat and moisture transport from the subtropical and tropical regions. Riehl (1950) observed that poleward heat transport occurred along "narrow strips of longitude" occurring on the eastern sides of pressure troughs which built into the tropics from the middle latitudes. Bjerknes (1966) suggested that enhanced poleward transport occurred as a result of middle and high-cloud blowoff from enhanced tropical convection driven by sea-surface temperature anomalies. Much of the present-day research on moisture plumes began a couple of decades later, when these plumes were first identified by satellites on a routine basis. One of the first studies to detect moisture plumes with satellites was done by Hill (1969), who examined large-scale meridional troughs in the Tasman Sea off of New Zealand. He labeled these features as "cloud sheets." Anderson and Oliver (1970) identified these features on geostationary satellite imagery as "cloud surges". These surges were speculated to

occur when upper tropospheric midlatitude troughs and their associated wind maxima approach and couple with the Intertropical Convergence Zone (ITCZ). This explanation essentially combines the mechanisms for plume development proposed by Riehl and Bjerknes. Other names given to these features include "jet-stream associated cloudbands" (De Felice and Viltard, 1976), "shear bands" (Zwatz-Meise and Hailzl, 1980), and "cirrus surges" (Schroeder, 1983).

The initial identification of moisture plumes on satellite imagery generated much interest in these features, spawning several research efforts that contributed to the understanding of their physical characteristics. Thepenier and Cruette (1981) examined the development of "tropical plumes" (plumes which originate in the tropics and extend to the subtropics or midlatitudes) using Geostationary Operational Environmental Satellite-1 (GOES-1) visible and infrared (IR) imagery, noting their associations with mid-latitude storm development. Kininmonth (1983) looked at moisture plumes over Australia, noting their connection to episodes of heavy precipitation on that continent. Kiladis (1985) found that tropical plumes occurred as low-pressure troughs from the subtropics and midlatitudes interacted with areas of increased convection along the ITCZ, most likely due to tropical waves. The interaction of midlatitude troughs with the ITCZ convection was found to impart momentum/energy to the upper atmosphere, which then intensified the subtropical jet downstream of the interaction and further assisted plume development (Keen, 1984; Kiladis, 1985; Stockton, 1986; Thompson and McGuirk, 1987; McGuirk et al., 1988). Stockton studied tropical plumes using *in situ* and GOES-IR observations from the First GARP Global Experiment-1 (FGGE-1) in 1979. The results from this study corroborated the results presented by Kiladis. It was also found that: 1) anticyclones from the Southern Hemisphere which cross the equator provided another source of troughs; and 2) convection along tropical plumes is caused by a combination of strong upper-level divergence and abundant low-level moisture below the trade wind

inversion. The appearance of tropical plumes and the adjacent synoptic signatures on upper-level water vapor (WV) imagery has been examined (Ulsh, 1988; McGuirk and Ulsh, 1990). In the upper level moisture field, a common signature preceding tropical plume development is a moist trough approaching a moist tropical wave, with the two separated by an anomalously dry subtropical high.

It has been realized that moisture plumes needed to be better handled in forecast models (Scheafer, 1985; Coe, 1992). Some efforts were made to assess the impact of injecting improved moisture plume data, from satellites, into forecast models. McGuirk (1993) made such an attempt with tropical plumes by inputting an improved TOVS (TIROS Operational Vertical Sounder) signal into the National Meteorological Center (NMC) Global Spectral Model, finding positive results in model performance.

In a more recent study, Mecikalski and Tripoli (1998) present an alternative theory for the development of tropical plumes. In many plume examples, the adjacent middle-latitude systems did not extend far enough equatorward for the accompanying dynamically-induced lift to generate the tropical plumes. They suggest instead that the tropical plumes result merely from enhancements of the upper branch of a thermally direct circulation poleward of the ITCZ, due to outbreaks of ITCZ convection. In contrast to previous studies, it is suggested that middle-latitude disturbances may have a less direct influence on plume development. In fact, these middle-latitude disturbances may be connected more to the demise of tropical plumes, rather than their formation.

1.1.2 Plume climatologies

Several climatologies of moisture plumes have been developed which attempt to summarize the characteristics of plumes and their development (Smith, 1985; McGuirk et al., 1987; Kuhnel, 1989; Iskenderian, 1995). Some of the findings are that moisture plumes occur primarily over oceans and that they are generally more common during the

winter months. On an annual basis, moisture plumes are found throughout the world, with the most common locations of occurrence being the central and eastern portions of the north Pacific and north Atlantic Ocean basins (Iskenderian, 1995) as well as the south-central Pacific Ocean (Kuhnel, 1989). Although the majority of research about moisture plume characteristics has focused on tropical plumes, it has been noted that these plumes can take on a variety of forms (McGuirk et al. 1987). This work uses geostationary satellite IR images along with total column water vapor data from the NASA Water Vapor Project (NVAP) to identify and then categorize moisture plumes according to their moisture structures and attendant cloud distributions. Three classes are defined in this work: classic, subtropical, and tropical-polar plumes. A more complete discussion is provided in Chapter 2.

1.1.3 Moisture characteristics

Efforts have been made to determine the spatial and temporal moisture characteristics of plumes (Scheafer, 1985; Stockton, 1986; Thompson and McGuirk, 1987; McGuirk et al., 1988, Ulsh, 1988; McGuirk and Ulsh, 1990). Stockton (1986) concluded that moisture plumes are often characterized by abundant upper-level moisture. The layer of upper-level moisture tends to elevate as one heads along the plume, downstream from its origin. Both upper-level and lower-level moisture is found in areas along the plume where deep convection is occurring, such as areas of upper-level divergence. In areas under the plume where there is no active convection, a dry mid-atmospheric layer often exists between the upper-level moisture and the boundary layer moisture (Figure 1.2). Some studies (Schaefer, 1985; McGuirk et al., 1988) also found a marked drying at all levels of the atmosphere just north and west of the main plume axis.

Little work has been done to study the moisture transports that occur within moisture plumes. Thompson and McGuirk (1987) used a combination of radiosonde and

dropsonde data from the FGGE-II and FGGE-III projects to estimate moisture transport. They were able to see a general poleward flux of moisture inside the plumes they studied. Total tropospheric transport values along the plume axis were on the order of 10^2 $kgm^{-1}s^{-1}$. These results, however, were deemed to be largely inconclusive, due to the questionable handling of the observational data by their analysis model. Hence, an important question still remains. What are the spatial and temporal characteristics of moisture within moisture plumes? In Chapters 4 and 5, this project investigates the preceding question and, along with the findings on plume classes, attempts to determine what the typical moisture characteristics are for each plume class.

Currently, much of the data used for understanding the spatial and temporal characteristics of moisture within moisture plumes has been limited to radiosonde and satellite IR data, with some additional dropsonde data obtained during special projects such as the FGGE experiments. As is generally known, radiosonde data are quite sparse across the eastern subtropical Pacific Ocean and do not provide sufficient observational data coverage for many moisture plume episodes. The use of satellite data helps to extend the observational coverage across data-sparse areas. In the past, IR-based methods have been the primary choice for retrieving the moisture distribution within moisture plumes. These methods, however, have limited usefulness in cloudy regions, since clouds readily absorb at IR wavelengths.

An alternative is to use microwave (MW) radiation, which is briefly discussed in Chapter 3. An advantage of using MW radiation rather than IR radiation is that MW, unlike IR, can pass relatively unimpeded through liquid clouds as well as thin layers of high clouds (Jones, 1989). The only significant MW signal degradation occurs in clouds that have a significant ice content or are heavily precipitating. A main disadvantage of using MW rather than IR is that MW sensors have poorer horizontal resolution, which hinders their ability to detect finer-scale variations in the moisture fields. Also, if sub-

field-of-view sized clouds are not accounted for, they can adversely affect the radiation incident on the MW sensor, leading to errors in radiative transfer calculations (Greenwald et al., 1997). There has been work done in the past few years to devise a retrieval method that combines MW and IR. The cloud-penetrating capabilities of MW are utilized, while the greater horizontal resolution of the IR is used to detect and correct for the fractional cloud amount within the MW scanner field of view (FOV). Lietzke (1998) tested the usefulness of such a method in a study of the tropical eastern Pacific convergence zone. It was determined that over the oceans, the MW + IR method performed no better than methods in which only MW radiation was used.

1.2 Retrieval algorithm application and evaluation

This work is an application of the microwave-only version of the Bayesian Water Vapor Retrieval algorithm (Lietzke, 1998), or BWR, determining the moisture characteristics of moisture plumes in the eastern Pacific Ocean (Figure 1.1). Previous uses of the BWR algorithm have been limited primarily to tropical oceanic regions. For instance, BWR has been used to study occurrences of the double-ITCZ in the tropical eastern Pacific Ocean (Lietzke, 1998; Lietzke et al., 2000). The BWR algorithm has not been used much in extratropical regions such as the subtropics and midlatitudes. The present work makes several modifications to BWR in an effort to ensure its successful use outside the tropics. A more complete description of BWR, including modifications, is presented in Chapter 3. A discussion of the overall performance of the BWR algorithm is given in Chapter 6.

For selected case studies of moisture plumes, the BWR algorithm uses microwave brightness temperatures from the Special Sensor Microwave T-2 instrument to retrieve atmospheric moisture profiles. The retrieved variables of interest are: the relative humidity (RH) values at the surface, 850 mb, 700 mb, 500 mb, 400 mb, and 300 mb,

along with the total column liquid water and ice water contents of clouds. In Chapter 4, the three-dimensional moisture distributions found from these case studies are examined and compared with previous work. Once the relative humidity values are known, specific humidities are derived and are then used, along with wind data from the National Center for Environmental Prediction (NCEP) model reanalysis, to calculate moisture transports for each of the plume case studies.

The moisture transport calculations are presented and discussed in Chapter 5. For each plume class, as defined in Chapter 2, the calculated spatial and temporal moisture characteristics for each case study are summarized. From this, conclusions are made concerning what role moisture plumes play in the poleward transport of moisture from the tropical regions. In Chapter 7, the entire work is summarized and recommendations for future work are provided.

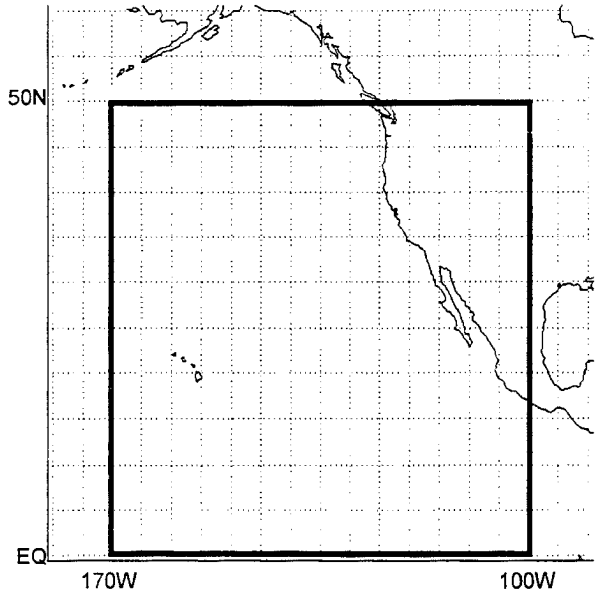

Figure 1.1 Eastern Pacific study region.

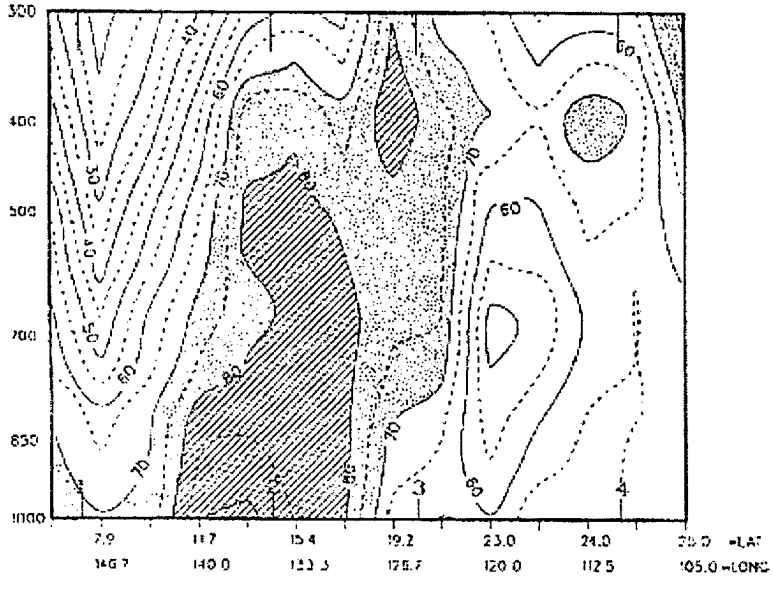

Figure 1.2 Example of a vertical cross section of relative humidity within a moisture plume. Relative humidities (in %) are labeled (after Schaefer, 1985).

2. Plume Climatology

A preliminary objective of this work is to determine and summarize the different forms of moisture plumes. One type of moisture plume that has been widely examined by many groups is the "tropical plume", introduced in Chapter 1. An accepted definition of a Northern Hemispheric tropical plume is a moisture plume with an associated mid- to high-level cloud band which originates equatorward of 15°N latitude and has a length of approximately 2000 km or greater (McGuirk et al., 1987). Within these criteria, tropical plumes do, however, take on a variety of forms. Thus, it may be instructive to further classify tropical plumes, according to certain criteria. For instance: 1) Does the cloud band of a given tropical plume connect directly with a low-pressure system and its associated cloud band? 2) Does the poleward end of the cloud band extend to the subtropics or the midlatitudes? The list could go on. In this section, three separate plume classes are identified and defined. Tropical plumes (i.e. plumes originating < 15°N) are separated as "classic" and "tropical-polar" according to whether their cloud bands' poleward edge is or is not, respectively, directly connected into the cloud band of a midlatitude low-pressure system. For tropical plumes, it is assumed in this work that the region of higher moisture inside the plume is directly connected to tropical moisture equatorward of 15°N latitude. An additional class of moisture plumes which has received little attention is one whose plumes are directly connected with midlatitude troughs and whose cloud bands originate in the subtropics, poleward of 15°N latitude. Plumes that fall under this category are henceforth designated as "subtropical" plumes. This chapter

develops a simple climatology of moisture plume activity for the January-April period of the years 1995-1997. The longitudinal and monthly distributions of activity for each plume class (classic, subtropical, and tropical-polar) are summarized. These results will be used, along with the plume case study results discussed in Chapters 4 and 5, to analyze monthly/seasonal patterns in moisture plume behavior for each plume class. The mean synoptic conditions associated with each class are also mentioned.

2.1 Previous climatologies

Several climatologies of moisture plumes have been developed in the past two decades. Most of these have dealt solely with tropical plumes, which include the "classic" and "tropical-polar" classes. Thepenier and Cruette (1981) produced one of the first climatologies of moisture plumes. They examined tropical plumes over a three-year period of GOES-1 satellite imagery. They concluded that tropical plumes were primarily a cool season (late fall-early spring), synoptic-scale phenomenon. These plumes usually formed on the eastern sides of midlatitude troughs that approached the tropical latitudes from the northwest.

A second climatology (Smith, 1985; McGuirk et al., 1987) was compiled from imagery for 4 cool seasons (Nov.-Apr.), including the 1982-83 El Niño event, and focused specifically on tropical plumes over the northern Pacific Ocean Basin from 160°E-100°W. A tropical plume was defined as a cloud band at least 2000 km in length which originates equatorward of 15°N. It was found that an average of 10 tropical plume events occurred per month, or about 60 events per cool season, with a minimum of activity suggested in February and March. On average, there was at least one tropical plume present in the study region on 71% of the days during the cool season. During the 1982-83 El Niño, a decrease in tropical plume activity was noted and it was suggested

that the frequency of tropical plume occurrence decreases during El Niño events, in accordance with the strengthening of the eastern Pacific Hadley cell (McGuirk et al., 1987). The association of tropical plumes with adjacent midlatitude troughs suggested by Thepenier and Cruette was noted in this study. An examination of 41 tropical plume events over the period of January-April, 1982, found that in all but one case an upper-level pressure trough was present upstream (west or northwest) of the plume cloud band. Two possible subclasses of tropical plumes were also suggested by McGuirk et al. (1987), namely, those that originate as a midlatitude trough and its associated cloudband move equatorward of 15°N, and those that originate from convection in the ITCZ in response to approaching midlatitude troughs.

A more complete climatology was developed by Kuhnel (1989), who examined the global distribution of tropical plumes using IR imagery from the TIROS-N/NOAA satellite series over the period 1979-1983. Kuhnel established a set of criteria for the definition of a Northern Hemispheric tropical plume similar to those developed by McGuirk et al. (1987). The main difference was that the southern latitude boundary was set at 20°N rather than 15°N. It was found that tropical plume activity was generally greatest along the western edges of ocean basins, especially for the Pacific and Atlantic Ocean basins, with 50-80 plume events per cool season. The eastern North Pacific Ocean basin (100°W-155°W) was equally active, with about 70 events per cool season. The connection between the Southern Oscillation Index (SOI) and tropical plume frequency was examined for all regions. Of particular note is the observation by Kuhnel that the eastern North Pacific region had a positive correlation with SOI, indicating a decrease in plume activity during El Niño events. This result corroborates the results found by McGuirk et al. (1987).

In a more recent tropical plume climatology (Iskenderian, 1995), only the Northern Hemisphere was considered. Tropical plumes were examined over the October-May period of the years 1974-1984. The plume criteria used were identical to those used by Kuhnel (1989). As with previous studies, an association of tropical plumes with midlatitude troughs extending into the tropics and subtropics was noted. It was found that the preferred longitudinal zones of plume activity were in the central and eastern oceanic regions. This differs from Kuhnel (1989), who found that the preferred longitudinal zones for development were in the western portions of ocean basins. In the eastern Pacific, Iskenderian reported an average of about 40 plumes per season, a value somewhat lower than in previous studies. In agreement with the results of McGuirk et al. (1987), Iskenderian found a minimum in Northern Hemisphere tropical plume activity during the months of February and March, as well as a minimum in activity during El Niño events. Iskenderian presented a hypothesis for the February-March minimum in plume activity, proposing that since the ITCZ reaches its southernmost extent during this period, Northern Hemisphere midlatitude troughs generally did not extend far enough south to initiate the interactions with the ITCZ necessary to generate tropical plumes. Iskenderian also examined the general synoptic conditions associated with plume development over the eastern Pacific Ocean. The main features observed were a strong jet extending from Asia out to the International Date Line, with a strong Rex block (Rex, 1952), or a high pressure center positioned north of a low pressure center, in the eastern Pacific Ocean.

2.2 Climatology development

2.2.1 Plume identification

The definitions for the moisture plume classes discussed here were based largely on satellite imagery. In this project, plumes were identified using IR images from the 11.7 μm channel on the Geostationary Operational Environmental Satellite (GOES) West (GOES-7, 1995-January 1996; GOES-9, January 1996-1997) International Satellite Cloud Climatology Project (ISCCP) archive. Plumes are characterized by long bands (~2000 km length) of predominantly mid- and high-level clouds. Maps of total column water vapor from the NASA Water Vapor Project (NVAP) were also used in the identification process, primarily to help identify the longitudes of the origins (i.e. equatorward end) of the identified plumes. These NVAP data are also used to compare values of total column water vapor with those calculated by BWR (see Chapter 6).

2.2.2 Plume class definition

Based on the appearance of the plumes identified in the GOES and NVAP datasets, three classes of moisture plumes are defined: classic, subtropical, and tropical-polar plumes. Table 2.1 provides a summary of the criteria for each plume class. A "classic" plume (Figure 2.1) is defined as a moisture plume which has a length of at least 2000 km, originates equatorward of 15°N, and does not merge directly with the frontal cloud band of a midlatitude trough. In some instances, these plumes may extend poleward of 30°N. The cloud bands associated with classic plumes often display an anticyclonic curvature and form in the region between midlatitude and subtropical troughs approaching from the north and west, and subtropical anticyclones to the east. These plumes may sometimes connect directly with subtropical lows (i.e. low-pressure centers

positioned between 15°N-30°N latitude) and are often a manifestation of a strengthened subtropical jet stream downwind of the approaching troughs.

A "subtropical" plume (Figure 2.2) is defined as a moisture plume which has a length of at least 2000 km and originates between the latitudes of 15°N-30°N. In almost all cases, the cloud bands of these moisture plumes are merely the frontal cloud bands associated with midlatitude troughs that have built into the subtropical regions. Although the above definition also includes moisture plumes that lie entirely within the 15°N-30°N latitudinal zone, no such plumes were observed in this present work.

Finally, a "tropical-polar" plume (Figure 2.3) is a moisture plume which has a length of at least 2000 km, originates equatorward of 15°N, and, unlike classic plumes, is directly connected with the frontal cloud band associated with a midlatitude trough. In many cases, tropical-polar plumes form as a classic plume builds poleward and connects with a midlatitude trough. Subtropical and classic plumes can also combine in this manner to form a tropical-polar plume. The tropical-polar plume is the least common of the three classes mentioned here.

2.2.3 Method

Once the plume class definitions were developed (Table 2.1), GOES and NVAP data were again used to identify and classify the moisture plumes that occurred in the study region (Figure 1.1) during the period of January-April, 1995-1997. To facilitate the identification/classification of the moisture plumes, the study region was divided into 7 longitudinal bins, each 10° wide. Plumes were counted daily over the study period; on a given day, a plume was counted for a particular longitudinal bin if the plume's origin occurred within that bin.

2.3 Results

2.3.1 Space-time dependence

In order to determine monthly variations during the January-April period in the longitudinal distribution of moisture plumes within the study region (Figure 1.1), a set of tables of plume counts per month per 10° longitudinal bin was constructed for each plume class. This set consisted of three tables, one for each year (1995, 1996, 1997), along with the average and standard deviation of these three years. Before discussing any results, however, it should be noted that only three years were used in this analysis. In order to more accurately represent the longer-term characteristics of each class, more years must be considered.

The January-April period seems to exhibit two distinct modes of activity for classic plumes (Tables 2.2-2.4). During January and February, the plumes are quite common in the eastern half of the study region (100°W-140°W), with little activity to the west. For reasons which are unclear, the center of maximum activity gradually shifts westward throughout the period, so that by March and April, classic plumes are more common in the western portion of the study region (140°W-170°W). This pattern is most evident for the January-April period in 1995 (Table 2.2), where a maximum of 8 plume counts occurs in February at the longitude bin 110°W-120°W, while a second maximum of 9 counts occurs in April for the 140°W-150°W longitudinal bin. The 1995-1997 mean data (Table 2.5) also shows this pattern, with a January-February maximum of 5 to 6 counts per month within the 120°W-130°W longitude bin and a March-April maximum of 6-7 counts spread evenly between 140°W-160°W.

In 1997, however, this pattern is not evident at all (Table 2.4). The zone of maximum plume activity remains in the western half (140°W-170°W) of the study region during the

entire January-April period, with the greatest activity (up to 9 counts per month) occurring during both March and April. The pattern exhibited in 1997 may have been influenced by the El Niño event that was developing during the 1996-97 winter.

The regions with the highest observed plume activity are also the regions that exhibit the highest variability in plume activity (Table 2.6). This relationship was also observes for the other two plume classes (Tables 2.11, 2.16). More years of data could be analyzed in order to smooth out some of this variability.

The activity of subtropical plumes was generally found to be much greater in the western half of the study region during the entire season (January-April), with the greatest activity occurring during January and February (Tables 2.7-2.9). The 1995-1997 mean data (Table 2.10) indicates a maximum of 6-7 counts per month during January-February, between 140°W-160°W. A second maximum of 5-6 counts is indicated during March, around 130°W-140°W. By April, the activity drops off substantially (3-4 counts per month to the west and 1-2 counts per month to the east) across the entire study region, with the greatest activity (4-5 counts per month) around 150°W-160°W. In 1995 (Table 2.7), the two early-season maxima are readily apparent. The first maximum occurred during February in the 140°W-160°W longitudinal range, with up to 12 counts per month, while the second maximum occurred in March at the 130°W-140°W bin, also with 11 counts per month. These maxima are also apparent in 1996 (Table 2.8), although the general pattern is shifted back by roughly one month. The first maximum occurs in January at 9 counts per month, while the second maximum occurs in February at 8 counts per month.

In the eastern part of the study region, there is a subtropical plume activity maximum which, although quite a bit smaller in magnitude than the maxima found in the western half of the region, is still worthy of note. This maximum occurs around February at the

110°W-120°W bin and averages about 3-4 counts (Table 2.10). In all three years (1995-1997), this maximum seems to be a persistent feature, as indicated by the relatively low standard deviation values seen here (Table 2.11; about 1 plume count per month). The cause of this activity maximum is not clear.

The pattern of subtropical plume activity during January-April, 1997 (Table 2.9) is markedly different from the 1995 and 1996 patterns (Tables 2.7 and 2.8, respectively). Again, this may be due to the El Niño event that was developing during the 1996-97 winter. In January, a maximum of 9 plume counts per month is observed between 150°W-160°W, but activity drops off rapidly after January. Unlike 1995 and 1996, there is no second maximum observed around 130°W-140°W during February-March. Activity did increase substantially around 150°W during late March and into April, This is a pattern which was not found in 1995 or 1996, although increased activity (about 6 counts) was observed in April 1996 between 150°W-160°W.

Out of the three plume classes defined in this chapter, the tropical-polar plume is by far the least common (Table 2.15). The observed activity is largely confined to the western part of the study region, between 140°W-170°W. In general, the greatest observed monthly plume activity is between 2-3 counts, although there are exceptions. For instance, in February 1996 (Table 2.13), a maximum of 9 plume counts was observed between 150°W-160°W. Due to the smaller number of tropical-polar plume observations (and correspondingly high variability in space and time; see Table 2.16), very little can be concluded about tropical-polar plume distributions during the January-April period.

2.3.2 Spatial, temporal composites

The results presented in Section 2.3.1 are summarized further by developing a series of both longitudinal and temporal composites. The longitudinal composites were produced by averaging the plume counts from each of the longitudinal bins, producing a plot of plume counts as a function of month. To produce a temporal composite, the plume counts for each month can be averaged over the time period of interest to obtain an average plume count as a function of longitude (or longitudinal bin).

First, for each class, the monthly variations of plume count distributions over the entire study region were examined. Attempts were made to analyze these distributions for each month (January, February, March, and April) separately. However, the results were largely inconclusive. Instead, the study period (January-April) was divided into two periods, January-February and March-April, and temporal composites were produced for each class for both of the periods.

The longitudinal distributions of classic plume activity for these two periods are shown in Figure 2.4. The January-February period (Figure 2.4a) shows an average (1995-1997) maximum of 9 plume counts in the eastern half of the study region, between 120°W-140°W. This eastern concentration of activity is most pronounced in 1995. The maximum activity for 1996 is shifted west from the 1995-1997 average to the 130°W-140°W bin. At 16 plume counts per month, the 1996 season had the greatest activity observed for January-February. This plot indicates more clearly that the average maximum, being between 120°W-130°W longitude, is tending towards the middle of the study region. During March and April, this maximum shifts decidedly to the western half of the study region, where an average maximum of 11 plume counts per month occurs between 140°W-160°W (Figure 2.4b). The general pattern of an eastern maximum in January-February and a western maximum in March-April is not evident in 1997, where

the count maximum remains in the western half of the study region. This trend is also seen in Table 2.4.

Subtropical plumes (Figure 2.5) are most active in the western parts of the study region throughout the entire study period (January-April). The 1995-1997 average location of maximum activity for January-February is at 150°W-160°W, with 13 counts per month. For March and April, this maximum persists, although smaller in magnitude at 9 counts per month. Also evident during March and April is a second maximum of 8 counts per month near 130°W-140°W, which seems to be influenced largely by the activity maxima from both 1995 and 1996. Overall, the greatest subtropical plume activity was in 1995, with a maximum of 17 counts per month between 140°W-150°W for January-February and a maximum of 14 counts per month between 130°W-140°W during March-April.

Figure 2.6 gives the January-February and March-April composites for tropical-polar plumes. The 1995-1997 average for the January-February period (Figure 2.6a) indicates a maximum of about 7 plume counts per month centered on 140°W-150°W. Almost all of the plume activity during January-February is confined primarily to the western half of the study region, while the March-April period is uniformly active (about 1-3 plume counts per month) across the entire study region. The greatest overall tropical-polar plume activity was during January-February 1996, with 13 counts per month at 150°W-160°W.

Finally, a summary of plume activity in each class is shown in Figures 2.7 and 2.8. Figure 2.7 shows the 1995-1997 average of total plume counts over the January-April period for each longitudinal bin, while Figure 2.8 shows the 1995-1997 average of total plume counts over the entire study region for each month.

Both of the subtropical and tropical-polar plume classes display a marked difference in overall activity between the eastern and western portions of the study region (Figure 2.7). A sharp increase in activity is observed for both classes as one heads from east to west. The average peak in subtropical plume activity occurs at 150°W-160°W, with over 20 counts on average between January-April. The average peak in tropical-polar plume activity occurs at 140°W-150°W, with about 5-10 counts between January-April. The activity distribution of classic plumes differs a bit from the other two classes in that the plume activity peaks towards the middle of the study region. The maximum activity for classic plumes, with a little over 15 counts per month, occurred within the 140°W-150°W bin.

Figure 2.8 summarizes the total monthly plume counts, averaged over the study region, for each class. Subtropical plumes appear to be most frequently observed of the three plume classes, especially during the months of January and February. March and April tend to bring a decrease in subtropical activity, with an activity comparable to that of the classic plumes. Subtropical plumes are most active in the month of February, with a 1995-1997 average of about 30 counts over the study region.

The combined results for the classic and tropical-polar plumes are also examined. Both are types of tropical plumes (i.e. originate equatorward of 15°N), for which several climatologies have been established and are discussed in Section 2.1. A couple of these climatologies (McGuirk et al., 1987; Iskenderian, 1995) have indicated a minimum in tropical plume activity during the months of February and March. The results in this paper tend to support these observations, although it is difficult to directly compare these two sets of results, due to the differing methods of summarizing plume activity. The combined total counts of tropical-polar and classic plumes do show slightly less activity during February, with increased activity in January and April. The increased activity in

January is indicated to be largely due to tropical-polar plumes, while the increased activity in April is largely due to classic plumes.

Several studies (Smith, 1986, McGuirk et al., 1987; Kuhnel, 1989; Iskenderian, 1995) have noted a decrease in tropical plume activity during El Niño events. Figure 2.9 is a plot of January-April tropical plume (classic and tropical-polar plume) activity for the years 1995, 1996, and 1997. In January-April 1997, during which the 1997-98 El Niño event was developing, the combined activity of classic and tropical-polar plumes is observed to decrease, compared to the other two years. This decrease is indicated to be largely due to a decrease in tropical-polar plume activity, as classic plume activity was relatively constant during 1995-1997.

Table 2.1. Plume class definition criteria.

Plume Class	Latitude of origin	Northernmost Latitude	Connect to midlatitude low pressure center?
Classic	< 15N	varies	no
Subtropical	15N-30N	varies	varies
Tropical-polar	< 15N	> 30N	yes

Table 2.2. Classic plume counts. January-April, 1995.

	160-170W	150-160W	140-150W	130-140W	120-130W	110-120W	100-110W
January	1	1	1	2	4	1	4
February	0	3	1	3	7	8	0
March	0	2	2	5	1	1	1
April	4	8	9	0	5	1	5

Table 2.3. Classic plume counts. January-April, 1996.

	160-170W	150-160W	140-150W	130-140W	120-130W	110-120W	100-110W
January	0	1	1	10	10	1	0
February	1	0	3	6	0	2	2
March	2	7	7	6	0	0	0
April	5	2	1	2	2	1	0

Table 2.4. Classic plume counts. January-April, 1997.

	160-170W	150-160W	140-150W	130-140W	120-130W	110-120W	100-110W
January	0	0	2	2	3	3	0
February	0	1	7	3	3	0	0
March	2	6	6	3	0	3	0
April	3	9	9	3	2	2	1

Table 2.5. Classic plume counts. January-April, 1995-1997 average.

	160-170W	150-160W	140-150W	130-140W	120-130W	110-120W	100-110W
January	0.33	0.67	1.33	4.67	5.67	1.67	1.33
February	0.33	1.33	3.67	4	3.33	3.33	0.67
March	1.33	5	5	4.67	0.33	1.33	0.33
April	4	6.33	6.33	1.67	3	1.33	2

Table 2.6. Classic plume counts. January-April, 1995-1997 standard deviation.

	160-170W	150-160W	140-150W	130-140W	120-130W	110-120W	100-110W
January	0.58	0.58	0.58	4.62	3.79	1.15	2.31
February	0.58	1.53	3.06	1.73	3.51	4.16	1.15
March	1.15	2.65	2.65	1.53	0.58	1.53	0.58
April	1	3.79	4.62	1.53	1.73	0.58	2.65

Table 2.7. Subtropical plume counts. January-April, 1995.

	160-170W	150-160W	140-150W	130-140W	120-130W	110-120W	100-110W
January	5	1	7	4	1	2	1
February	7	12	10	7	3	3	3
March	5	5	5	11	3	2	2
April	3	4	5	3	3	1	1

Table 2.8. Subtropical plume counts. January-April, 1996.

	160-170W	150-160W	140-150W	130-140W	120-130W	110-120W	100-110W
January	3	9	5	3	1	1	1
February	3	5	5	8	3	4	1
March	4	1	2	4	2	1	2
April	4	6	2	3	3	0	3

Table 2.9. Subtropical plume counts. January-April, 1997.

	160-170W	150-160W	140-150W	130-140W	120-130W	110-120W	100-110W
January	8	9	7	4	1	1	2
February	3	3	2	1	2	5	2
March	2	5	2	2	0	2	1
April	2	5	5	2	3	2	0

Table 2.10. Subtropical plume counts. January-April, 1995-1997 average.

	160-170W	150-160W	140-150W	130-140W	120-130W	110-120W	100-110W
January	5.33	6.33	6.33	3.67	1	1.33	1.33
February	4.33	6.67	5.67	5.33	2.67	4	2
March	3.67	3.67	3	5.67	1.67	1.67	1.67
April	3	5	4	2.67	3	1	1.33

Table 2.11. Subtropical plume counts. January-April, 1995-1997 standard deviation.

	160-170W	150-160W	140-150W	130-140W	120-130W	110-120W	100-110W
January	2.51	4.62	1.15	0.58	0	0.58	0.58
February	2.31	4.73	4.04	3.79	0.58	1	1
March	1.53	2.31	1.73	4.73	1.53	0.58	0.58
April	1	1	1.73	0.58	0	1	1.53

Table 2.12. Tropical-polar plume counts. January-April, 1995.

	160-170W	150-160W	140-150W	130-140W	120-130W	110-120W	100-110W
January	0	0	4	1	4	2	0
February	0	1	1	0	0	0	0
March	6	0	2	1	0	0	0
April	0	1	1	0	0	0	4

Table 2.13. Tropical-polar plume counts. January-April, 1996.

	160-170W	150-160W	140-150W	130-140W	120-130W	110-120W	100-110W
January	3	4	6	0	0	0	0
February	4	9	2	0	0	0	0
March	2	1	1	0	0	0	0
April	0	0	0	0	3	2	1

Table 2.14. Tropical-polar plume counts. January-April, 1997.

	160-170W	150-160W	140-150W	130-140W	120-130W	110-120W	100-110W
January	0	1	4	0	0	0	0
February	0	0	3	0	0	0	0
March	0	4	1	1	2	1	1
April	0	0	1	0	1	0	0

Table 2.15. Tropical-polar plume counts. January-April, 1995-1997 average.

	160-170W	150-160W	140-150W	130-140W	120-130W	110-120W	100-110W
January	1	1.67	4.67	0.33	1.33	0.67	0
February	1.33	3.33	2	0	0	0	0
March	2.67	1.67	1.33	0.67	0.67	0.33	0.33
April	0	0.33	0.67	0	1.33	0.67	1.67

Table 2.16. Tropical-polar plume counts. January-April, 1995-1997 standard deviation.

	160-170W	150-160W	140-150W	130-140W	120-130W	110-120W	100-110W
January	1.73	2.08	1.15	0.58	2.31	1.15	0
February	2.31	4.93	1	0	0	0	0
March	3.06	2.08	0.58	0.58	1.15	0.58	0.58
April	0	0.58	0.58	0	1.53	1.15	2.08

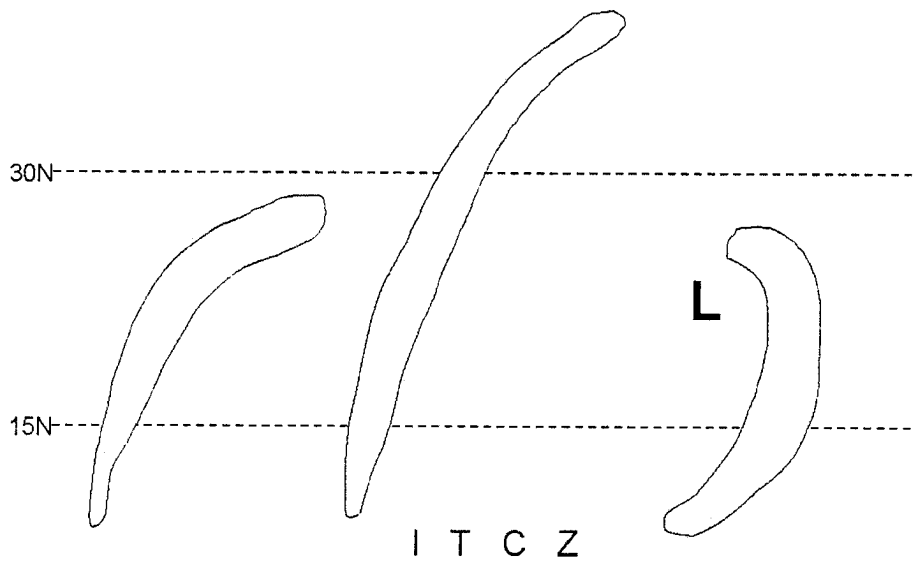

Figure 2.1. Examples of the cloud bands associated with classic plumes.

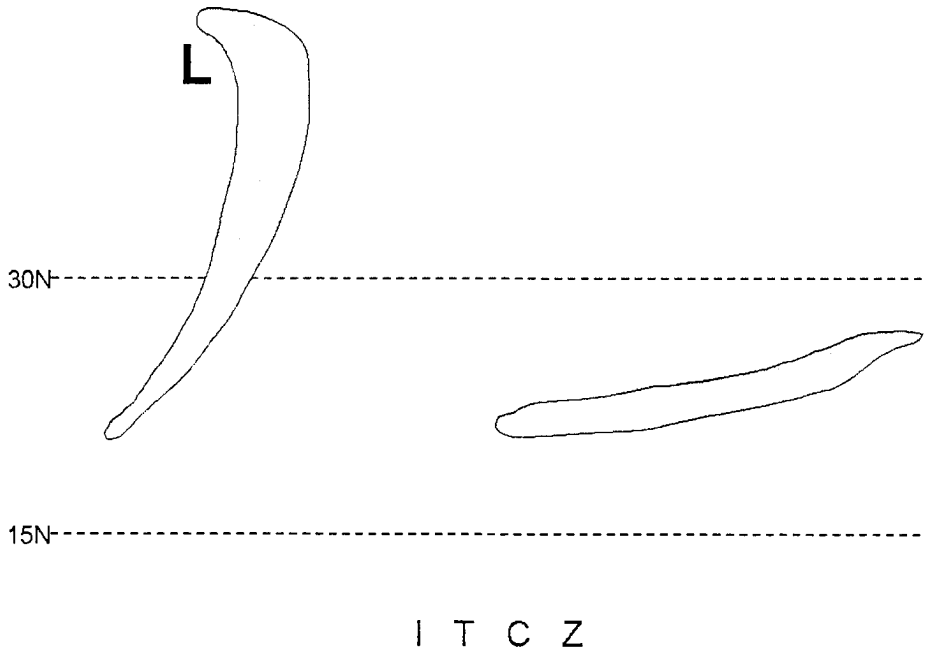

Figure 2.2. Same as Figure 2.1, but for subtropical plumes.

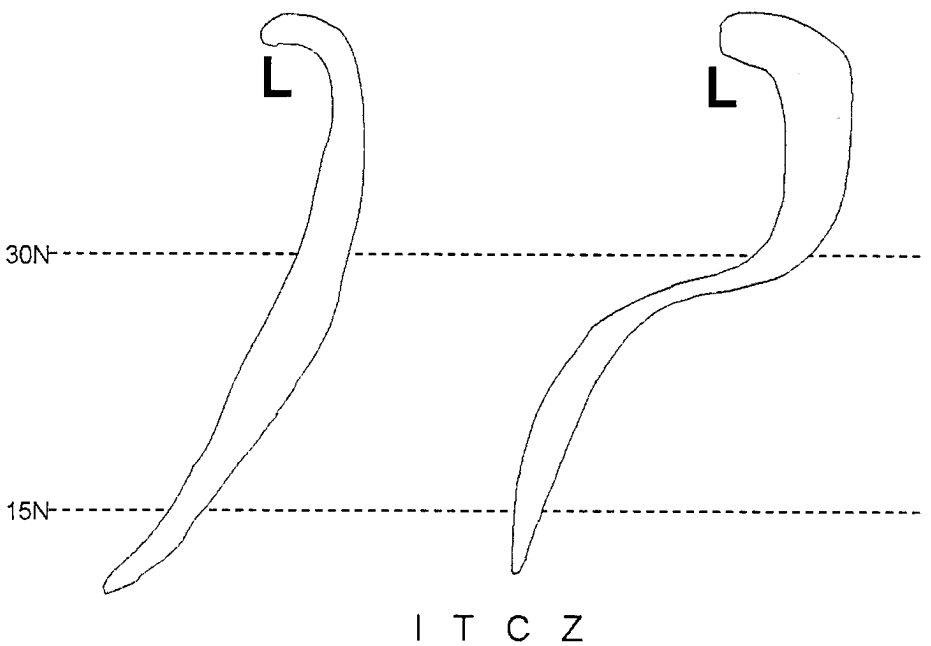

Figure 2.3. Same as Figure 2.1, but for tropical-polar plumes.

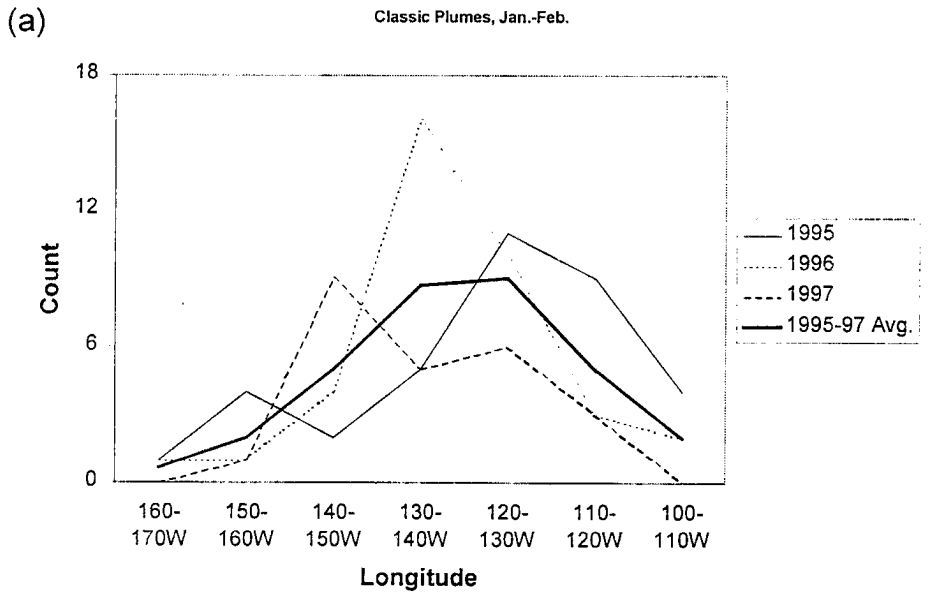

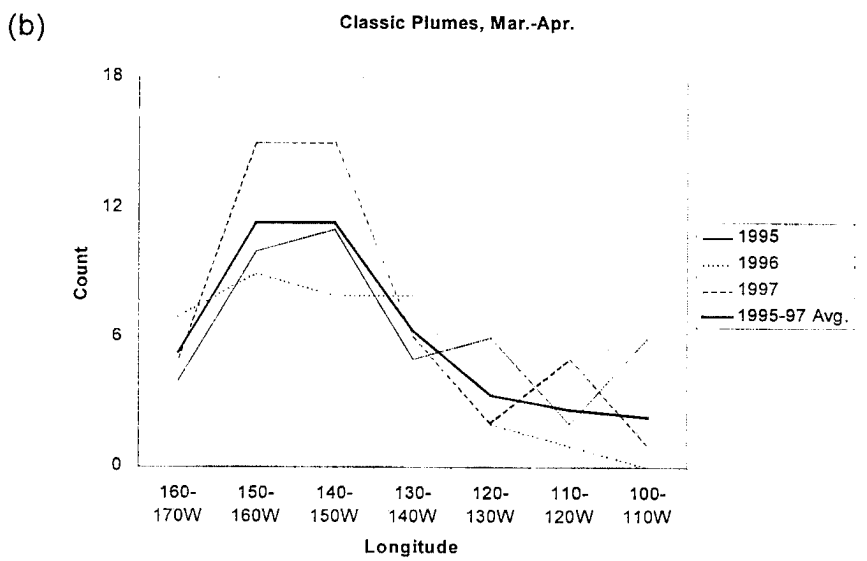

Figure 2.4. Total counts (days) of classic plumes for January-February (a) and for March-April (b).

(a)

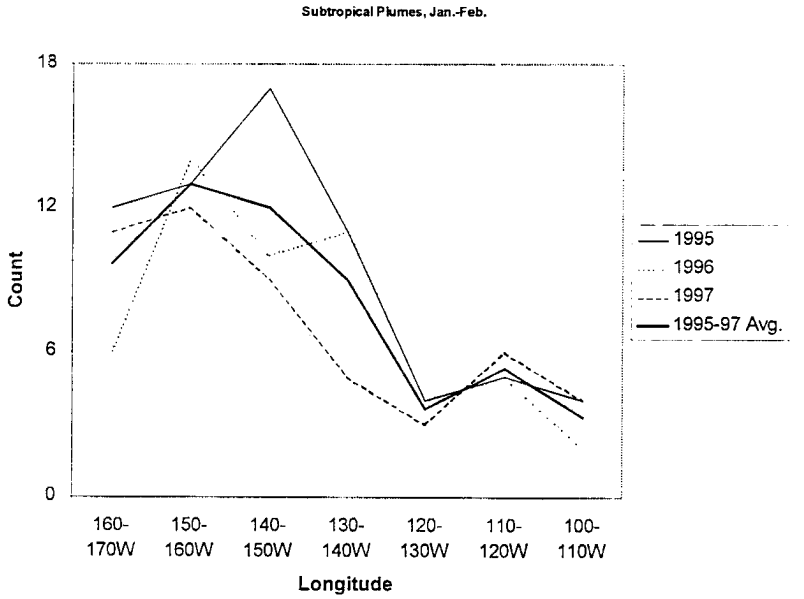

(b)

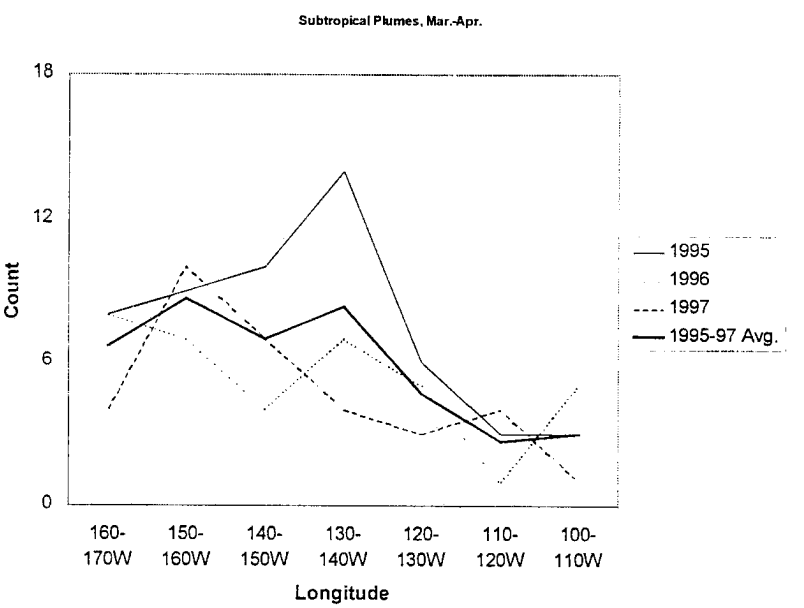

Figure 2.5. Same as Figure 2.4, except for subtropical plumes.

(a)

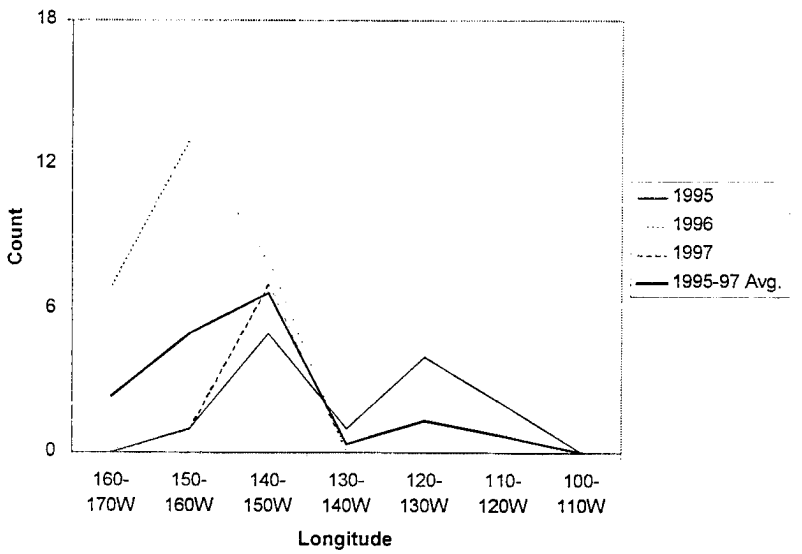

(b)

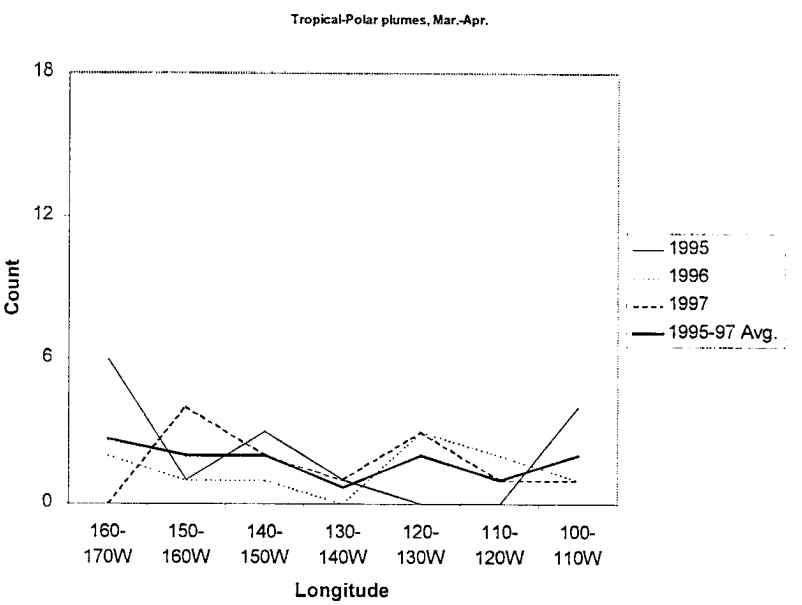

Figure 2.6. Same as Figure 2.4, except for tropical-polar plumes.

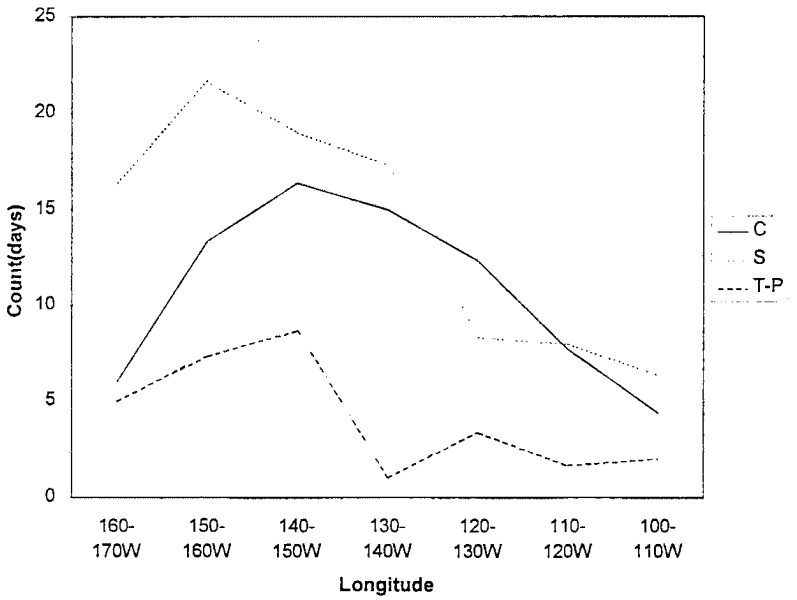

Figure 2.7. Moisture plume activity through the study region, averaged over the January-April period for the years 1995-1997.

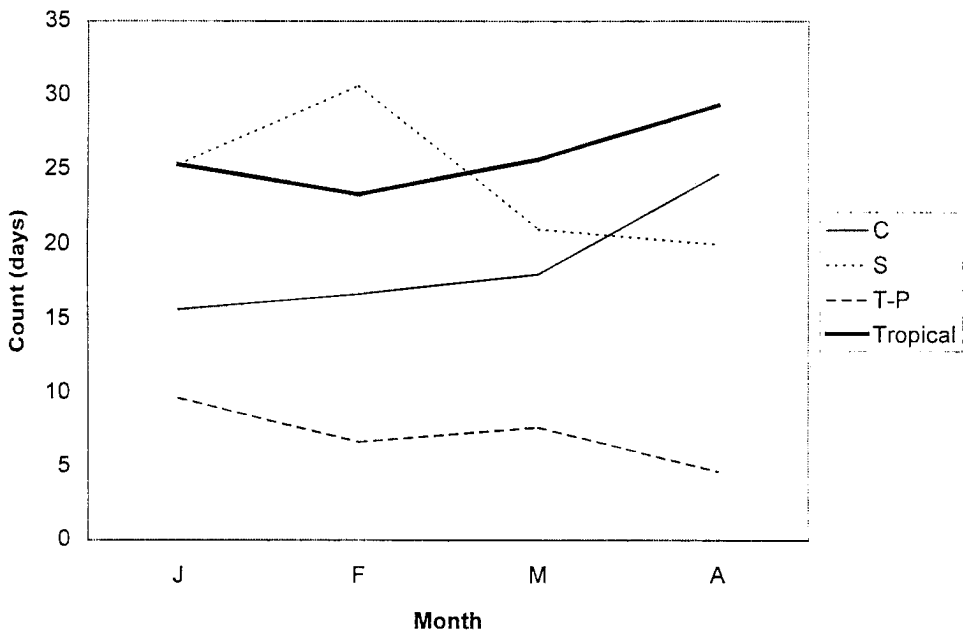

Figure 2.8. Moisture plume activity during the January-April study period, averaged over the study region for the years 1995-1997. The activity of tropical (classic + tropical-polar) plumes is shown in bold.

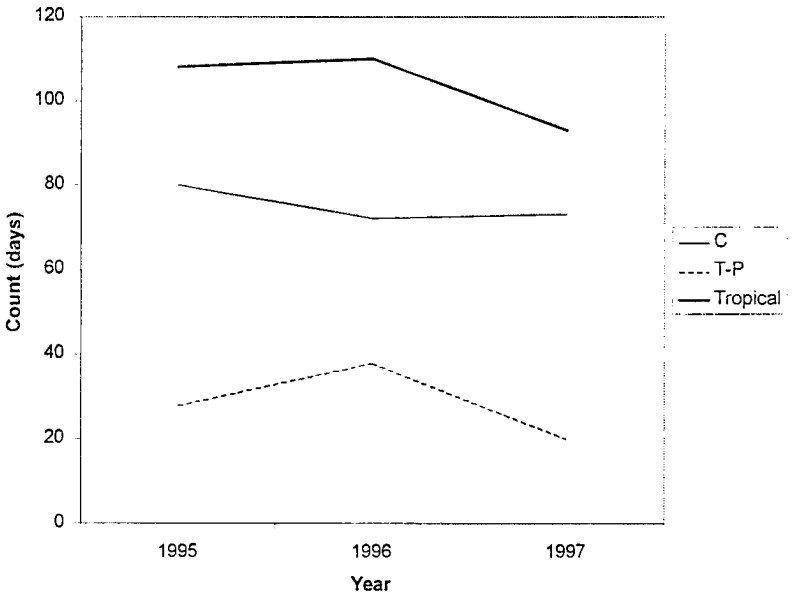

Figure 2.9. Total January-April activity of tropical (classic + tropical-polar) plumes.

3. Methods

3.1 Microwave radiative transfer

Satellite retrievals of vertical moisture profiles have traditionally used either IR or MW wavelengths. Some of the previous studies (Section 1.1) of moisture plumes have used IR-based retrieval methods. The present study is an application of a MW-based retrieval method (BWR) over an oceanic region (the Eastern Pacific-Figure 1.1). The use of MW radiation for profiling atmospheric moisture is advantageous in a couple of ways. First, when clouds are present, the atmosphere is usually more transparent to MW radiation than it is to IR radiation, allowing for the sensing of MW emissions from the entire atmospheric column. Secondly, ocean surfaces exhibit low emissivities at MW wavelengths, compared to infrared wavelengths. This radiatively cold background is useful for detecting the higher-emissivity signals from any low-level moisture (low clouds, water vapor, etc.) which may be present. A main disadvantage of using MW radiation is the relatively poorer horizontal resolution of MW sensors. For instance, the nadir fields-of-view (FOVs) for the SSM/T-2 channels range from 48-88 km (Table 3.1). These resolutions, however, are steadily improving on more recent MW sensors (e.g., the Advanced Microwave Sounding Unit sensors: AMSU-A and AMSU-B).

This section briefly reviews a few important fundamentals of MW radiative transfer in the frequencies of interest to this study (the SSM/T-2 frequencies: 92 GHz, 150 GHz,

183±1 GHz, 183±3 GHz, 183±7 GHz). Figure 3.1 shows the absorption characteristics at these frequencies.

3.1.1 SSM/T-2

The satellite brightness temperature observations used in the BWR algorithm are obtained twice daily from the SSM/T-2 MW sensor on the DMSP F12 satellite. The F12 satellite is a sun-synchronous, near-polar orbiting satellite. The orbit characteristics are similar to those of the F11 satellite: a nominal altitude of 833 km, with an orbital period of 102 minutes and an inclination angle of 98.8° (Lee, 1994). The SSM/T-2 sensor (Falcone et al., 1992) is a five-channel passive MW sensor (Table 3.1) which uses a cross-track scanning pattern. The 92 GHz and 150 GHz channels are situated within atmospheric window regions where MW radiation propagates relatively unimpeded through the atmosphere, with the exception of a little absorption due to atmospheric water vapor (the water vapor continuum). The remaining three channels (183±1 GHz, 183±3 GHz, 183±7 GHz) are centered around the strong water vapor (WV) resonance (absorption) line centered at 183.31 GHz (Figure 3.1). This absorption band is a result of the interaction between the permanent electric dipole moment of the water molecule and the MW radiation at this frequency (Jones, 1989). The weighting functions for each channel are shown in Figure 3.2. The window channels (92 GHz, 150 GHz) are used to retrieve the moisture characteristics of the lower atmosphere. The three WV absorption line channels (183 GHz) are used to retrieve the moisture characteristics of the upper atmosphere; of these three channels, the 183±7 GHz channel penetrates lowest into the upper atmosphere. In all five channels, both vertical and horizontal polarizations are mixed together at some ratio that depends on the viewing angle from nadir (Forsythe, personal communication).

3.1.2 Effects of cloud liquid water, ice

The effects of liquid water clouds that form in the lower atmosphere are easily observed at the 92 GHz and 150 GHz window channels. Cloud droplets readily absorb (and emit) MW radiation. As a result, over oceans, low-level clouds generally have higher brightness temperatures (greater MW emission) than the surrounding ocean background, which is radiatively cold at the SSM/T-2 frequencies (Leute and Stephens, 1993). As one moves to thicker liquid clouds, however, the bulk of the MW emission originates higher up in the cloud, leading to decreased brightness temperatures (Jones, 1989). These thicker clouds are also more likely to contain precipitation-sized liquid particles. These hydrometeors tend to scatter MW radiation, also contributing to lower brightness temperatures.

Ice particles, which are present in high clouds and at the higher levels of some precipitating clouds, are a primary agent for the scattering of upwelling MW radiation (Jones, 1989), which decreases the observed brightness temperature. For high clouds, these scattering effects are substantial for all but the thinnest cirrus clouds. The effects of scattering by ice particles are most apparent in brightness temperature observations in the three WV channels (183 GHz). Locations where higher clouds and/or deep convection are present have lower brightness temperatures than surrounding areas.

3.2 Bayesian Water Vapor Retrieval algorithm

The use of radiometric brightness temperature data to retrieve vertical profiles of moisture is an example of an inversion problem, commonly encountered in remote sensing applications. The inverse problem attempts to determine the atmospheric state responsible for the upwelling radiation received by the satellite sensor. The number of retrieved variables defining the atmospheric state is usually greater than the number of

independent satellite observations. It follows that the inversion process must be somehow constrained (i.e. some atmospheric state variables must be previously specified) if a solution is to be found.

The BWR algorithm uses the inverse problem in this paper to retrieve vertical moisture profiles from MW brightness temperature observations obtained from the SSM/T-2 sensor (Section 3.1.1) aboard the DMSP F12 satellite. The BWR algorithm consists of three primary units (Lietzke, 1998): the Inputs Module (Section 3.2.2), the Radiative Transfer Module (Section 3.2.3), and the Optimization Module (Section 3.2.4).

3.2.1 Bayes' theorem

The BWR algorithm uses Bayes' theorem to constrain the solution to the inverse problem. The solution is constrained by introducing prior information about the atmospheric state (the moisture profile to be retrieved). When applied to moisture retrieval, Bayes' theorem (Lietzke, 1998) states that

$$P(x \mid y) = aP(y \mid x)P(x) \tag{3.1}$$

where P(x|y) is the posterior probability given x, the atmospheric state, and y, the observed satellite brightness temperature. P(x) is the prior probability, P(y|x) is the conditional (or forward) probability, and a is a normalization constant. A multivariate normal distribution is assumed for the prior and forward probability distributions, so that

$$P(y \mid x) = \exp\left[-(y - y(x))^T C_y^{-1} (y - y(x))/2\right] \tag{3.2}$$

$$P(x) = \exp\left[-(x - x_m)^T C_x^{-1} (x - x_m)/2\right] \tag{3.3}$$

In these relations, y(x) is the simulated brightness temperature observation, which is based on a forward model radiative transfer calculation using the retrieved moisture

profile, x; x_m is the prior moisture profile used to constrain the retrieval (Table 3.2); C_x is the prior covariance (Table 3.2); and C_y is the combined error covariance of the satellite sensor and the forward model (Table 3.3). The goal is to determine which atmospheric profile (x) maximizes the posterior probability P(x|y) and hence provides the best solution to the inverse problem. This is accomplished by finding the minimum of a cost function J(x), given by

$$J(x) = (y - y(x))^T C_y^{-1} (y - y(x)) + (x - x_m)^T C_x^{-1} (x - x_m) \quad (3.4)$$

This minimization is performed using the Powell Direction Set Method (Press et al., 1992).

3.2.2 Inputs module

The Inputs module processes three items of input data: the user-defined atmospheric structure, the prior information used to constrain the solution, and the SSM/T-2 observations. The user-defined atmospheric structure specifies the variables to be retrieved, which atmospheric levels are to be retrieved at, and auxiliary data (assumed to be known) to be used in the forward model calculations (Section 3.2.3). Ample flexibility exists on how the atmospheric structure is defined by the user. Table 3.4 summarizes the structure that was used for this study. Retrievals were performed at 6 atmospheric levels: 1000 mb, 850 mb, 700 mb, 500 mb, 400 mb, and 300 mb; these levels correspond roughly to the upper air mandatory reporting levels for National Weather Service (NWS) weather station observations. The retrieved variables were: relative humidity at the six specified pressure levels, cloud liquid water content, cloud ice water content, the cloud top heights of both liquid and ice clouds, and a MW surface emissivity

parameter (MSEP-1). For ocean applications, MSEP-1 accounts for changes in surface emissivity due to ocean surface winds.

A typical source of prior information for inverse problem applications is the climatological mean, x_m, and its covariance, C_x, for the atmospheric state being retrieved (Table 3.2). This prior information is used for the initial guess in the retrieval process. Past tropical oceanic applications of the BWR algorithm (Lietzke, 1998; Lietzke et al., 2000) have used a single relative humidity climatological mean and covariance dataset, derived from tropical radiosonde data.

Moisture plumes, however, have a spatial extent often extending from the tropics into the midlatitudes (see Figures 2.1-2.3). A wide variety of atmospheric states are encountered between the tropics and midlatitudes, particularly with respect to atmospheric moisture (Peixoto and Oort, 1992). For instance, one can often expect the tropical regions to be moist throughout the atmospheric column, especially around the ITCZ. The subtropical regions are dominated by the subtropical high, which gives rise to a dry upper atmosphere above a moist lower atmosphere (below the trade wind inversion). The midlatitudes exhibit highly variable moisture profiles, depending on the passage of midlatitude storms. These moisture profiles also have marked annual variations. To address these variations, relative humidity mean and covariance datasets (x_m and C_x) were obtained from NCEP reanalysis forecast model data (see Table 3.2). The NCEP reanalysis data has a spatial resolution of 2.5° latitude by 2.5° longitude. For each month in which retrievals were performed (March and April 1995; January-April, 1996), separate relative humidity prior information datasets were produced for each NCEP grid box. For a BWR retrieval at a given location, the appropriate prior information was obtained from the corresponding NCEP grid box.

Various auxiliary data are provided in the Inputs module to aid in the retrieval calculations. In addition to the monthly relative humidity information, daily-averaged

temperature profiles for each NCEP grid box are obtained for the day on which a given retrieval is performed (Table 3.4). These daily temperature data are used along with the monthly relative humidity information to initialize the Radiative Transfer module. Additional constant auxiliary parameters are provided for the radiative transfer calculations (Section 3.2.3). These parameters include liquid and ice cloud thickness, liquid cloud droplet radius, ice cloud particle mean diameter, total column ozone, and MW surface emissivity parameters (Table 3.5).

3.2.3 Radiative Transfer module

The primary purpose of the Radiative Transfer module is to calculate a set of simulated top-of-the-atmosphere (TOA) brightness temperature observations at each of the SSM/T-2 channels, based on the atmospheric structure and auxiliary information provided in the Inputs module. Lietzke (1997) provides a detailed discussion on the Radiative Transfer module. This work uses the MW portion of this module.

The only change made in the Radiative Transfer module from Lietzke's work is with the ocean surface MW emissivity. The previous expression used was that of the product of the Fresnel emissivity of calm water and MSEP-1 (Table 3.4):

$$\varepsilon = 0.5(\varepsilon_v + \varepsilon_h)(MSEP1) \tag{3.5}$$

where ε_v and ε_h are the emissivities for the vertical and horizontal polarizations, respectively. Although the Fresnel emissivity of calm water holds at nadir viewing angles, this is not correct for off-nadir viewing angles. An alternate expression (Lietzke, personal communication) is

$$\varepsilon = \left[\varepsilon_v \cos^2\left(\frac{\pi\theta}{180}\right) + \varepsilon_h \sin^2\left(\frac{\pi\theta}{180}\right)\right](MSEP1) \tag{3.6}$$

where θ is the viewing angle from nadir. This expression accounts for the variation in surface MW emissivity as a function of viewing angle from nadir. This expression is then multiplied by the MSEP-1 parameter in order to obtain the actual surface MW emissivity.

3.2.4 Optimization module

For a given retrieval, once the simulated MW observations for each SSM/T-2 channel are calculated from the Radiative Transfer module, these results are passed on to the Optimization module. This module then works together with the Radiative Transfer module to iteratively find the best solution to the atmospheric state which gives rise to the observed MW radiances. This is done by using Bayes' theorem and the Powell Direction Set Method to maximize the posterior probability (Lietzke, 1998). In order to ensure that the solution obtained is not a local maximum, the Radiative Transfer module uses five separate initial guesses on the atmospheric state. These initial guesses are obtained by randomly perturbing (five times) the prior relative humidity information provided in the Inputs module. A best-guess solution to the atmospheric state is obtained for each of these initial guesses. Of these five solutions, the one that has the highest posterior probability is picked as the final solution.

3.3 Moisture transport

The retrieved relative humidities at each atmospheric level can be combined with the daily NCEP reanalysis temperature data (Table 3.4) and wind data for that location to calculate moisture transports at each retrieved atmospheric level and the total moisture transport. To begin with, for each level *n* to be retrieved at, the saturation vapor pressure e_s (mb) is calculated by (Bolton, 1980):

$$e_{s,n} = 6.1121 \exp\left[\frac{(17.67T_n)}{T_n + 243.5}\right] \tag{3.7}$$

where T_n is the atmospheric temperature at atmospheric level *n*, taken from the NCEP reanalysis temperature profile. The saturation vapor pressure is then combined with the relative humidity and pressure (mb) at the atmospheric level *n* to determine the specific humidity q_n (g/kg):

$$q_n = 1000b\frac{e}{p} = 1000b\left(\frac{e_{s,n}RH_n}{p}\right) \tag{3.8}$$

where *b* is a constant factor (=0.622). The moisture transport Q_n ($gkg^{-1}ms^{-1}$) at the level *n* is then found by multiplying q_n by the wind at that level (v_v). In order to obtain the total moisture transport Q ($gm^{-1}s^{-1}$), the moisture transport at each level is integrated over the entire atmospheric column:

$$Q = \frac{1}{g}\int(qv)dp \tag{3.9}$$

For the present work, this quantity is approximated by

$$Q \approx \frac{1}{g}\sum_{n=1}^{6} q_n v_n \Delta p_n \tag{3.10}$$

The moisture transports calculated here are useful for determining what contribution moisture plumes have in the overall atmospheric transport of moisture.

Table 3.1. SSM/T-2 channel characteristics (after Leute and Stephens, 1993).

Channel No.	Frequency (GHz)	Nadir FOV (km)	Peak Altitude (mb)	NEΔT (K)
1	183.31 ± 3	48	650	0.6
2	183.31 ± 1	48	500	0.8
3	183.31 ± 7	48	800	0.6
4	91.655	88	Surface	0.6
5	150.0	54	1000	0.6

Table 3.2. Prior mean vector (x_m) and covariance matrix (C_x). Shaded areas represent values that depend on NCEP reanalysis.

x_m	Variable	C_x										
0	Liquid Water Content (gm^{-3})	0.0003	0	0	0	0	0	0	0	0	0	0
2.5	Liquid Cloud Top Height (km)	0	40	0	0	0	0	0	0	0	0	0
0	Ice Water Content (gm^{-3})	0	0	0.0004	0	0	0	0	0	0	0	0
8.0	Ice Cloud Top Heighr (km)	0	0	0	90	0	0	0	0	0	0	0
1.0	MSEP-1	0	0	0	0	0.0001	0	0	0	0	0	0
	Rel. Humidity (%) at 1000 mb	0	0	0	0	0						
	Rel. Humidity (%) at 850 mb	0	0	0	0	0						
	Rel. Humidity (%) at 700 mb	0	0	0	0	0						
	Rel. Humidity (%) at 500 mb	0	0	0	0	0						
	Rel. Humidity (%) at 400 mb	0	0	0	0	0						
	Rel. Humidity (%) at 300 mb	0	0	0	0	0						

Table 3.3. Combined error covariance (C_y).

Frequency (GHz)					
91.655	1.0	0	0	0	0
150.0	0	1.0	0	0	0
183.31 ± 1	0	0	1.0	0	0
183.31 ± 3	0	0	0	1.0	0
183.31 ± 7	0	0	0	0	1.0

Table 3.4. Retrieved variables and auxiliary data.

Pressure level (mb)	Variable	Auxiliary
-	Cloud Liquid Water (gm^{-3})	-
-	Liquid Cloud Height (km)	-
-	Cloud Ice Water (gm^{-3})	-
-	Ice Cloud Height (km)	-
-	Microwave Emis. Parameter 1	-
1000	Relative Humidity (%)	Temperature (K)
850	Relative Humidity (%)	Temperature (K)
700	Relative Humidity (%)	Temperature (K)
500	Relative Humidity (%)	Temperature (K)
400	Relative Humidity (%)	Temperature (K)
300	Relative Humidity (%)	Temperature (K)
200	-	Temperature (K)

Table 3.5. Auxiliary inputs (assumed constant) used in the Radiative Transfer module.

Constant Auxiliary Inputs	Ocean surf. value
Liquid Cloud Thickness (km)	1.0
Ice Cloud Thickness (km)	1.0
Liquid Cloud Droplet Radius (μm)	20
Ice Cloud Particle Median Diameter (μm)	200
Total Column Ozone (Dobson units)	350
Infrared Surface Emissivity	0.98
Microwave Surface Emissivity Parameters (2, 3, 4)	0, 91.6, 0

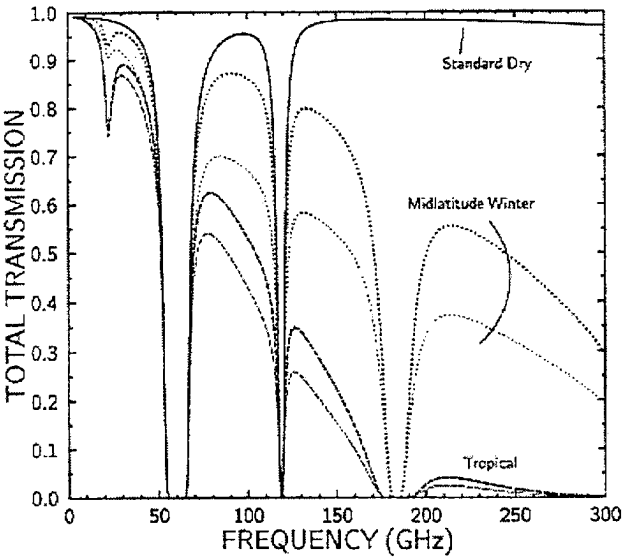

Figure 3.1. Microwave transmission spectrum (after Greenwald and Stephens, 1995).

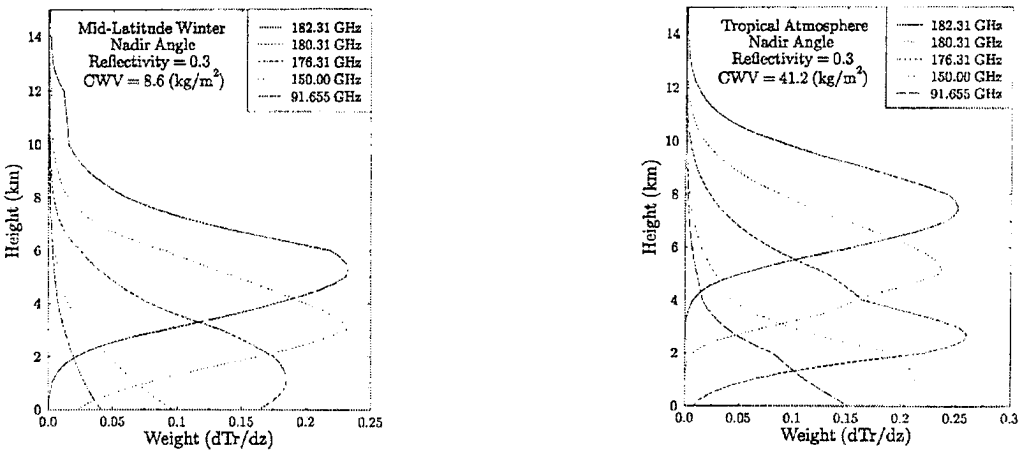

Figure 3.2. SSM/T-2 weighting functions (after Leute and Stephens, 1993).

4. Moisture Distribution

In regions where surface observations are sparse, such as the eastern Pacific Ocean, satellite observations are often the only means of determining the three-dimensional structure of moisture within the tropospheric column (see, for example, Lietzke et al., 2000). Relative humidity and cloud liquid and ice parameters retrieved from the BWR algorithm are now used to estimate the three-dimensional structure of moisture within the three moisture plume classes. For each plume class, ten case studies were selected. These case studies were selected on the basis of SSM/T-2 coverage. It was desired that the SSM/T-2 coverage be such that at least one of the two daily orbit passes over the area viewed the entire width of the moisture plume. Table 4.1 lists all of the case studies for this present study. Tables 4.2 and 4.3 present some summary statistics for cloud liquid water and cloud ice water for each of the case studies.

4.1 Classic plumes

The classic plume case study discussed here is a classic plume that occurred on March 25, 1996 (Figure 4.1). This moisture plume occurred during a large Rex-block (Rex, 1952) pattern, centered on 150°W longitude, which is indicated in the 500-mb analysis (Figure 4.2). The upper-level trough associated with the moisture plume development was a deep low-pressure center that cut off from the main midlatitude flow and was centered near 37°N, 150°W. This low-pressure center was situated to the north

of the moisture plume, which originated between 150°W-160°W and occupied the southern side of the low-pressure trough. In the 200-mb analysis (Figure 4.3), a strong jet stream is also evident due east of the southern tip of the low-pressure trough, in the same region occupied by the moisture plume. An intensified jet stream in the vicinity of a moisture plume is a feature that has been noted in previous studies (see Chapter 1).

The first vertical cross section for this case study (Figure 4.4a) shows a deep area of moisture along the main plume axis, centered near 151°W, with relative humidities exceeding 90%. In all subsequent discussion on vertical relative humidity cross sections, the main plume axis is defined as the longitude (or latitude/longitude pair) at which the deepest, continuous column of high relative humidities (usually > 80%) occurs. To the left (north and west) of the plume, the atmosphere dries out considerably. A second area of relative humidities exceeding 90% is indicated at about 400 mb, a few degrees longitude to the east (right) of the main plume axis. This area of moisture is clearly indicated in the second vertical cross section (Figure 4.4b). These profiles can be compared to the moisture profiles presented by Schaefer (1985), which also show deep moisture along the plume axis, upper-level moisture to the east of the main plume axis, and marked drying to the left (west) of the plume (Figure 1.2). Maps of cloud liquid water (Figure 4.5a) and cloud ice water (Figure 4.5b) show the close proximity of the clouds along the plume axis and the ice cloud mass just to the south and east of the plume. The calculated cloud liquid water within the plume is relatively small, with a maximum value of 0.45 gm^{-3} (see Table A.1). This result is a bit puzzling, given the deep moisture indicated along the main plume axis (Figure 4.4a). The calculations for cloud ice water for this case study (Table A.2) indicate that ice cloud is relatively more dominant than liquid cloud. The maximum cloud ice water is 0.55 gm^{-3}.

4.2 Subtropical plumes

Figure 4.6 shows a subtropical plume that occurred on February 8, 1996. This plume was associated with a frontal cloud band on the eastern side of a midlatitude trough approaching the U.S. west coast (Figure 4.7). The plume originated between 140°W and 150°W, at the southern tip of the trough, which was centered at 140°W. This storm system had large impacts on the S. Oregon and N. California coasts. Precipitation totals for the 24-hour period ending at 12Z on February 9 (Figure 4.8) were as high as 2.46 inches on the Pacific coast near Brookings, OR, just north of the Oregon/California border.

The vertical relative humidity cross section in Figure 4.9a shows a moist region along the plume axis (127°W) that extends up to 300 mb, indicating cloudiness through the entire troposphere. Maximum RH values along the plume axis consistently exceed 90% at all levels of the atmosphere up to about 400 mb. To the west of the plume, starting at about 137°W, the tropospheric column is very dry, indicating strong subsidence. Closer to the plume axis, pockets of low-level moisture are indicated along the west side of the plume, near 131°W and 135°W. Relative humidities within these moisture pockets approach 70% and greater. The structure of these moisture pockets suggests that these might be areas of developing convection, feeding into the moisture plume. An area of high RH in the upper levels of the atmosphere is indicated a couple of degrees longitude to the right (south and east) of the deep moisture along the plume axis. Unlike the case study in Section 4.1, the upper-level moisture area is not a feature separate from the moisture along the plume axis. The two features are, for the most part, combined as one feature.

The second cross section (Figure 4.9b) shows the southern end of the moisture plume. In this cross section, the plume appears as a narrow strip of low-level moisture; virtually all of the moisture is confined below 500 mb. This could indicate that the

southern edge of the plume is comprised mostly of low-level cloudiness/convection, with very little ice cloud. This is indeed what is suggested on the GOES image (Figure 4.6), as well as on the plots of cloud liquid water (Figure 4.10a) and cloud ice water (Figure 4.10b). Cloud liquid water is very abundant throughout the plume, with a maximum of 1.32 gm^{-3} (Table A.1). The greatest cloud ice water is found in scattered patches just along the plume axis, possibly in those areas where convection is especially vigorous.

4.3 Tropical-polar plumes

A tropical-polar plume that occurred on January 1, 1996 is shown in Figure 4.11. Deeper convection is evident at the southern end of the plume. To the north, high clouds are still abundant, but it isn't obvious whether deep convection is occurring in the area or whether these clouds are being advected in from the south. This plume formed during a period of highly amplified meridional flow in the eastern Pacific Ocean. The plume, which originated in the 140°W-150°W longitudinal belt, was positioned between a sharp midlatitude trough near 160°W and an amplified ridge positioned near 130°W, just off the U.S. west coast (Figure 4.12).

A couple of vertical cross sections along the northern part of the plume are given in Figures 4.13a and 4.13b. Figure 4.13a indicates that along the moisture plume axis, near 140°W, moisture is quite abundant throughout the tropospheric column; RH values of greater than 90% are found up to about 400 mb. Cloud liquid water values within this region (Figure 4.14a) are generally between 0.5-1.0 gm^{-3}. The maximum cloud liquid water within the plume is 1.22 gm^{-3} (Table A.1). Returning to Figure 4.13a, an area of high-level moisture is apparent near 145°W, to the left of the main plume axis. This may possibly be due to high cirrus clouds on the left edge of the cloud band associated with the plume (Figure 4.11, Figure 4.14b).

Figure 4.13b shows a profile taken near a developing area of low pressure along the middle portions of the plume. The developing low-pressure center is also evident in Figure 4.11. The moisture maximum along the plume axis is clearly seen, centered near 146°W. To the left of the main moisture maximum, near 150°W, a small pocket of increased moisture with RH values of 60%-70% is indicated near 500 mb. This maximum is in approximately the same location as the center of the developing area of low pressure (see Figures 4.11, 4.14). Figure 4.14b indicates that ice cloud is present near the low-pressure center. Some high-level clouds along the western edge of the plume are being drawn into the developing circulation (Figure 4.11). These higher clouds may be contributing, along with any convection near the low-pressure center, to the moisture maximum near 150°W.

In addition to the moisture maximum near 150°W, Figure 4.13b also shows somewhat elevated moisture near 500 mb, relative to the adjacent atmospheric layers, to the east of the main plume axis. Maximum RH values are between 50%-60%. This somewhat moist layer is possibly due to cirrus clouds on the eastern portions of the cloud band associated with the plume (Figure 4.11).

The third relative humidity profile (Figure 4.13c) is taken near the area of increased convection at the southern end of the plume. Convective centers are clearly indicated at both 152°W and 156°W, where RH values are frequently at 90% or greater throughout much of the tropospheric column. The convection near 156°W is located on the plume axis. Upper-level moisture between 400-500 mb is indicated to the east of the convective centers, at about 149°W. As Figure 4.11 indicates, this moisture may be due to high clouds advecting northward from an area of enhanced ITCZ convection just south of the moisture plume.

4.4 Summary

For the three cases considered in this chapter, some common features were found in the vertical profiles of relative humidity. These features were: 1) moisture extending through much of the tropospheric column near the plume axis, 2) marked drying just to the north and west of the plume axis, and, in some cases, 3) upper-level moisture overlying drier air at the mid-levels to the south and east of the plume axis. Some exceptions to these patterns do exist, however (e.g., Figures 4.9b and 4.13c). It should be noted that the regions with the greater indicated moisture content are also the regions that realize poorer retrieval performance (see Chapter 6). In these areas, it is less certain that the retrieved atmospheric state matches the actual state. These areas often correspond to areas with greater amounts of liquid and ice cloud.

Increased values of cloud liquid water are usually indicated within moisture plumes in regions where either substantial low-level cloudiness or deep cloudiness throughout the tropospheric column is present. Areas with higher cloud ice water tend to correspond to those areas in the relative humidity profiles where substantial upper-level (above 500 mb) moisture is retrieved.

In general, cloud liquid water values are smallest for classic plumes (Table 4.2). This suggests that the moisture in classic plumes is situated more in the upper levels than at lower levels, with more ice cloud relative to liquid cloud than in the other two case studies (Table 4.3). These findings support studies such as McGuirk et al. (1987), which found that these types of plumes were primarily upper-level events. Cloud ice water values are markedly lower for subtropical plume than they are for classic and tropical-polar plumes. This finding, along with the relatively high values of cloud liquid water, suggests that subtropical moisture plumes are the most likely of the three plume classes to have little or no upper-level moisture present (e.g. Figure 4.9b).

Table 4.1. Listing of case study dates for each plume class. Asterisks (*) indicate the case studies discussed in this paper.

Classic	Subtropical	Tropical-polar
3/18/95	3/10/95	3/7/95
4/27/95	3/13/95	1/1/96*
4/29/95	4/3/95	1/10/96
1/23/96	4/9/95	1/23/96
1/25/96	1/5/96	1/25/96
1/28/96	1/7/96	1/28/96
2/25/96	1/31/96	1/29/96
3/4/96	2/8/96*	2/19/96
3/25/96*	4/6/96	2/21/96
3/28/96	4/14/96	3/8/96

Table 4.2. Summary statistics of cloud liquid water (gm^{-3}). The coefficient of variance is the ratio of the standard deviation and the mean.

	Maximum	Mean	Standard Dev.	Coeff. of Var.
Classic	0.962	0.092	0.132	1.511
Subtropical	1.278	0.141	0.242	1.71
Tropical-polar	1.215	0.143	0.204	1.46

Table 4.3. Summary statistics for cloud ice water (gm^{-3}).

	Maximum	Mean	Standard Dev.	Coeff. of Var.
Classic	0.595	0.042	0.071	1.698
Subtropical	0.521	0.034	0.053	1.647
Tropical-polar	0.6	0.036	0.069	2.013

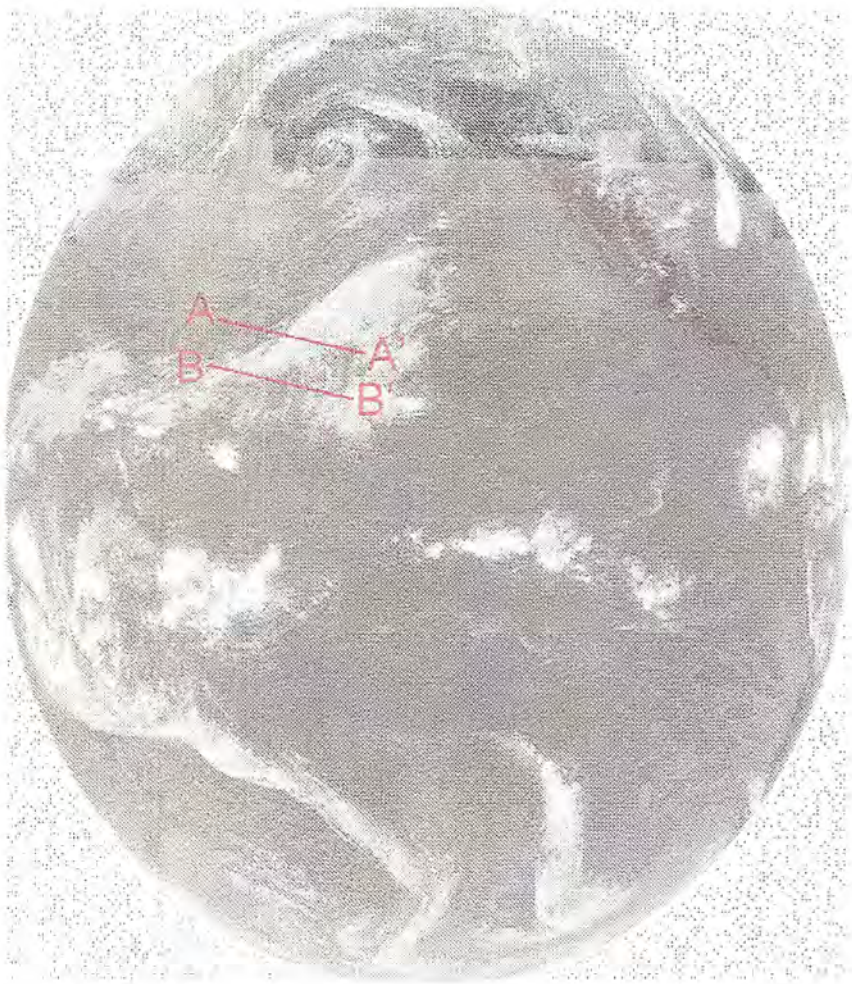

Figure 4.1. GOES-West IR image, March 25, 1996 classic plume. Vertical cross sections A-A' and B-B' are indicated.

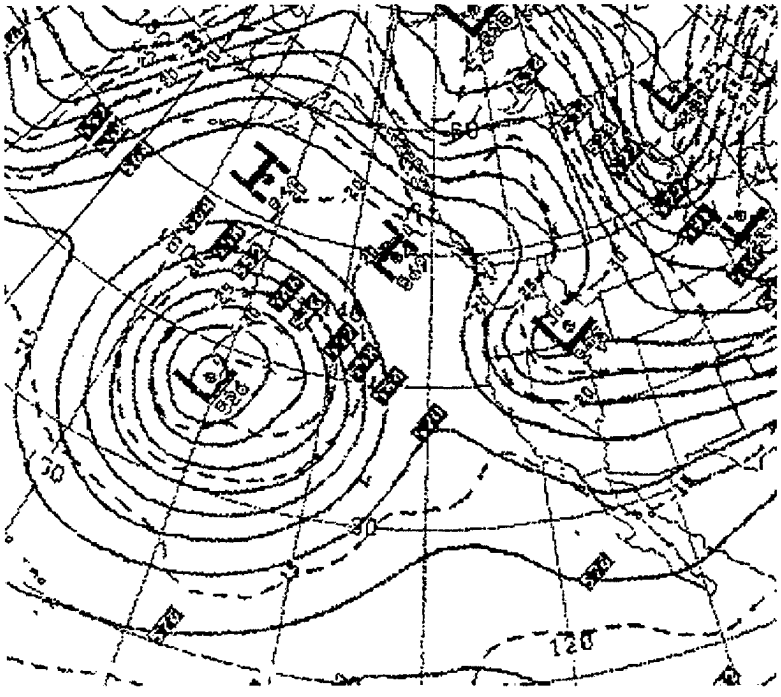

Figure 4.2. 500-mb analysis, March 25, 1996.

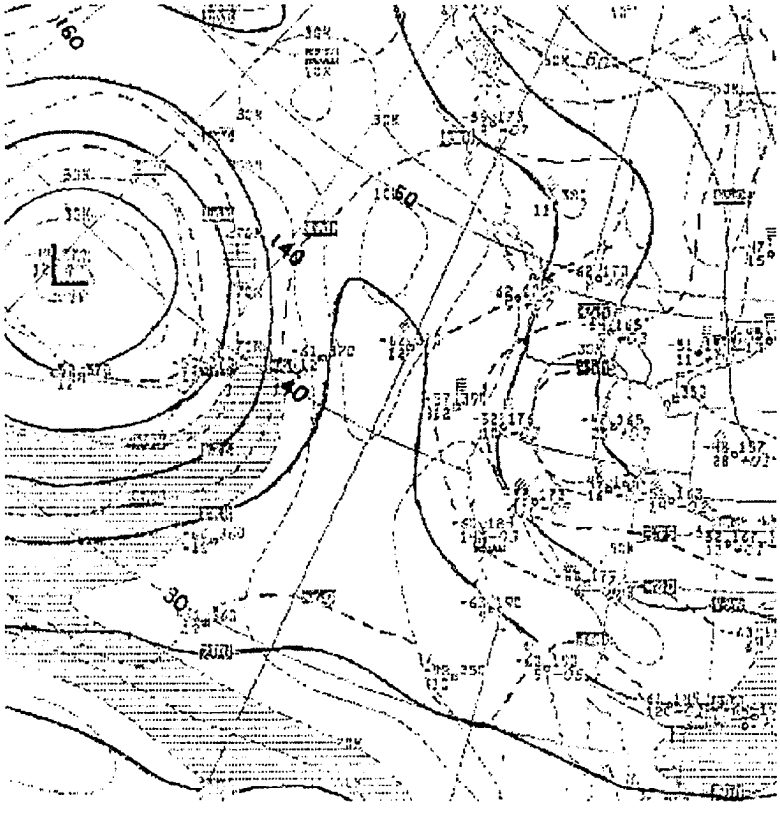

Figure 4.3. 200-mb analysis, March 25, 1996.

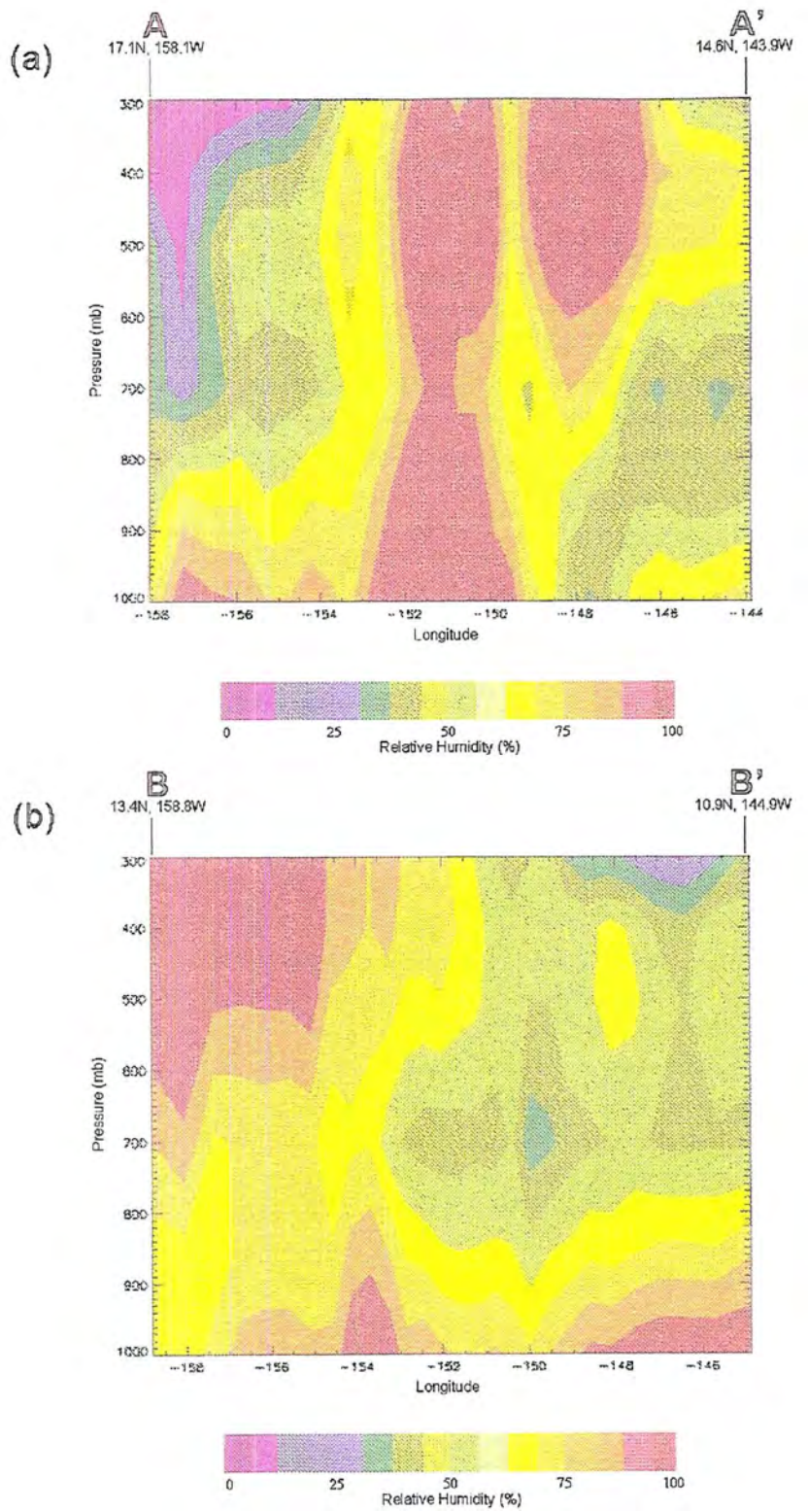

Figure 4.4. Relative humidity profiles A-A' (a) and B-B' (b) for the March 25, 1996 classic plume.

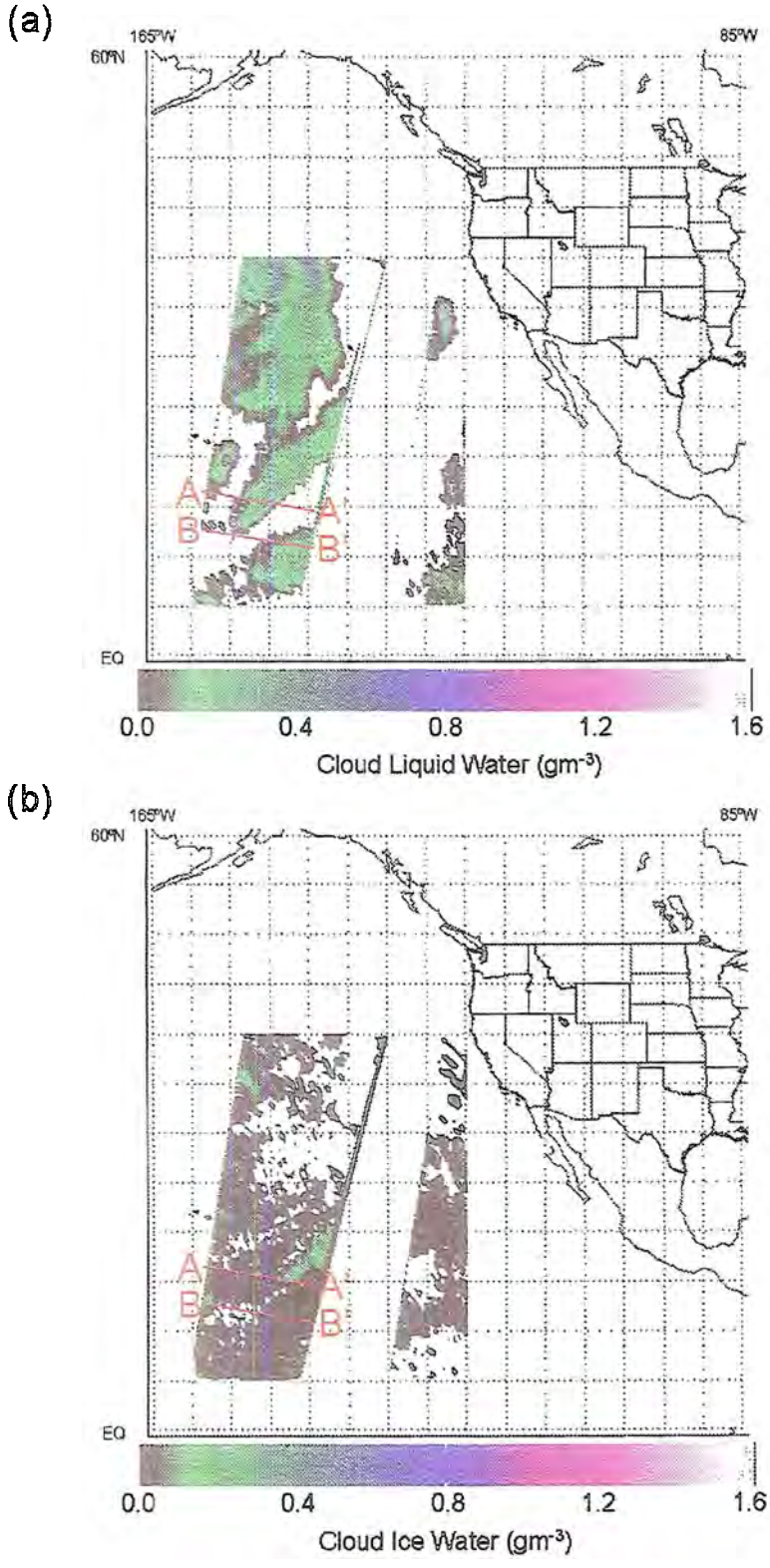

Figure 4.5. Cloud liquid water (a) and cloud ice water (b) for the March 25, 1996 classic plume. Vertical cross sections A-A' and B-B' are indicated.

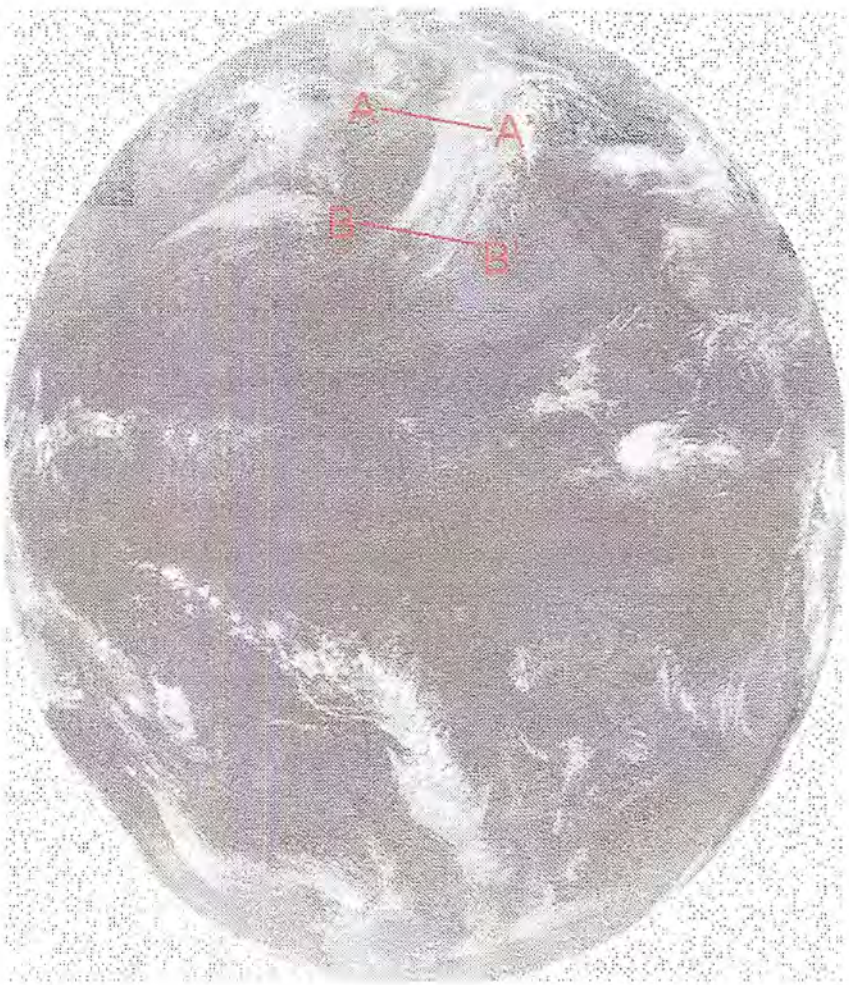

Figure 4.6. GOES-West IR image, February 8, 1996 subtropical plume. Vertical cross sections A-A' and B-B' are indicated.

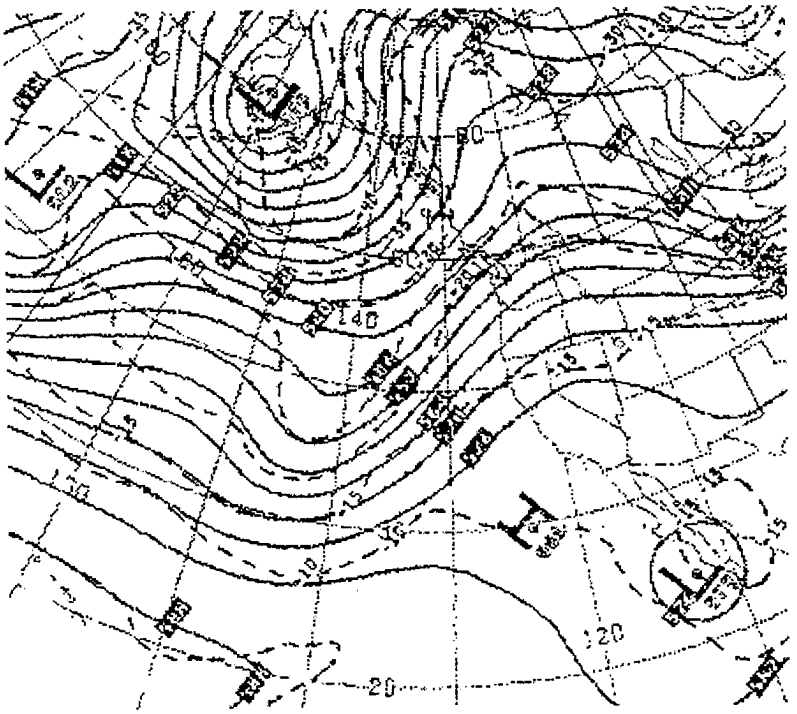

Figure 4.7. 500-mb analysis, February 8, 1996.

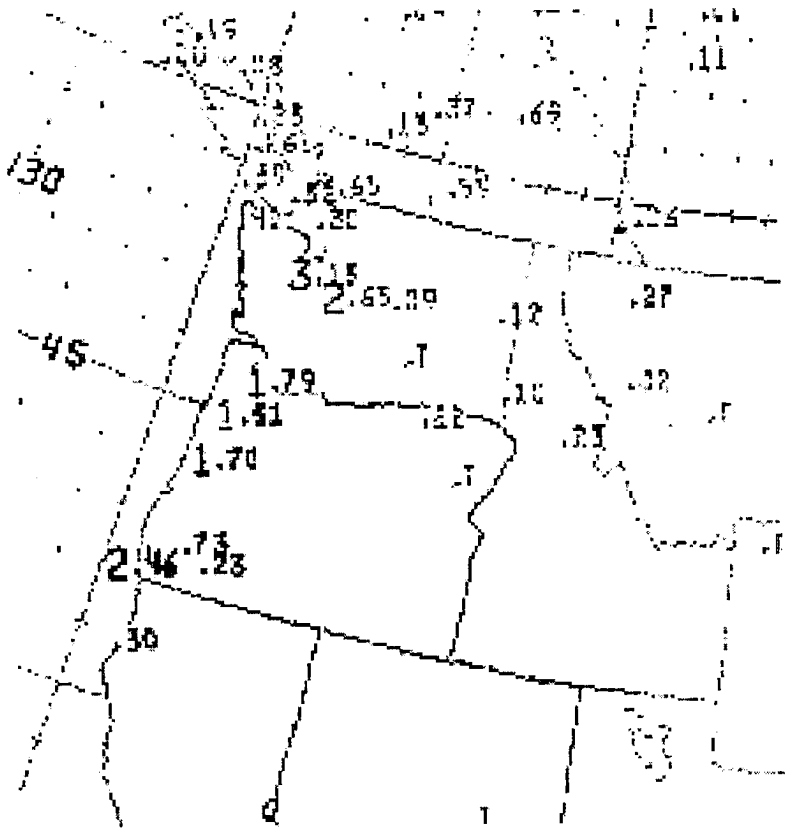

Figure 4.8. Map of 24-hour precipitation ending on 12Z, February 9, 1996.

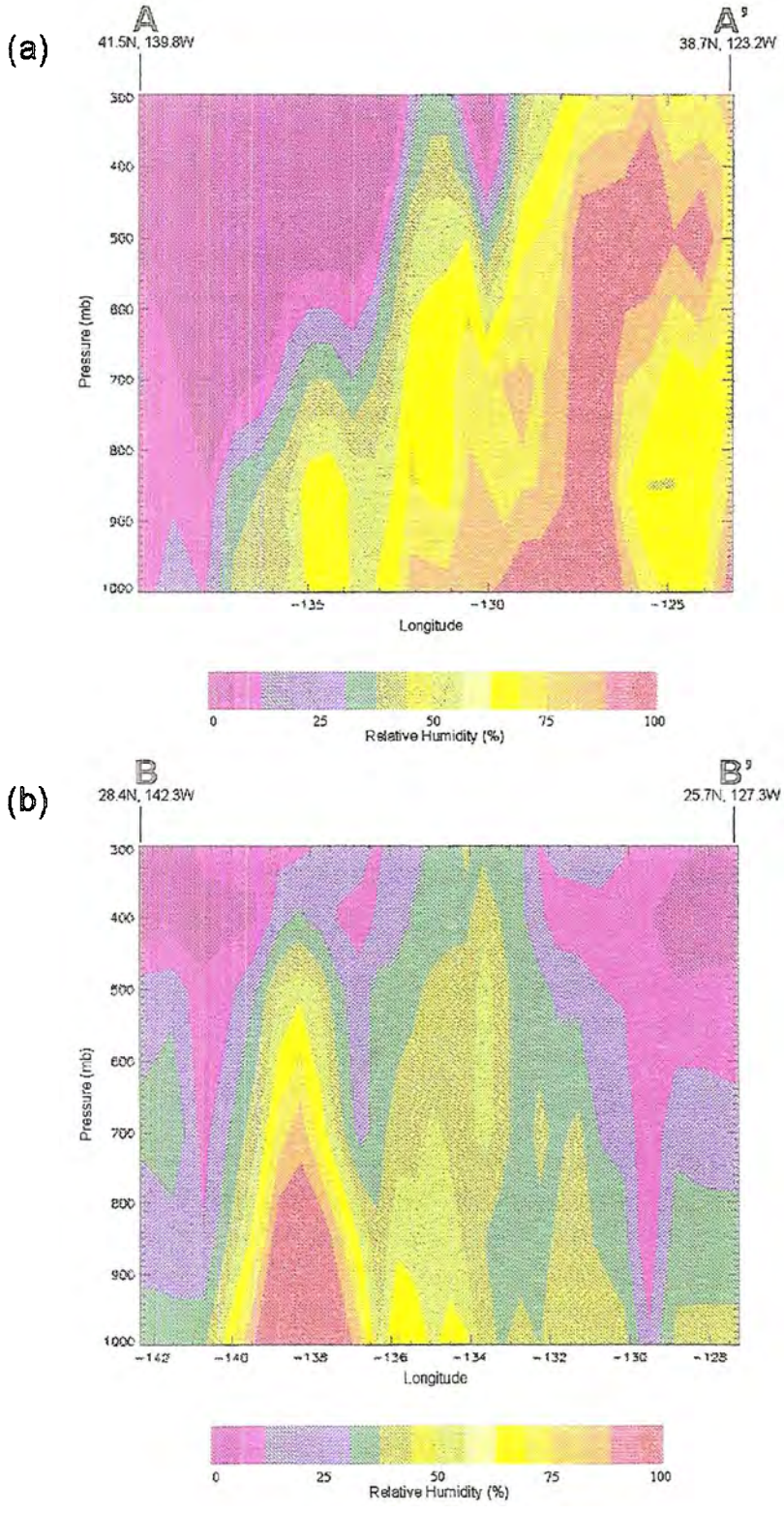

Figure 4.9. Relative humidity profiles A-A' (a) and B-B' (b) for the February 8, 1996 subtropical plume.

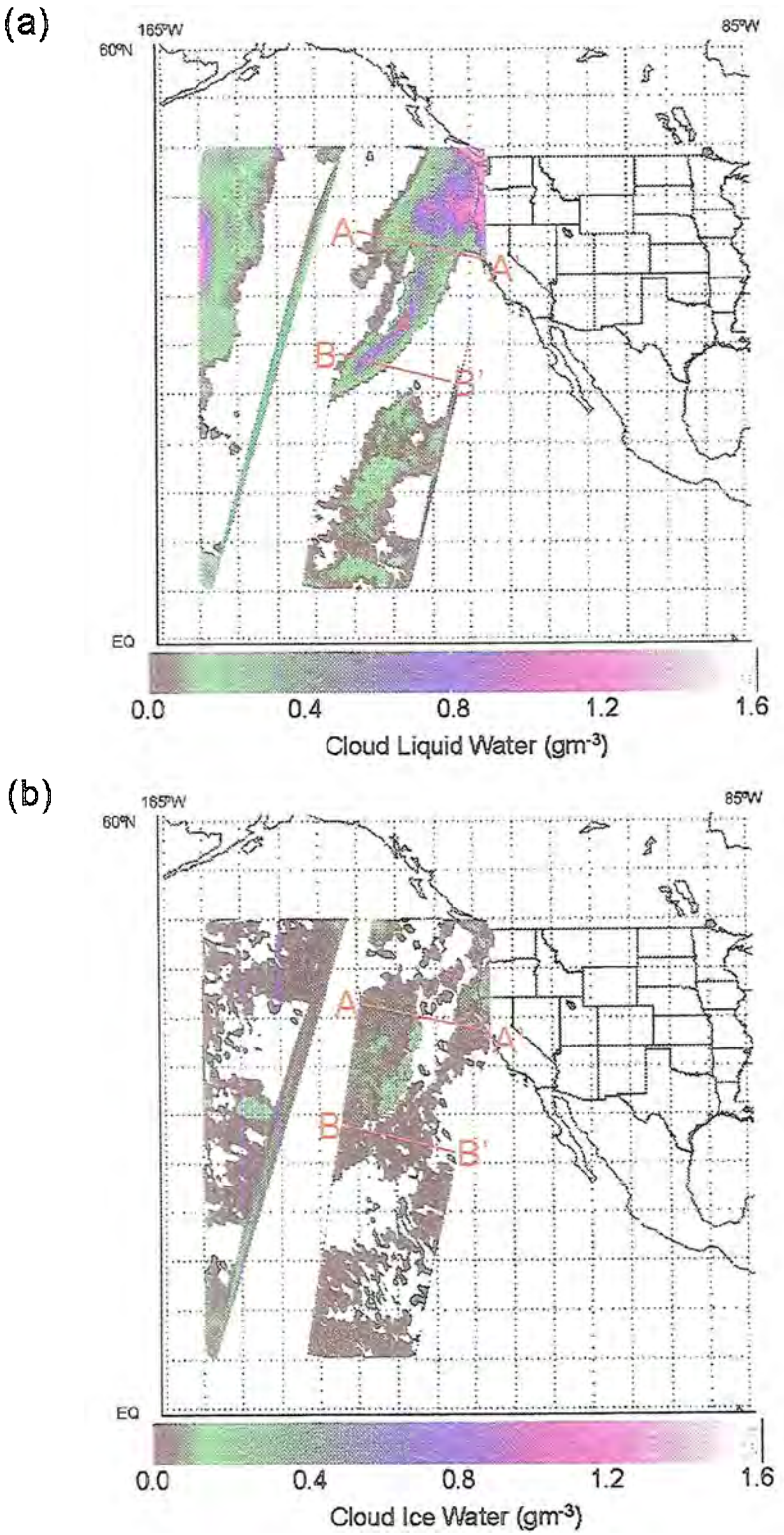

Figure 4.10. Cloud liquid water (a) and cloud ice water (b) for the February 8, 1996 subtropical plume. Vertical cross sections A-A' and B-B' are indicated.

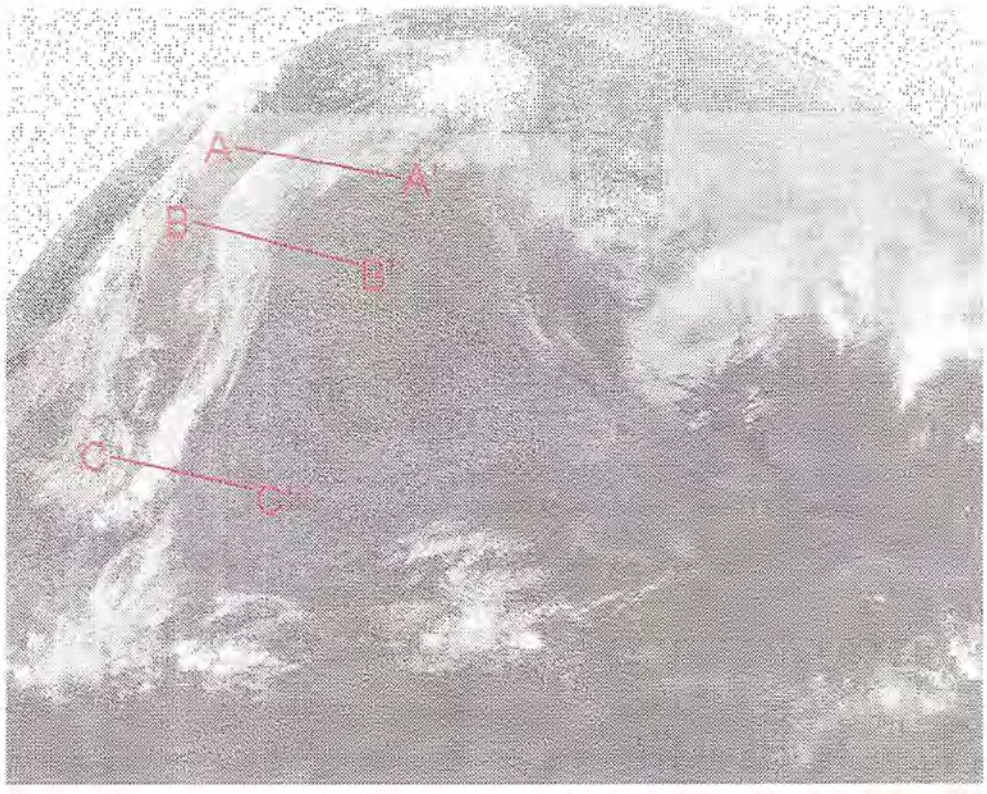

Figure 4.11. GOES-West IR image, January 1, 1996 tropical-polar plume. Vertical cross sections A-A', B-B', and C-C' are indicated.

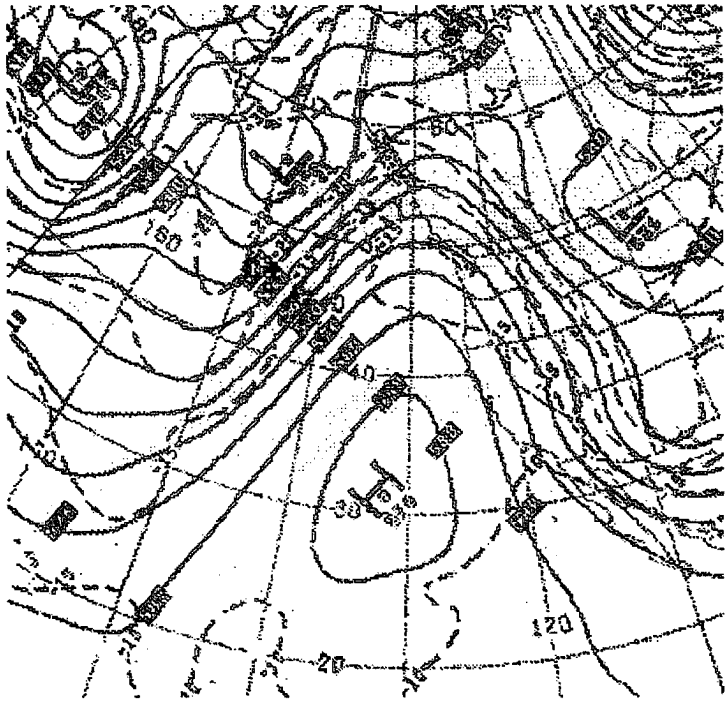

Figure 4.12. 500-mb analysis, January 1, 1996.

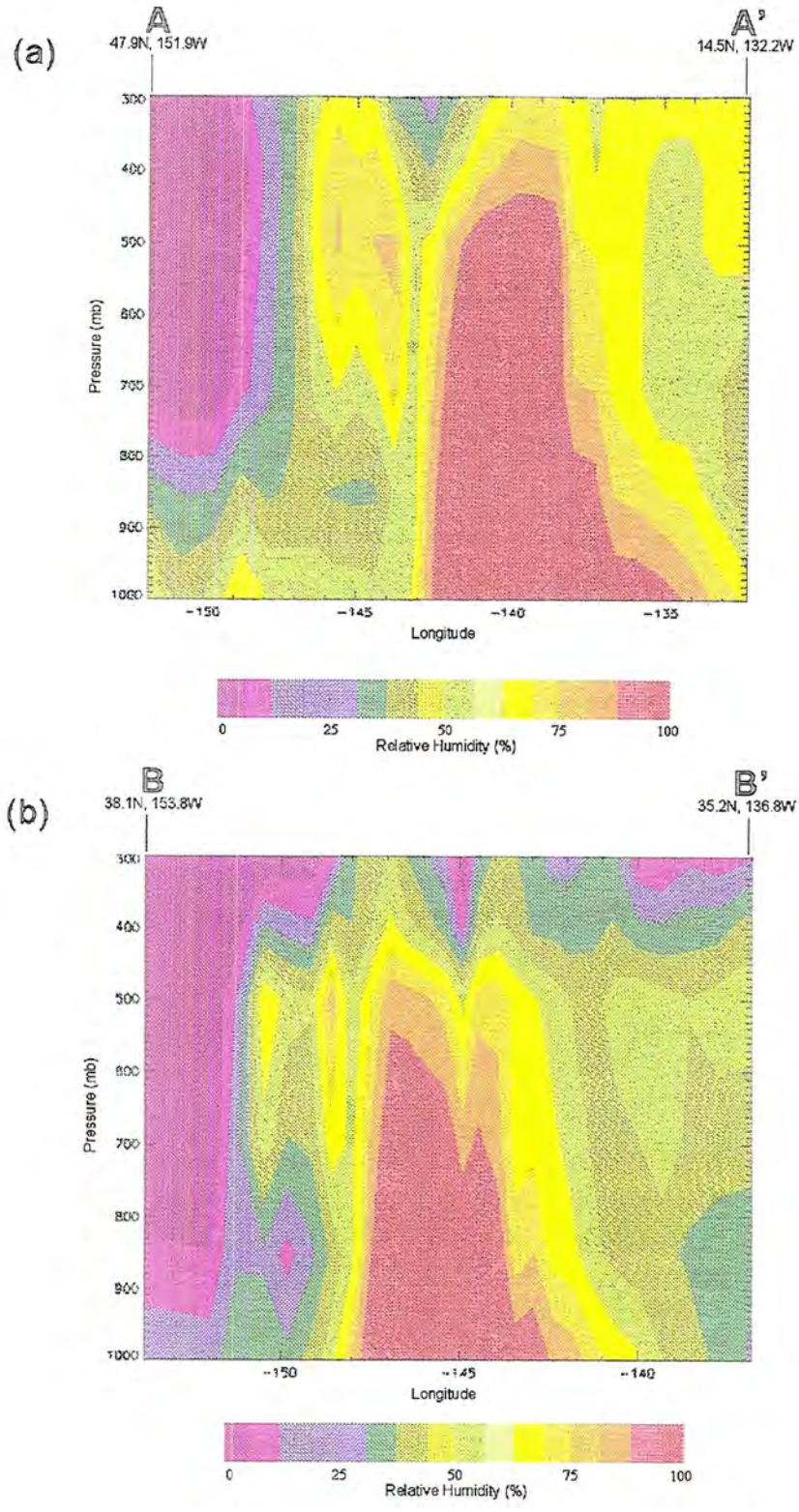

Figure 4.13. Relative humidity profiles A-A' (a), B-B' (b), and C-C' (c), for the January 1, 1996 tropical-polar plume.

(c)

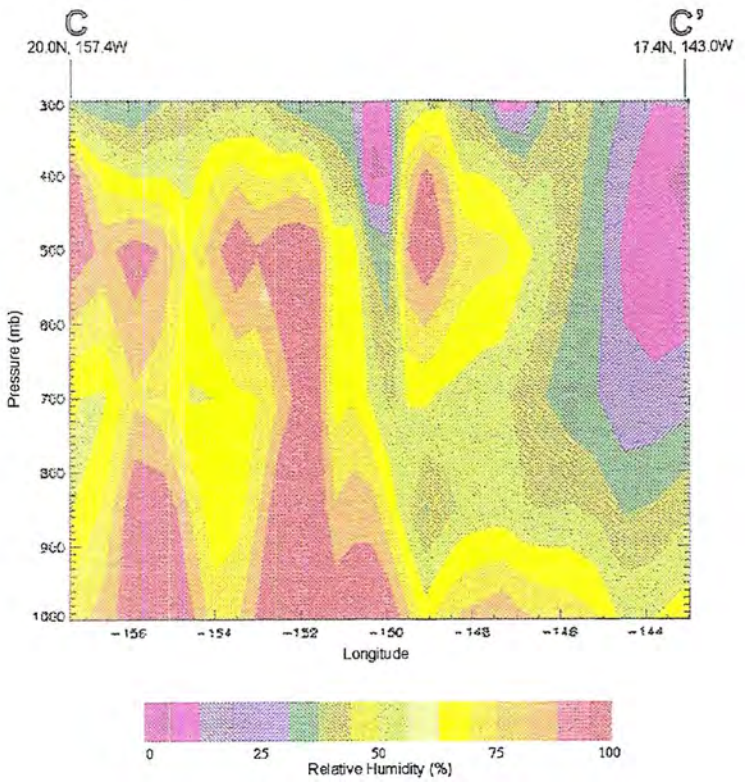

Figure 4.13. (cont.)

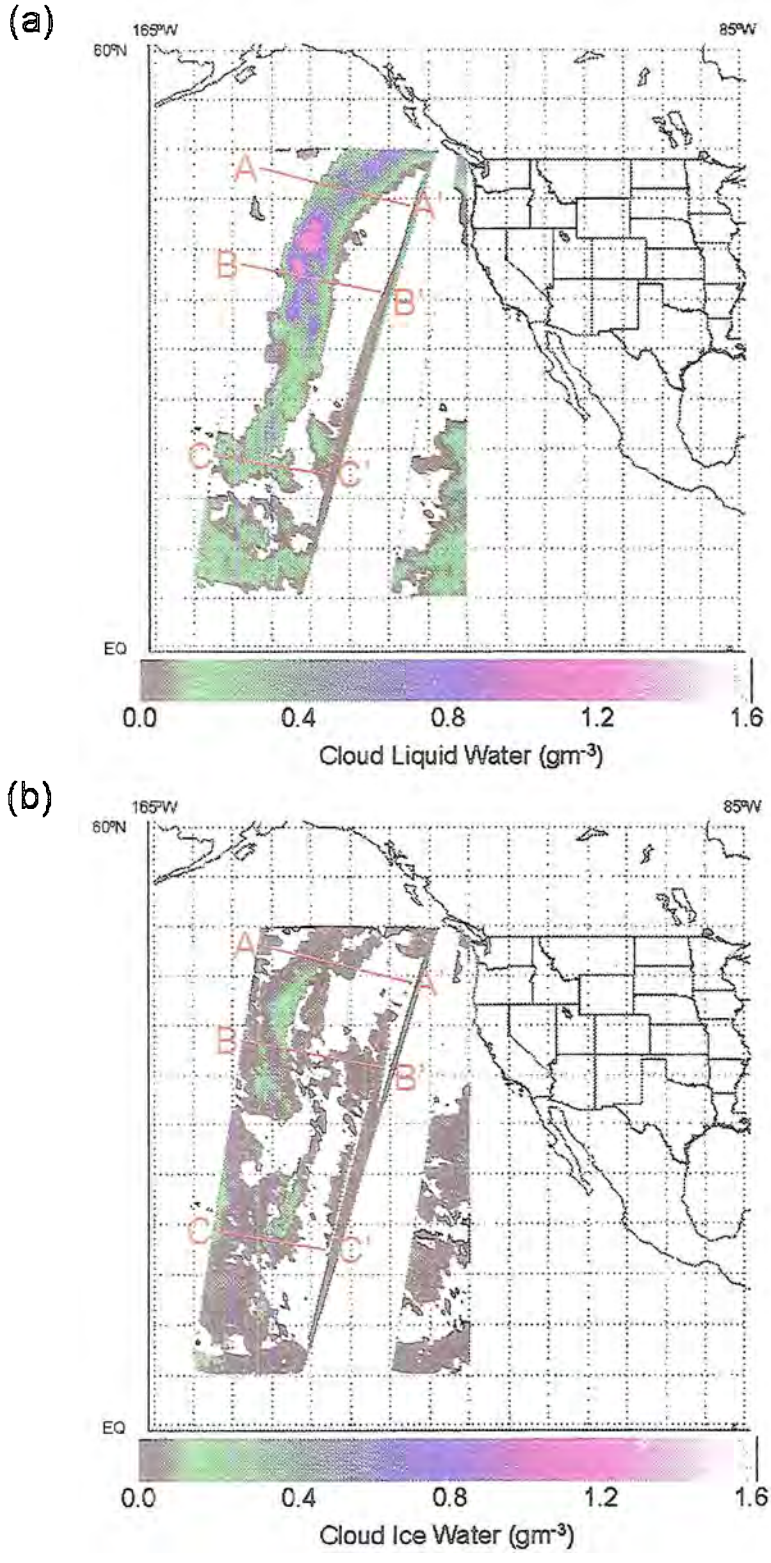

Figure 4.14. Cloud liquid water (a) and cloud ice water (b) for the January 1, 1996 tropical-polar plume. Vertical cross sections A-A', B-B', and C-C' are indicated.

5. Moisture Transport

It is instructive to determine what role moisture plumes play in transporting moisture poleward from the tropics and subtropics. As has been previously mentioned, moisture plumes do impact the west coast of North America, with occasionally disastrous consequences (e.g. heavy rains, flooding). The moisture found within these plumes represents a potential source of precipitation once the moisture plume reaches the coast. Additionally, it is instructive to know at which atmospheric *levels* the moisture transport is a maximum. This chapter discusses the results of moisture transport calculations (Section 3.3) done for each of the moisture plume case studies (Table 4.1). In the sections that follow, all discussion on plume-related moisture transport refers to moisture transport occurring along the *main axis* of the moisture plume (defined in Chapter 4).

5.1 Classic plumes

The moisture transport (combined zonal/meridional transport) over the entire tropospheric column and the moisture transport for each of the BWR-retrieved levels are shown in Figure 5.1 for the March 25, 1996 classic plume case study. At 1000 mb, it is somewhat difficult to distinguish the moisture transport occurring within the moisture plume from that occurring in the surrounding areas (Figure 5.1a). It may be that the surface (or boundary layer) winds do not represent the general synoptic circulations at the overlying atmospheric levels.

The circulation of the upper levels becomes more apparent at 850 mb (Figure 5.1b) and 700 mb (Figure 5.1c). It is at these pressure levels that the moisture transport within the moisture plume becomes more discernable from the transport outside the plume. The maximum values observed at these two levels are both above 200 $gkg^{-1}ms^{-1}$ (Tables A.4 and A.5) and are among the highest of the 6 BWR-retrieved levels. Hence, the 850 mb and 700 mb levels both appear to be primary contributors to the total tropospheric moisture transport (Figure 5.1g) within the moisture plume.

The 500-mb level (Figure 5.1d) indicates moisture transport both in areas where liquid clouds are indicated and in areas where ice clouds are indicated (see Figure 4.5). The moisture transport occurring in areas with liquid cloud might be due to higher-level liquid clouds present at the 500-mb level. This level also contributes substantially to the total tropospheric moisture transport. Maximum values within the plume are above 200 $gkg^{-1}ms^{-1}$ (Table A.6).

For most of the case studies in this project, the moisture transports at 400 mb and 300 mb were generally much smaller than the transports occurring at lower levels. For this case study (March 25, 1996), however, both the 400-mb (Figure 5.1e) and 300-mb (Figure 5.1f) transports are quite substantial. The maximum transport at 400 mb is well over 130 $gkg^{-1}ms^{-1}$ (Table A.7), while the maximum transport at 300 mb is just over 60 $gkg^{-1}ms^{-1}$ (Table A.8). In most of the case studies, the highest moisture transports at these two levels occurred in areas where notable ice cloud was indicated by BWR. Although the GOES image of this case study (Figure 4.1) indicates that plenty of high (ice) cloud exists in this moisture plume, the BWR-retrieved cloud ice water (Figure 4.5b) indicates less extensive areas of ice cloud in general within the plume than in the first case study. Hence, it is unclear how much of the moisture transport at 300 mb and 400 mb is actually due to ice cloud.

5.2 Subtropical plumes

For the February 8, 1996 subtropical plume case study, moisture transport is somewhat apparent within the plume at 1000 mb (Figure 5.2a). This moisture transport, with maximum values reaching over 150 $gkg^{-1}ms^{-1}$ (Table A.3), is primarily found in areas where liquid cloud is indicated (Figure 4.10). Much of the total transport (Figure 5.2g) is comprised of the moisture transports occurring at 850 mb (Figure 5.2b) and 700 mb (Figure 5.2c). Both levels exhibit maximum transports of over 250 $gkg^{-1}ms^{-1}$, the highest values of any of the retrieved atmospheric levels (see Tables A.4 and A.5). Most of the moisture transport occurring in these two layers is, like the 1000-mb layer, found in areas where liquid cloud is prevalent. At 500 mb (Figure 5.2d), moisture transport within the plume is still clearly defined. Maximum values of moisture transport at this level reach about 160 $gkg^{-1}ms^{-1}$.

Moisture transport is also evident at both 400 mb (Figure 5.2e) and 300 mb (Figure 5.2f), although the overall values are greatly reduced. Maximum transport values for the 400-mb and 300-mb layers are 45 $gkg^{-1}ms^{-1}$ and 21 $gkg^{-1}ms^{-1}$, respectively (Tables A.7 and A.8). The greatest moisture transport at these two levels occurs roughly in the same regions where notable ice cloud is indicated by the BWR algorithm (Figure 4.10b). Compared with the corresponding values for the classic plume case study discussed earlier, one can see that these values are much smaller. This finding seems to support the findings in Chapter 4, which indicate that, of the three plume classes, subtropical plumes are most likely to be low-level events (see Section 4.4). The decreased moisture transports at 300 mb and 400 mb are also seen in the summary statistics for the ten subtropical-plume case studies (Tables 5.5 and 5.6).

5.3 Tropical-polar plumes

For the January 1, 1996 tropical-polar plume, as with the two case studies discussed so far, the moisture transport occurring within the plume itself is most evident between the 850-mb and 500-mb levels (Figures 5.3b-5.3d). The greatest moisture transport values are found at 850 mb and 700 mb, with the maximum transport within the plume being approximately 200 $gkg^{-1}ms^{-1}$ at both levels (Tables A.4 and A.5). As a result, these levels contribute largely to the total tropospheric moisture transport (Figure 5.3g, Table A.9).

At the 400-mb and 300-mb levels (Figures 5.3e and 5.3f), the maximum transports are 49 $gkg^{-1}ms^{-1}$ and 27 $gkg^{-1}ms^{-1}$, respectively (Tables A.7 and A.8). The maximum moisture transport appears to be confined to the convective areas near the south end of the plume, a few hundred kilometers east of Hawaii. Compared to the summary statistics for the 10 tropical-polar plume case studies (Tables 5.5 and 5.6), the values given above are quite small. The transport values at 300 mb and 400 mb for tropical-polar plumes are generally comparable with the corresponding values for classic plumes.

A relative lack of upper-level moisture transport is also indicated at 500 mb (Figure 5.3d). Although the maximum calculated moisture transport at this level is nearly 120 $gkg^{-1}ms^{-1}$ (Table A.6), the only appreciable moisture transport occurs in the region of convection at the south end of the plume. Transports elsewhere along the plume are generally less than 50 $gkg^{-1}ms^{-1}$.

5.4 Summary

Summary statistics of the moisture transports at each BWR-retrieved level and the total tropospheric moisture transport are presented in Tables 5.1-5.7. The plumes that originate in the tropical regions (i.e. classic, tropical-polar plumes) generally have higher moisture transports at all levels than do the plumes of subtropical origin, as is indicated

in Table 5.7. Of the two plume classes that have tropical origins, the classic plumes generally had the higher moisture transports at the 1000-mb and 850-mb levels, while the tropical-polar plumes generally had the higher moisture transports at and above 700 mb.

From the results in sections 5.1-5.3, a few general observations can be made concerning the vertical variation of moisture transport within moisture plumes. Little consideration was given to the moisture transports at 1000 mb, as the transport patterns at this level were usually quite different from the transport patterns evident at higher levels. This is possibly due to surface and boundary layer wind effects. The greatest contribution to the total tropospheric moisture transport within moisture plumes appears to come from the 500-850 mb levels. The regions with high moisture transport at the 500-850 mb levels often correspond to regions containing higher amounts of cloud liquid water. Above 500 mb, the magnitudes of moisture transport drop off considerably. The greatest moisture transport at the uppermost levels is limited primarily to those areas where ice cloud is present. Typical total tropospheric moisture transports (Table 5.7) are on the order of 10^5 $gm^{-1}s^{-1}$. These values generally match the values found by Thompson and McGuirk (1987).

It is also instructive to briefly compare the moisture transports found in moisture plumes to the average wintertime values of moisture transport observed in the subtropical and midlatitude regions of the eastern Pacific Ocean. The results from Table 5.7 were compared to a 1984-1993 winter (DJF) average of total tropospheric moisture transport generated from ECMWF reanalysis data (Figure 5.4). The 1984-1993 winter average shows that the total tropospheric transport over the eastern Pacific Ocean is greatest within the westerlies near the midlatitude jet stream, with values between 1-$2X10^5$ $gm^{-1}s^{-1}$. The subtropical regions off the North American coast exhibit the lowest transports, with values on the order of 10^4 $gm^{-1}s^{-1}$. Comparing these magnitudes with

those presented in Table 5.7, the mean moisture transports occurring within plumes are somewhat larger than the average transports found in the midlatitude baroclinic zone, and about an order of magnitude greater than the average transports found in the subtropics. This brief comparison suggests that moisture plumes are indeed an important mechanism for atmospheric moisture transport, making large short-term contributions to the transport of moisture out of the tropics and subtropics and into the midlatitudes during the winter and early spring.

All the results presented in this chapter are considered to be preliminary results. A more detailed study of moisture transports would be necessary in order to draw any definite conclusions about long-term transport characteristics. In addition, this chapter only discusses the moisture transports occurring within the moisture plume itself (along the main plume axis). In order to understand more completely the moisture transport patterns of moisture plumes, future work should, in addition, look at the moisture transports occurring in areas *adjacent* to moisture plumes.

Table 5.1. Summary statistics for 1000-mb moisture transport ($gkg^{-1}ms^{-1}$).

	Maximum	Mean	Standard Dev.	Coeff. of Var.
Classic	184.749	76.657	40.534	0.547
Subtropical	132.617	40.377	27.102	0.676
Tropical-polar	157.157	42.144	29.74	0.712

Table 5.2. Same as Table 5.1, except for 850-mb moisture transport ($gkg^{-1}ms^{-1}$).

	Maximum	Mean	Standard Dev.	Coeff. of Var.
Classic	239.154	71.18	43.896	0.624
Subtropical	179.374	45.405	33.457	0.757
Tropical-polar	199.755	48.566	35.008	0.733

Table 5.3. Same as Table 5.1, except for 700-mb moisture transport ($gkg^{-1}ms^{-1}$).

	Maximum	Mean	Standard Dev.	Coeff. of Var.
Classic	170.331	45.269	31.554	0.69
Subtropical	149.422	36.454	28.551	0.776
Tropical-polar	184.372	42.715	33.869	0.823

Table 5.4. Same as Table 5.1, except for 500-mb moisture transport ($gkg^{-1}ms^{-1}$).

	Maximum	Mean	Standard Dev.	Coeff. of Var.
Classic	132.778	31.128	27.335	0.863
Subtropical	97.567	16.236	18.004	1.137
Tropical-polar	149.151	32.633	32.018	1.042

Table 5.5. Same as Table 5.1, except for 400-mb moisture transport ($gkg^{-1}ms^{-1}$).

	Maximum	Mean	Standard Dev.	Coeff. of Var.
Classic	72.318	14.994	15.968	1.091
Subtropical	34.843	3.774	5.389	1.6
Tropical-polar	81.183	12.696	14.144	1.272

Table 5.6. Same as Table 5.1, except for 300-mb moisture transport ($gkg^{-1}ms^{-1}$).

	Maximum	Mean	Standard Dev.	Coeff. of Var.
Classic	38.77	7.861	8.402	1.122
Subtropical	21.94	2.036	2.969	1.712
Tropical-polar	34.87	5.495	6.355	1.373

Table 5.7. Same as Table 5.1, except moisture transport over atmospheric column ($X10^5\ gm^{-1}s^{-1}$).

	Maximum	Mean	Standard Dev.	Coeff. of Var.
Classic	8.214	3.310	1.464	0.434
Subtropical	6.275	2.023	1.188	0.596
Tropical-polar	7.848	2.536	1.446	0.586

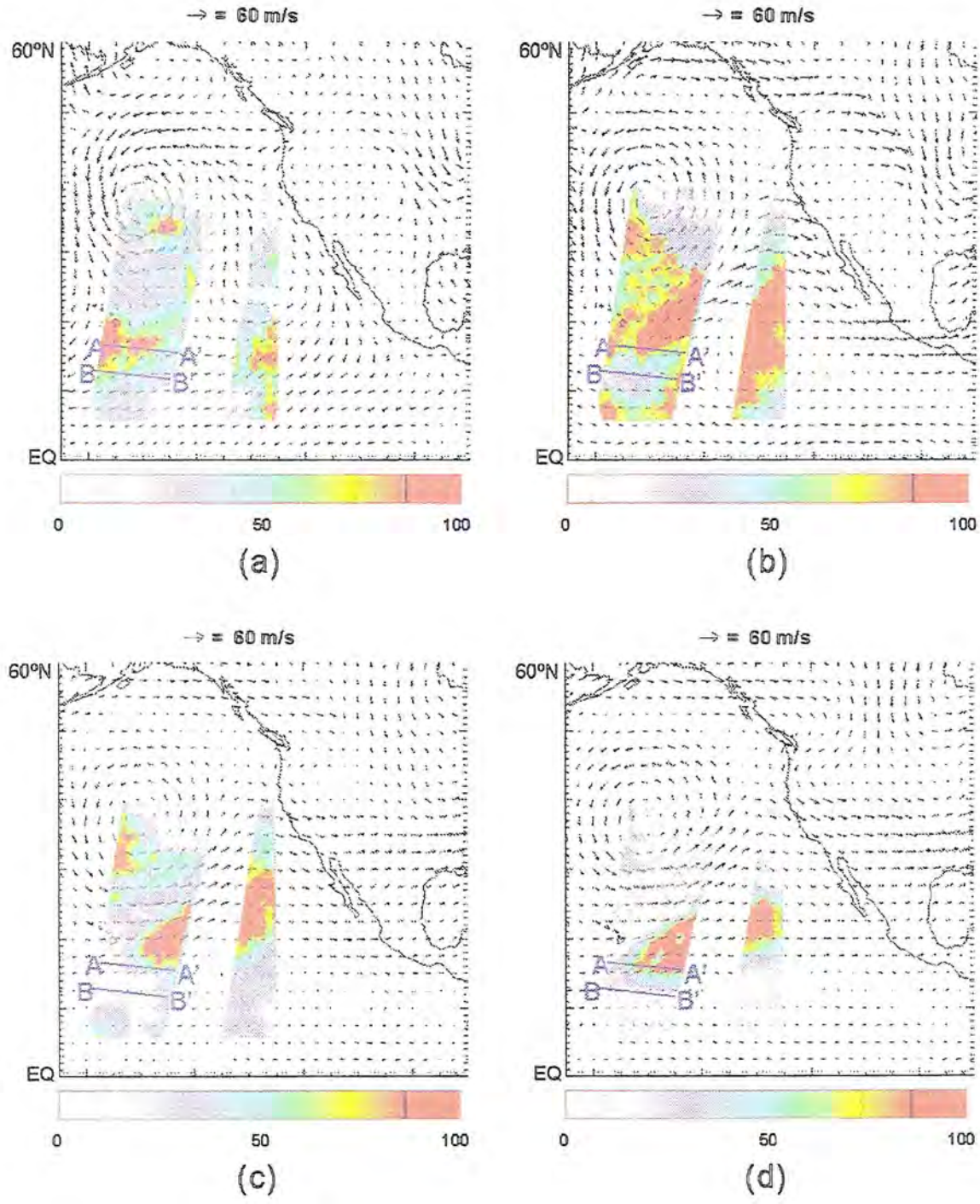

Figure 5.1. Moisture transports ($gkg^{-1}ms^{-1}$) at 1000 mb (a), 850 mb (b), 700 mb (c) 500 mb (d), 400 mb (e), and 300 mb (f), along with the moisture transport (in $gm^{-1}s^{-1}$) over the entire tropospheric column (g), for the March 25, 1996 classic plume. The wind data in (a)-(f) are taken from NCEP reanalysis. The vertical cross sections discussed earlier are also shown.

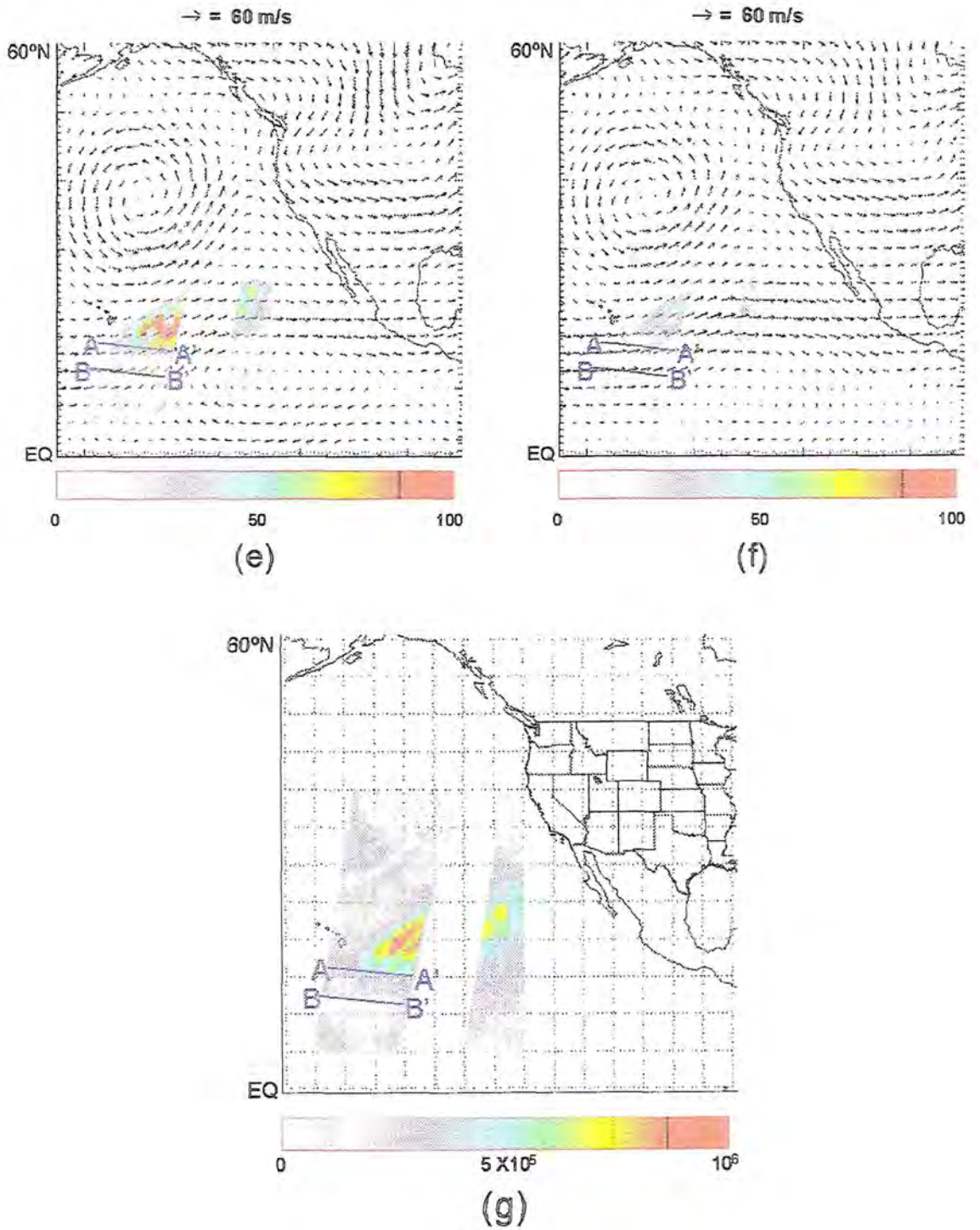

Figure 5.1. (cont.)

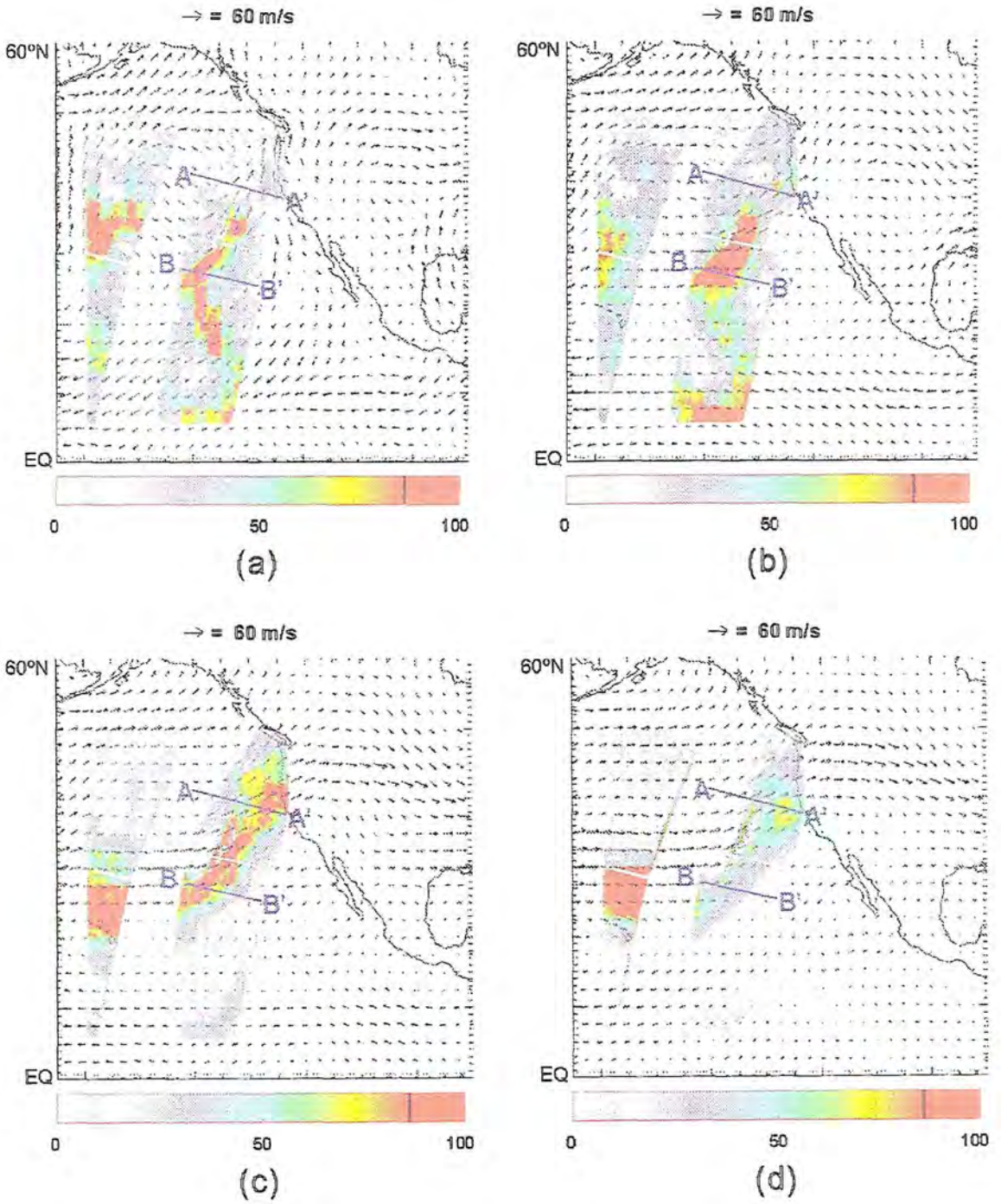

Figure 5.2. Same as Figure 5.1, except for the February 8, 1996 subtropical plume.

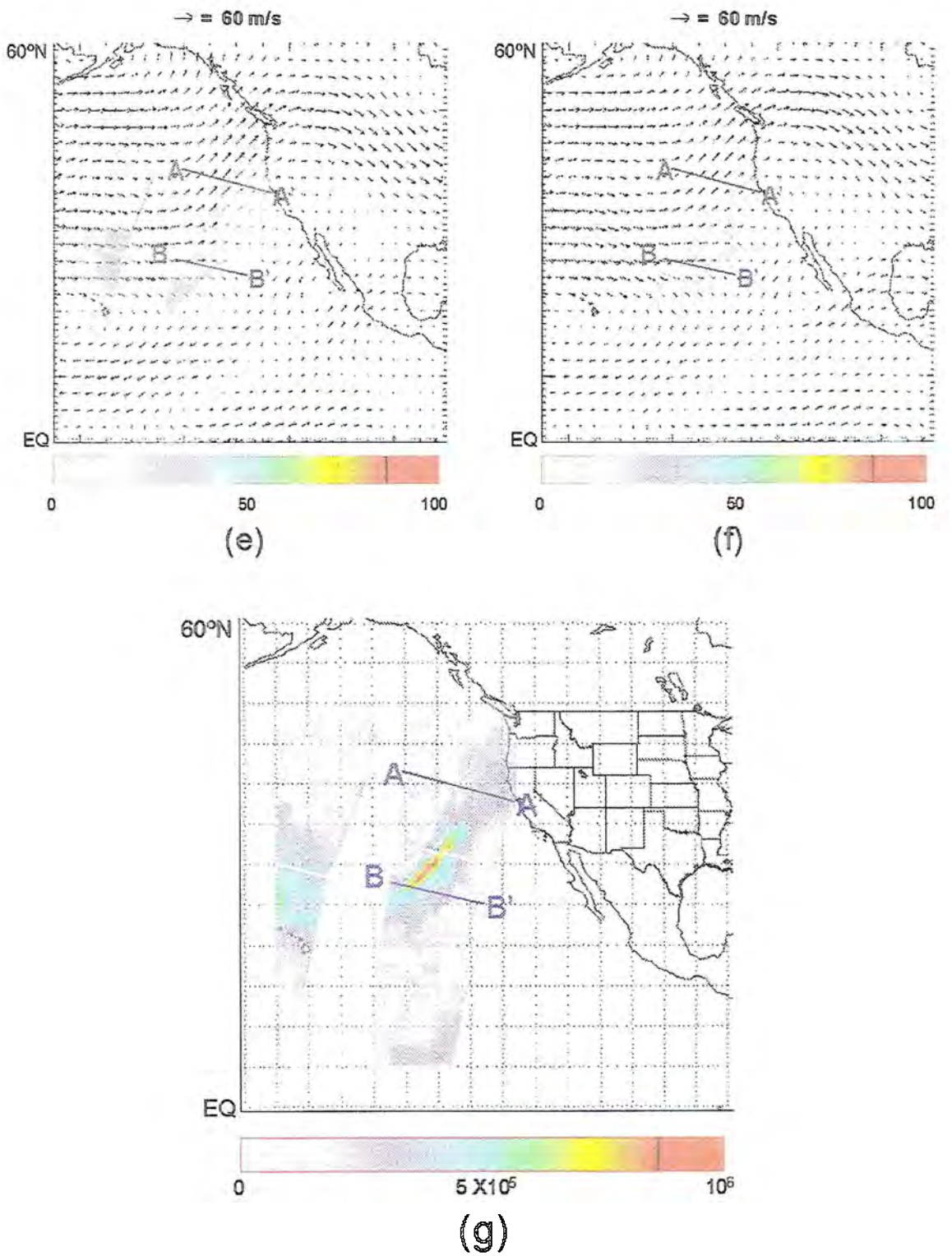

Figure 5.2. (cont.)

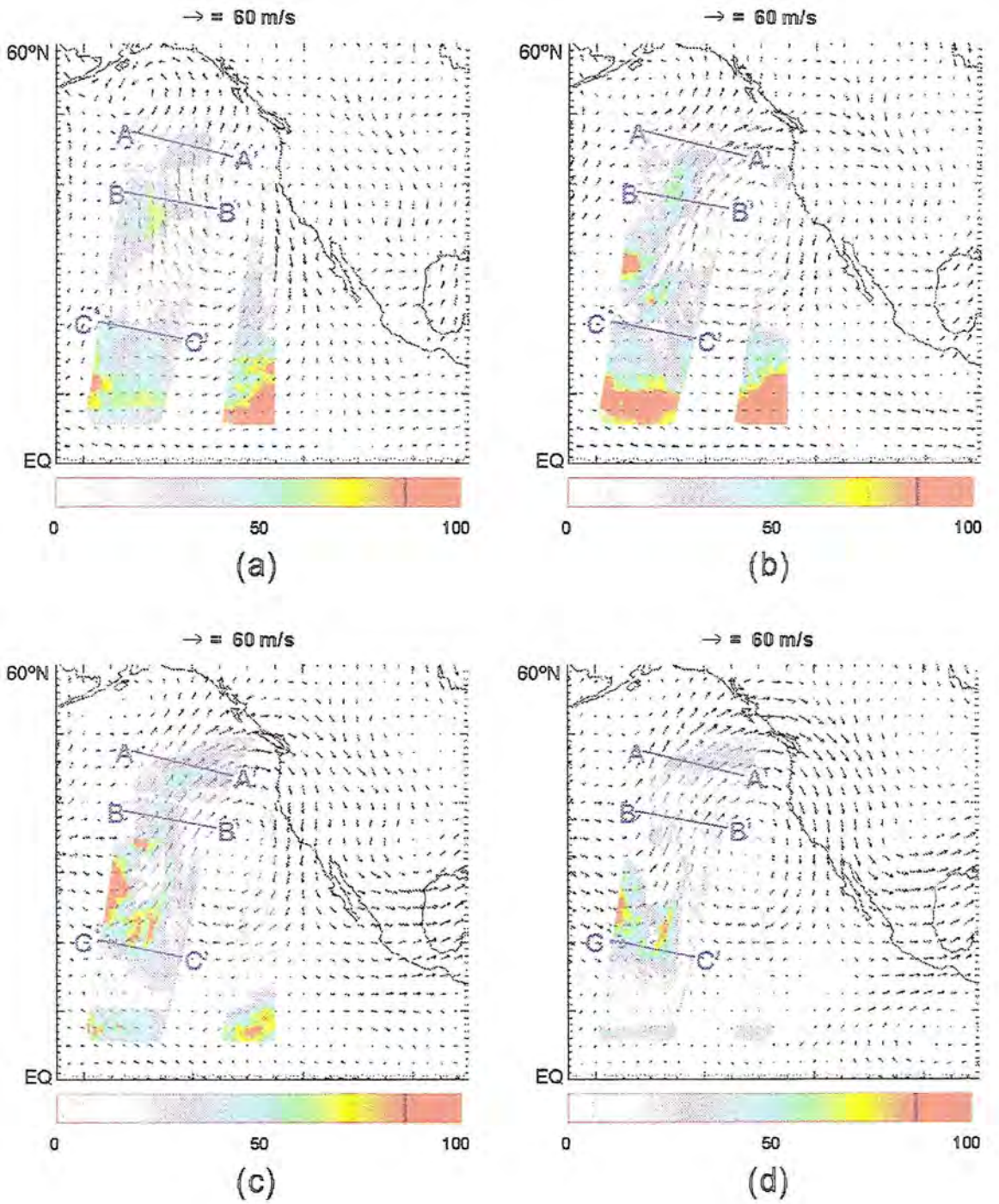

Figure 5.3. Same as Figure 5.1, except for the January 1, 1996 tropical-polar plume.

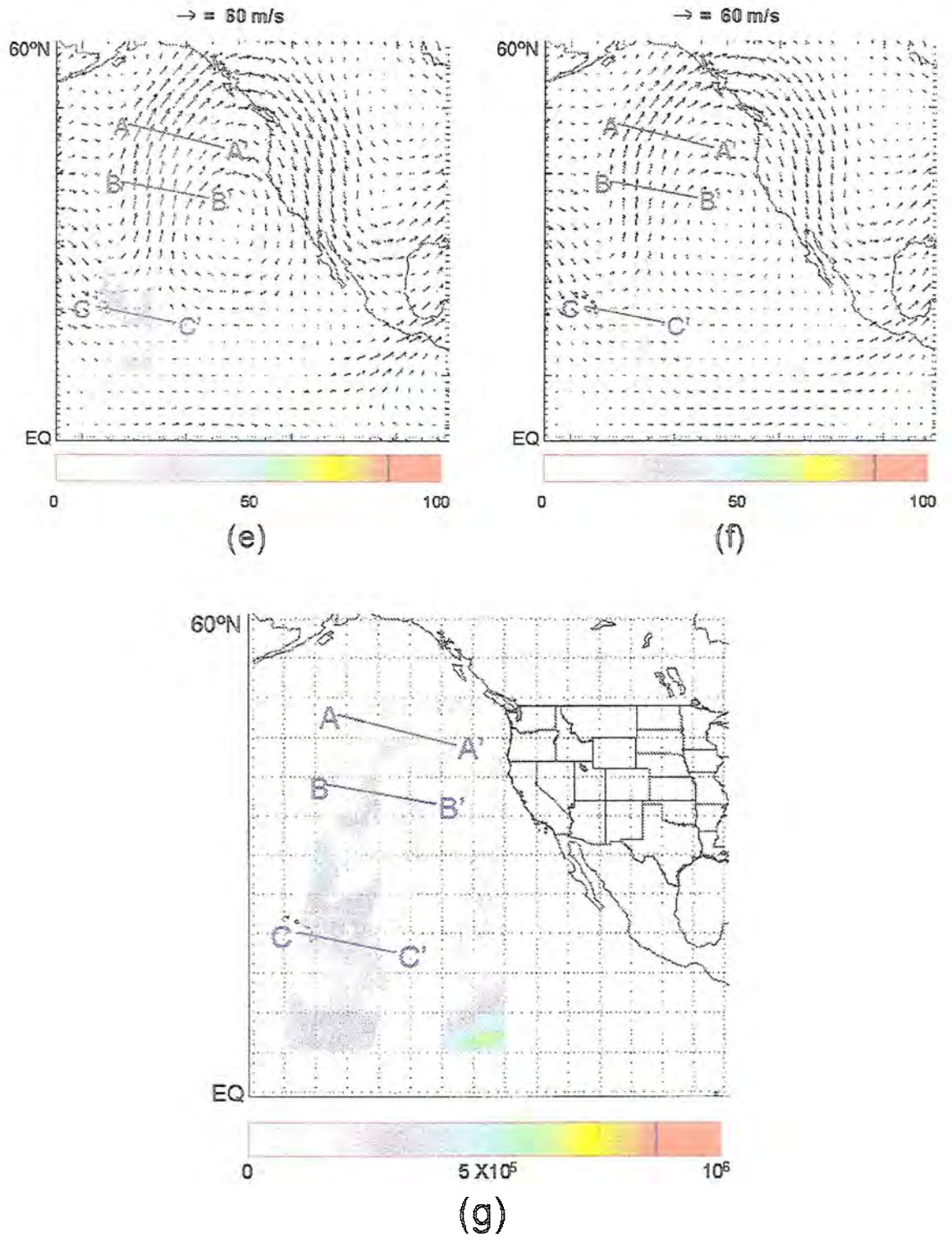

Figure 5.3. (cont.)

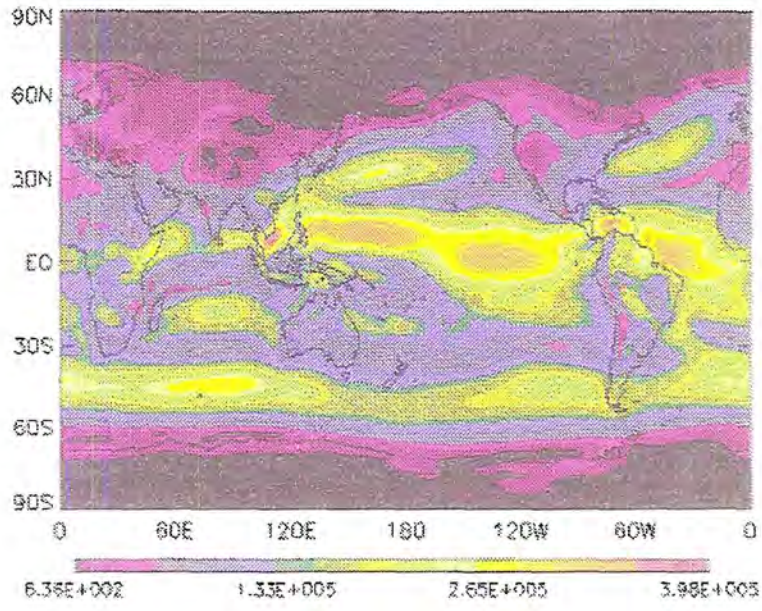

Figure 5.4. Total atmospheric moisture transport ($gm^{-1}s^{-1}$), 1984-1993 winter (DJF) average. The specific humidity and wind data used to calculate moisture transport were obtained from the ECMWF reanalysis product.

6. Retrieval Evaluation

6.1 Probability indices

The BWR algorithm uses three probability indices to indicate how closely the simulated atmospheric state matches the real atmospheric state. These indices are the prior, forward, and posterior probabilities, which are defined in Chapter 3. Higher probabilities represent an increased confidence that the simulated (retrieved) atmospheric state matches the real atmospheric state.

The prior probability is an indicator, at a given retrieval location, of how closely the *a priori* information (Section 3.2.2) about the atmospheric state (relative humidity, temperature, etc.) matches the actual atmospheric state. Prior probability results from the three case studies discussed in this paper are provided in Figure 6.1. In all three cases, the highest probabilities (above 50%) occur in regions that are either clear or have very few clouds present. These conditions are most commonly found in the subtropics. On the other hand, lower probabilities are often found in regions where significant cloud cover is present. Probabilities of 20% or less are found in areas where substantial liquid cloud is indicated (e.g., compare Figure 6.1b and Figure 4.10a). The liquid clouds referred to here are those clouds associated with substantial low level convection and do not usually include non-convective low-level stratus clouds. Small prior probabilities (< 20%) can also be found in regions where substantial ice cloud is indicated (e.g., compare Figure 6.1a and Figure 4.5b). These results might be explained

by recalling that the prior information consists of *monthly means* of relative humidity and temperature profiles over the study region. The daily profiles at a given location can be highly variable and, in some cases, not be well represented by the *a priori* data, especially for cloudy/stormy conditions.

The forward probability basically shows how well the Radiative Transfer (RT) module (Section 3.2.3) of the BWR algorithm is performing. It indicates how closely the simulated brightness temperature at each SSM/T-2 channel (i.e. the simulated radiance from the atmospheric level sensed by the SSM/T-2 channel - see Figure 3.2) calculated by the RT module matches the observed brightness temperatures at each SSM/T-2 channel (the observed radiance from the respective atmospheric level). Unlike the prior probability, the forward probability does not decrease substantially in the presence of liquid cloud. Forward probability is almost exclusively negatively affected by ice cloud (e.g. compare Figure 6.2a and Figure 4.5b), where values are often less than 20%. Although BWR does attempt to account for the effects of ice scattering of MW radiation (Lietzke, 1998), the algorithm only allows for a single ice cloud layer with a thickness of 1 km (see Table 3.5). Hence, the algorithm would likely have difficulty representing thick (> 1 km) and/or multi-layered ice clouds. Another problem is that ice clouds are often indicated in areas where heavier precipitation is occurring, such as in areas with deep convection. The RT module of the BWR algorithm is not designed to handle precipitation; it only handles non-precipitating liquid and ice clouds. Forward probabilities are greatest for cloud-free regions, with values around 60% and greater.

Finally, the posterior probability (Figure 6.3) combines the results from the forward and prior probabilities and is a final indicator of how accurately the BWR-calculated atmospheric state matches the actual atmospheric state at a given retrieval location. In areas where no liquid or ice cloud is indicated, the posterior probability can approach

values of 60%. In the regions where liquid and/or ice cloud is indicated, however, these values drop off to 20% and less.

6.2 Observed vs. simulated brightness temperatures

The differences between the observed and the BWR-calculated MW brightness temperatures at each SSM/T-2 channel are, like the forward probability, indicators of how well the RT module of the BWR algorithm is reproducing the observed brightness temperatures. Retrievals for which the brightness temperature differences are less than about 1K are considered to be good retrievals; i.e., the calculated atmospheric state is very likely to be representative of the actual atmospheric state. Retrievals for which the brightness temperature differences exceed 1K usually exhibit low forward probabilities, thus indicating poor retrieval performance. The value of 1K used to distinguish the good retrievals from the poor retrievals is the approximate value of the overall retrieval noise (see the description of C_y-Table 3.3), which is the sum of the SSM/T-2 instrument noise (Table 3.1) and the radiative transfer model error (Lietzke, 1998).

For the 92 GHz channel of the SSM/T-2 sensor, the largest differences between the observed and simulated MW brightness temperatures (Figure 6.4) occur in regions where abundant ice cloud is indicated. At these locations, the observed brightness temperature is usually less than the BWR-calculated brightness temperature. Liquid cloud can also affect the difference between the two brightness temperatures, although to a much lesser extent than ice cloud. The observed brightness temperature is usually greater than the simulated brightness temperature in regions with liquid cloud.

Figure 6.5 illustrates the brightness temperature difference patterns for 150 GHz. The 150 GHz channel is sensitive to both liquid and ice cloud. For areas where liquid cloud is indicated, the observed brightness temperature is usually greater than the simulated brightness temperature, as was the case for the 92 GHz channel. For regions

where ice cloud is indicated, the observed brightness temperatures can be either greater or less than the simulated brightness temperatures.

All of the SSM/T-2 channels near 183 GHz exhibit similar behaviors with respect to simulated brightness temperatures. For brevity, the results for the 183±1 GHz channel are shown here (Figure 6.6). The 183±1 GHz channel is sensitive to both liquid and ice cloud. The observed brightness temperatures are usually greater than the simulated brightness temperatures for areas with liquid cloud and/or areas with small amounts of ice cloud. However, in areas where both substantial liquid and ice cloud is indicated (e.g. deep convection), the observed brightness temperatures can be either greater or less than the simulated brightness temperatures.

6.3 Surface observation validation

For several of the 30 moisture plume case studies in this project, SSM/T-2 overpasses were available for moisture plumes that passed directly over the Hawaiian Islands. These cases provide an excellent preliminary comparison of the BWR-retrieved RH profiles with those obtained from surface observations. Rawinsonde data was obtained from Hilo and Lihue and compared to the nearest (both spatially and temporally) SSM/T-2 observation.

The BWR-retrieved atmospheric profiles and the rawinsonde profiles tend to match most closely in conditions where there is abundant low-level moisture but very little upper-level moisture. As Figure 6.7 shows, the differences between the two profiles are generally small below about 850 mb (< 10%). This difference tends to increase at the upper levels. Although both profiles do depict the very dry upper atmosphere, their RH values differ by as much as 20% in these regions.

As the upper atmosphere becomes moister, there is progressively less agreement between the BWR and rawinsonde profiles. Figure 6.8 shows two profile comparisons

for the subtropical plume case study on February 8, 1996 (Sections 4.2 and 5.2). Increased upper-level moisture (compared to Figure 6.7) is evident in the rawinsonde profiles. At most levels, the BWR-retrieved profiles tend to match the moistening/drying trends of the rawinsonde profiles. However, the amplitudes of these trends are much less for the BWR-derived profiles. This sometimes leads to large differences (up to 30%) in RH values, especially where the rawinsonde profile indicates a local moist maximum or minimum. This behavior is probably linked to the noted decrease in BWR performance in cloudy/stormy conditions (see Section 6.1), where the BWR-retrieved atmospheric profiles are less likely to represent the actual atmospheric profiles.

On February 19, 1996, GOES IR imagery (not shown) indicated a very strong tropical-polar plume positioned directly over Hawaii. Relative humidities from the BWR and rawinsonde datasets differ by as much as 40-50% at a given atmospheric level (Figure 6.9). Little similarity exists between the moisture profiles of the two datasets for this case. The moisture maxima/minima indicated by BWR are generally located at, or a few hundred millibars below, the corresponding maxima/minima in the rawinsonde profiles (see also Figure 6.8b, below 850 mb).

It must be reemphasized that the BWR-retrieved profiles and the rawinsonde profiles were obtained at slightly different locations and times. The present work used the SSM/T-2 sensor aboard the DMSP F12 satellite, which passed over Hawaii at about 10AM and 10PM local time. Rawinsonde measurements, on the other hand, were made at 2AM and 2PM local time (12Z and 0Z, respectively). If possible, comparisons would be more accurate between BWR and rawinsonde profiles that are both 1) colocated and 2) measured at the same time.

6.4 Total precipitable water

It was desired to know how accurately the BWR algorithm retrieves the total moisture content in the atmospheric column (total precipitable water, or TPW) for a given retrieval. The TPW was derived from the relative humidity information provided by BWR. First, for each atmospheric level n, the specific humidity, q_n, was calculated from the relative humidity at that level (Equations 3.7 and 3.8). The specific humidity was then used to calculate TPW:

$$TPW = \frac{1}{g}\int q\,dp \approx \frac{1}{g}\sum_{n=1}^{6} q_n \Delta p_n \qquad (6.1)$$

The BWR-calculated TPW for the location was then compared to the corresponding TPW values from the NVAP dataset (Randel et al., 1996). Figure 6.10 shows some scatter plots that were used to check this relationship.

As the correlation coefficients presented in Figure 6.10 show, the BWR-derived and NVAP TPW values are generally well correlated. The BWR-derived TPW values tend to be higher than the NVAP values, however, with differences generally between 9 and 10 mm. This difference becomes more evident as one moves to higher TPW values. Hence, it appears that BWR tends to overestimate the moisture content of the atmosphere.

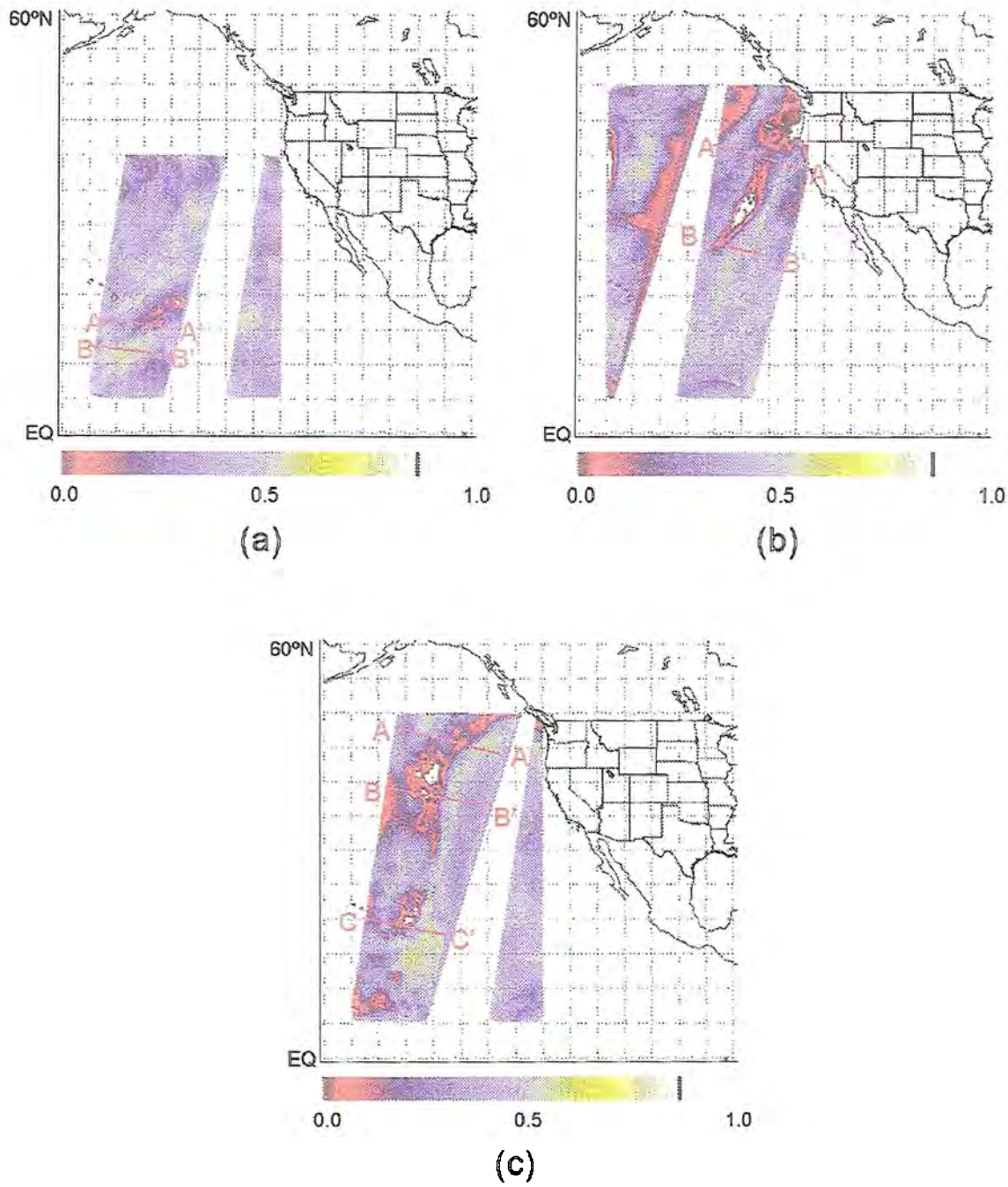

Figure 6.1. Prior probabilities for March 25, 1996 (a), February 8, 1996 (b), and January 1, 1996 (c). Previously discussed vertical profiles are also shown.

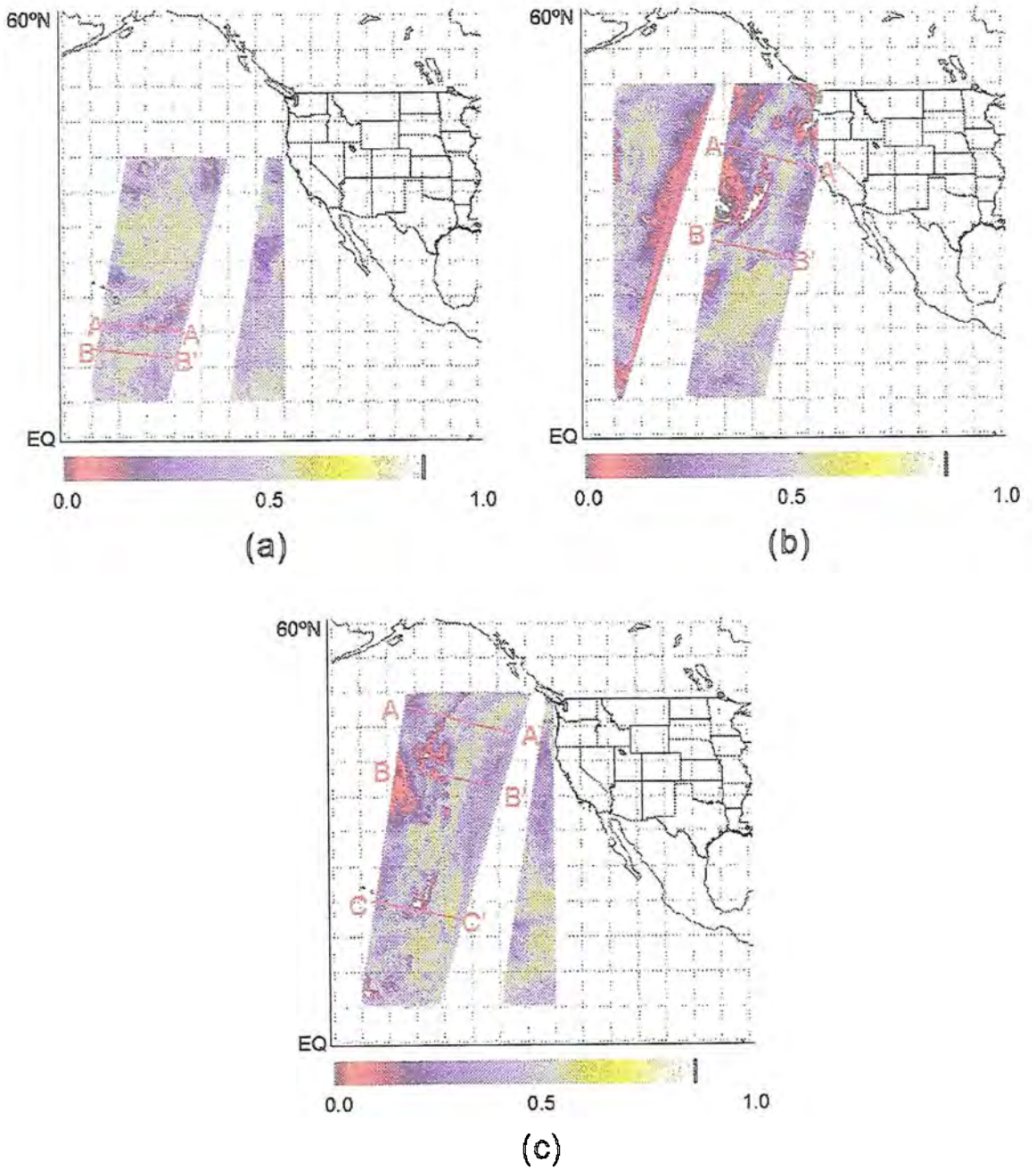

Figure 6.2. Same as Figure 6.1, except for forward probability.

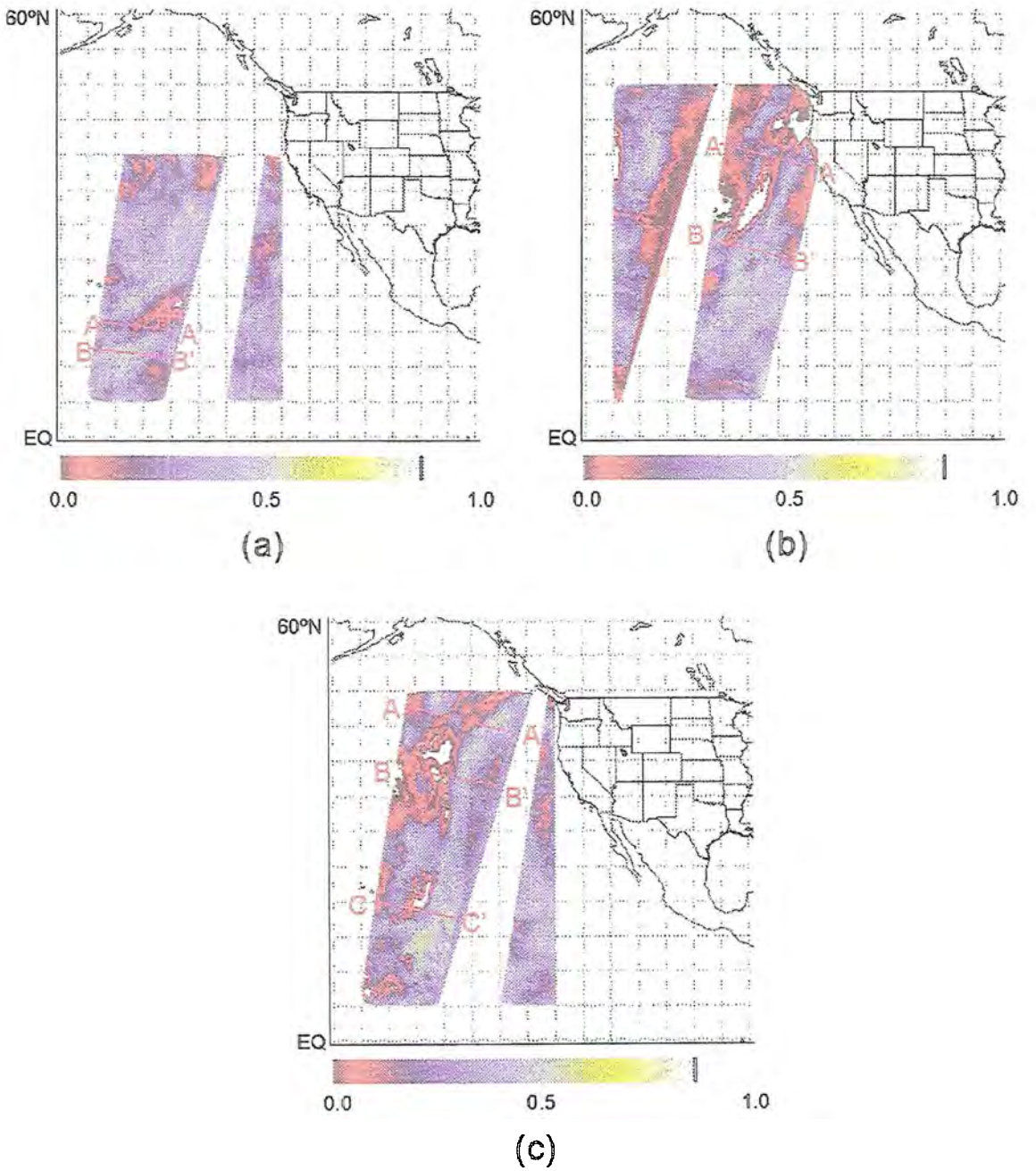

Figure 6.3. Same as Figure 6.1, except for posterior probability.

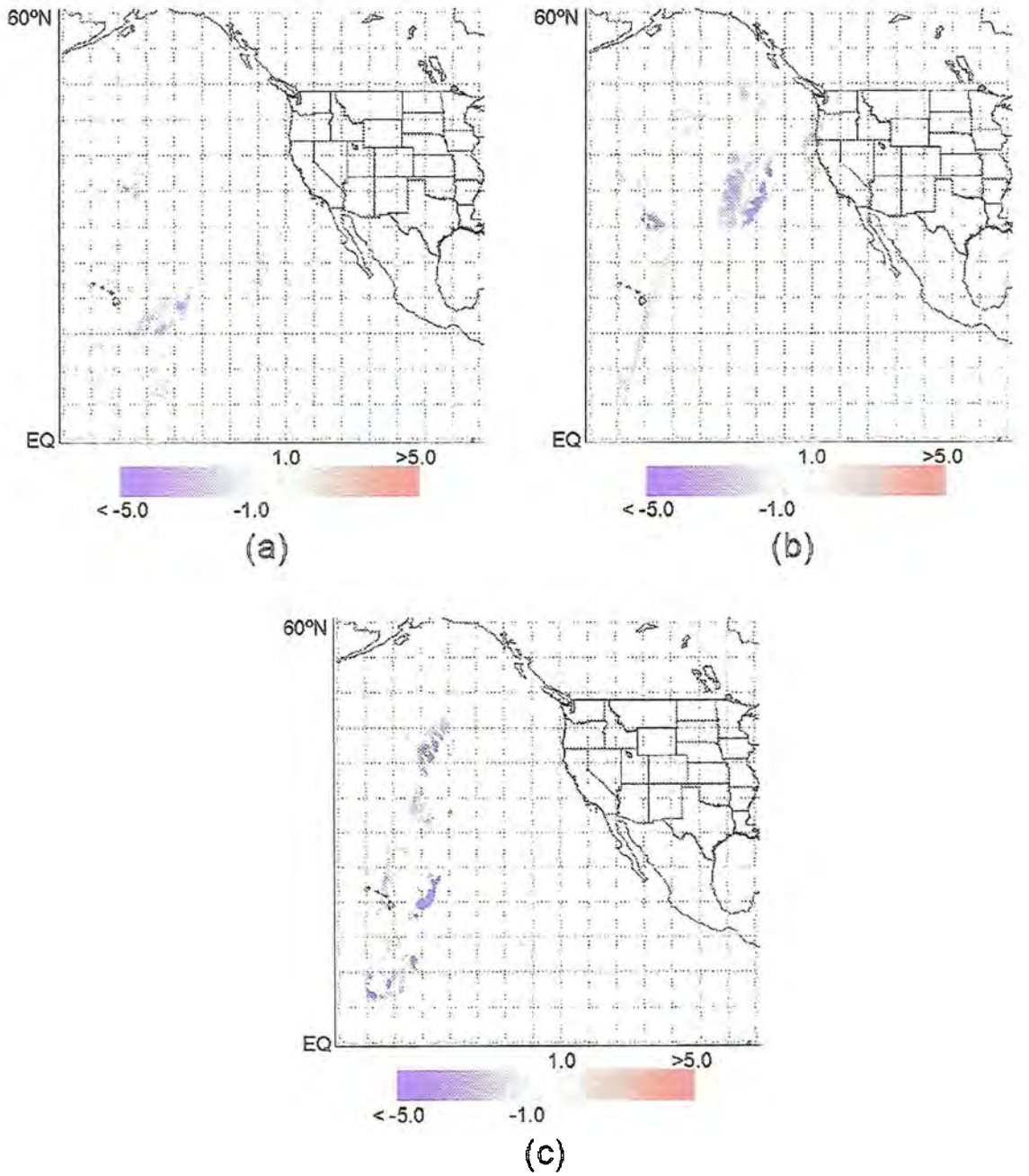

Figure 6.4. Brightness temperature differences (observed – simulated; K) at 92 GHz for March 25, 1996 (a), February 8, 1996 (b), and January 1, 1996 (c).

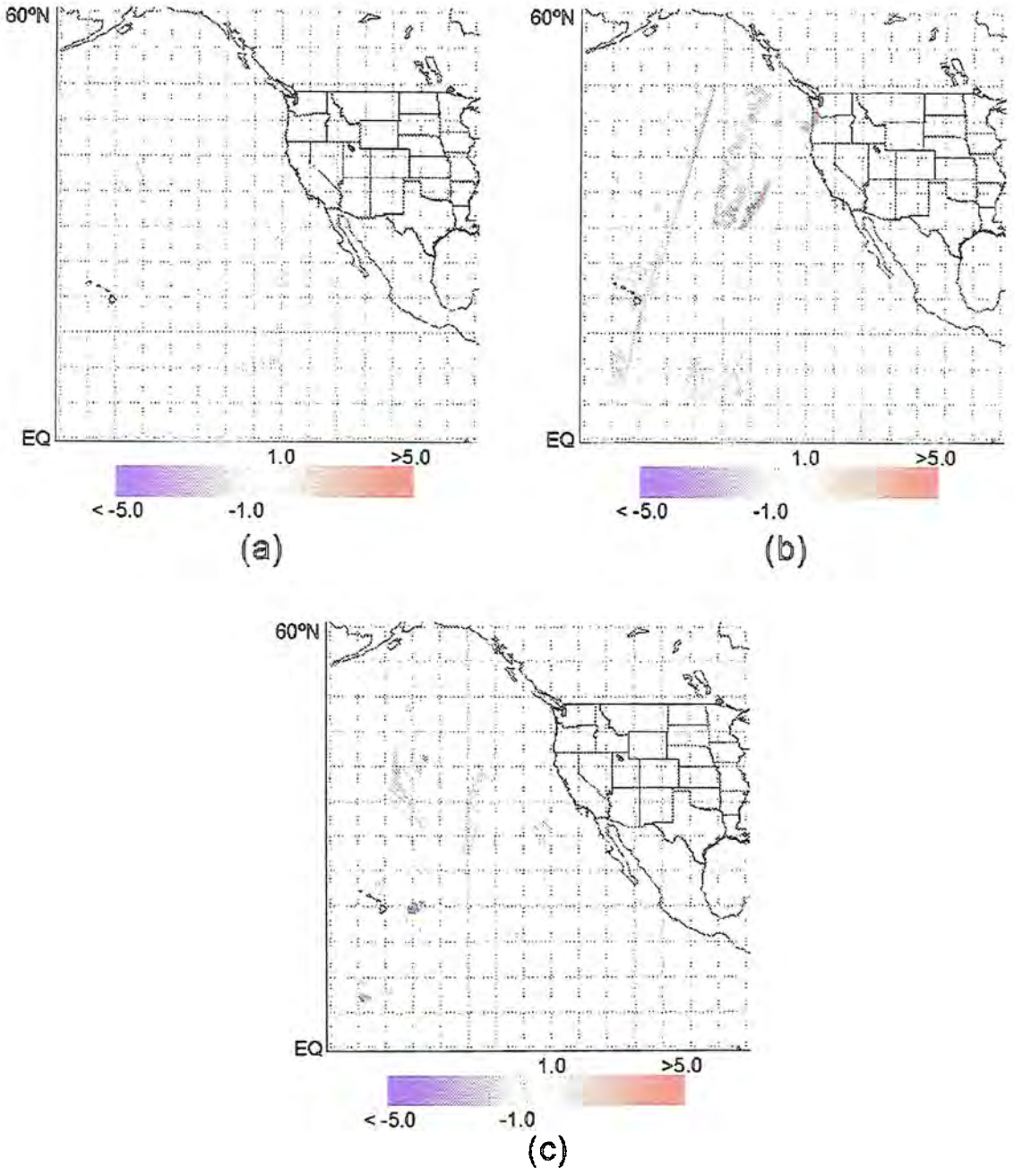

Figure 6.5. Same as Figure 6.4, except for 150 GHz.

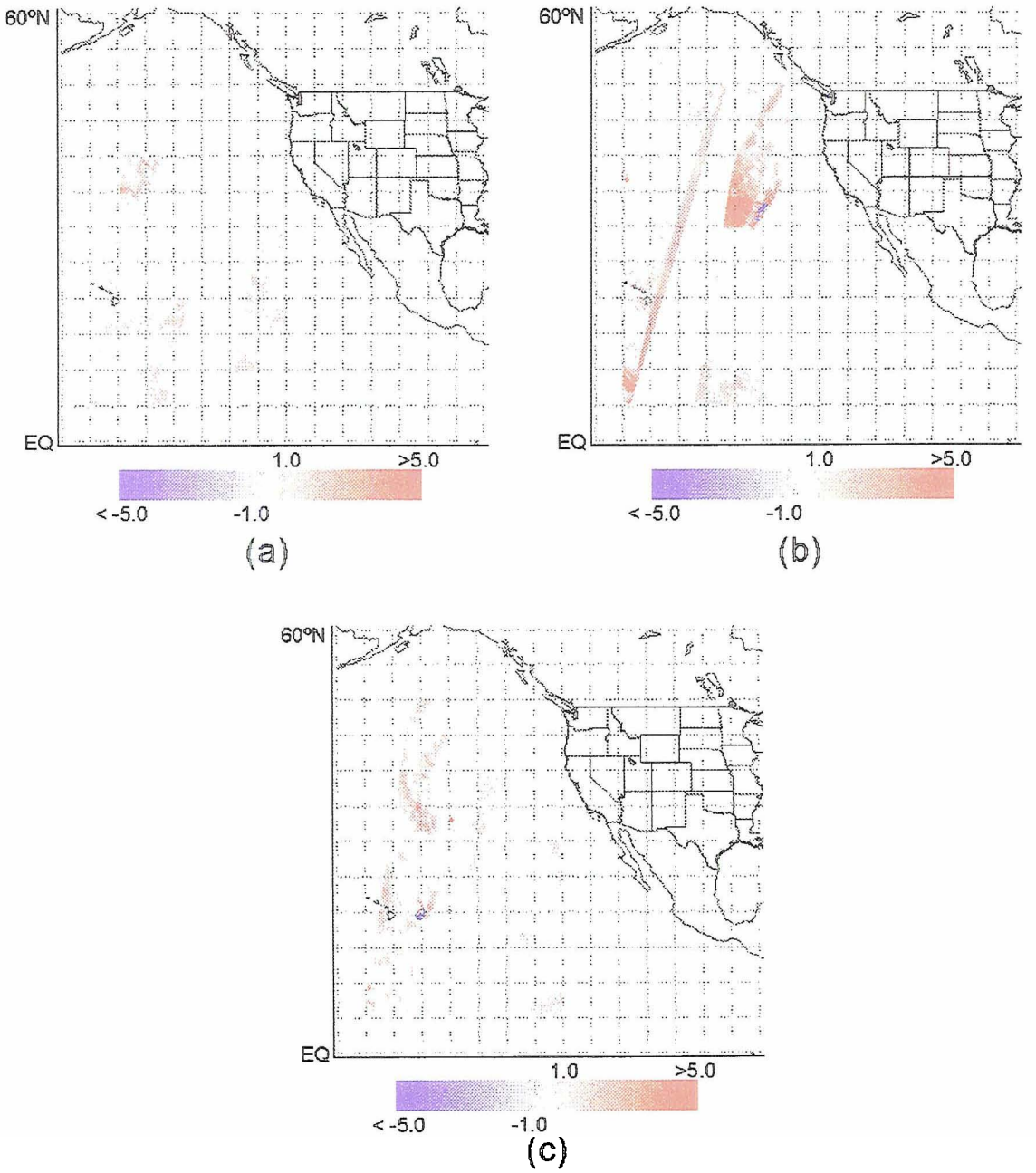

Figure 6.6. Same as Figure 6.4, except for 183 ± 1 GHz.

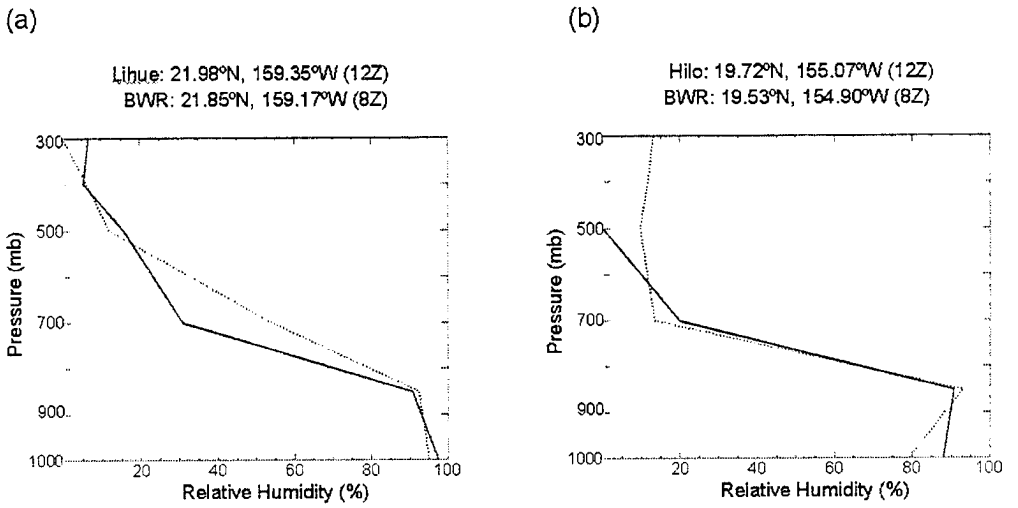

Figure 6.7. Comparisons of the vertical relative humidity profiles from BWR (solid) and rawinsonde (dashed) at the BWR-retrieved atmospheric levels for April 3, 1995 (a) and January 7, 1996 (b).

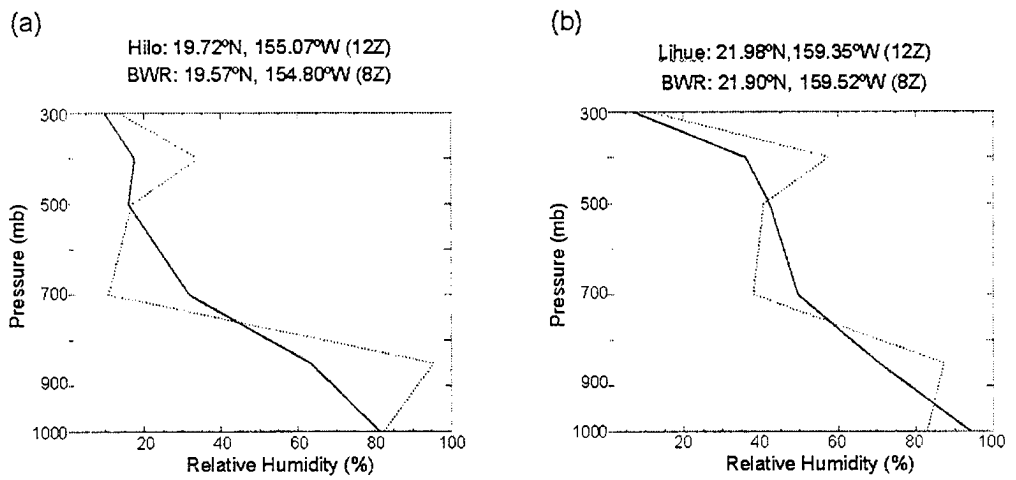

Figure 6.8. Same as Figure 6.7, but for the February 8, 1996 subtropical plume. Comparisons are made with Hilo, HI (a) and Lihue, HI (b).

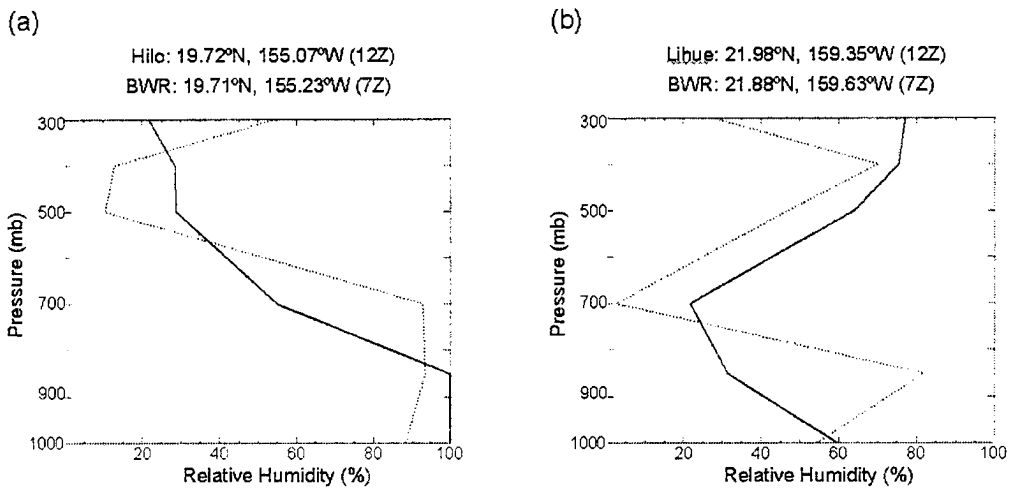

Figure 6.9. Same as Figure 6.7, but for a tropical-polar plume that occurred on February 19, 1996. Comparisons are made with Hilo, HI (a) and Lihue, HI (b).

(a)

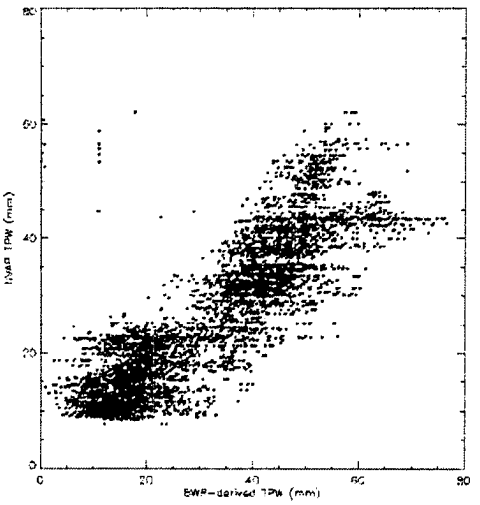

r = 0.84

RMS difference (BWR-NVAP) = 10.0

(b)

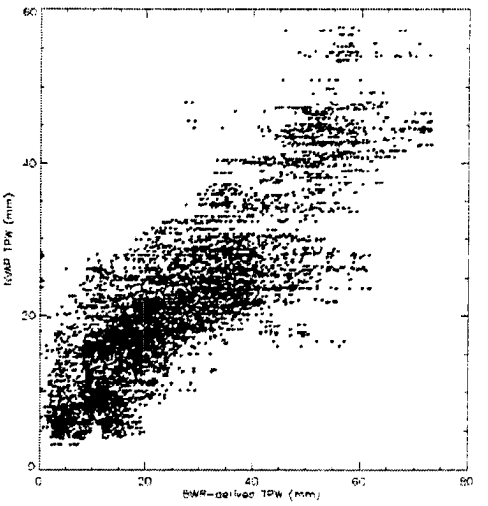

r = 0.85

RMS difference (BWR-NVAP) = 9.4

(c)

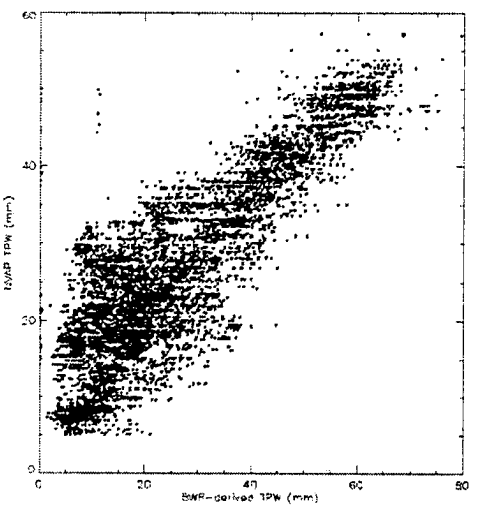

r = 0.84

RMS difference (BWR-NVAP) = 9.1

Figure 6.10. Scatter plots of NVAP total precipitable water (TPW) vs. BWR-derived TPW for March 25, 1996 (a), February 8, 1996 (b), and January 1, 1996 (c). The root-mean-square difference of the two datasets (BWR – NVAP; mm) and the correlation coefficient are also provided.

7. Conclusions and Suggested Future Research

Moisture plumes are a relatively common occurrence in the eastern Pacific Ocean basin. Eastern Pacific moisture plumes are most common during the winter and spring months and do occasionally impact the west coast of North America. The ultimate goal of this study was to get a preliminary picture of the role moisture plumes play in the general circulation and, more specifically, the transport of moisture from the tropics and subtropics. A better understanding of these characteristics would significantly aid in forecasting moisture plume events.

Moisture plumes are seen on satellite imagery as long bands of mid- to high-level clouds. Based on satellite imagery, three classes of moisture plumes were defined for this study: classic, subtropical, and tropical-polar plumes. Generally, plumes (all classes) were more frequent in the western part of the study region (140°W-170°W). A marked difference in plume activity was noted between the January-February and March-April periods, particularly for classic plumes. It would be desirable to look at more years of satellite imagery to see if the aforementioned patterns are indeed real.

Previous studies have noted a decrease in tropical plume activity during El Niño events. In possible support of this observation, the present study noted a decrease in tropical plume (classic + tropical-polar) activity in the January-April 1997 period. The 1997-1998 El Niño event was developing at this time. However, more conclusive results

might be obtained by looking at moisture plume activity during the 1997-1998 winter itself.

Satellites are an important means of obtaining observational data across oceanic regions. Other observational datasets (e.g. surface observations) in these regions are scarce and do not provide adequate spatial coverage. The present study is an application of BWR, a microwave-based retrieval algorithm. Based on Bayes' theorem, this algorithm utilizes microwave brightness temperatures from the SSM/T-2 satellite. The algorithm is used in this study to investigate moisture plumes occurring during the January-April period of the years 1995-1997. Thirty moisture plume case studies were examined, ten for each of the three aforementioned plume classes.

Previous applications of BWR for moisture retrievals have been primarily in tropical environments. Some modifications were made to the prior information used by the algorithm in an attempt to better represent the climatological conditions of the subtropics and midlatitudes. Using NCEP reanalysis data (2.5° latitude-longitude grid), the temperature and relative humidity prior information was, in essence, allowed to vary as a function of space and time. Monthly prior mean and covariance datasets were produced for each position in the NCEP reanalysis grid. For a given retrieval location, the prior information was obtained for the corresponding 2.5° NCEP box.

The BWR algorithm retrieves relative humidity at six atmospheric levels, along with liquid and ice cloud properties. These data were used to determine the spatial distribution of moisture, and corresponding moisture transports, within moisture plumes. These two areas of research have received very little attention in previous studies. Concerning spatial moisture distribution, a few common features were noted in most of the case studies. Deep moisture, often extending up to 300 mb or higher, is found along the main plume axis. Results indicated that both liquid and ice cloud are often found in these regions of deep moisture. To the south and east of the moisture plume, increased

moisture is found primarily in the upper levels of the troposphere. This moist layer often overlies dryer air at middle levels, and appears to be accompanied by ice cloud. In the cloud-free (ignoring low-level stratus) regions just to the north and west of the main plume axis, substantial drying was indicated throughout the retrieved atmospheric column. There were exceptions to this overall structure, however. This was particularly true with some of the profiles obtained for the subtropical plume case studies. For instance, in some profiles, moisture was confined primarily to the lower levels of the retrieved atmospheric column.

The relative humidity data obtained by BWR for each of the thirty case studies was then used to conduct an introductory investigation of the moisture transport characteristics of moisture plumes. Generally, it was found that moisture transport is greatest between 500-850 mb. This result, along with the spatial moisture characteristics discussed earlier, suggests that moisture plumes are a feature whose effects are felt primarily in the middle and upper levels of the troposphere. The magnitudes of moisture transport were found to be greater at all levels for the moisture plumes that originated in the tropics (< 15°N): classic and tropical-polar plumes. This trend is especially evident at 300 mb and 400 mb, where BWR-retrieved moisture indicates very dry conditions for some of the subtropical plume case studies. Total tropospheric moisture transport values for the thirty moisture plume cases were also analyzed. Mean transport values were generally around $2X10^5$-$3X10^5$ $gm^{-1}s^{-1}$, although maximum transports occasionally exceeded 10^6 $gm^{-1}s^{-1}$. These values were compared to the average total tropospheric transports occurring during the winter along the midlatitude baroclinic zone. It was found that the average transports within moisture plumes were generally larger, but within the same order of magnitude. A preliminary conclusion from these results is that moisture plumes have a role in the transport of atmospheric moisture comparable to that of midlatitude frontal systems, particularly with poleward moisture transport.

Several tests were performed to access the overall performance of the BWR algorithm. The retrieval probability indices provide an indirect way to measure the retrieval performance. Generally, a decreased performance was seen in those areas in which the algorithm indicated significant liquid cloud and/or ice cloud. These are often regions where liquid and/or ice precipitation may be occurring. . It is believed that the BWR algorithm does not properly handle the effects of precipitating clouds and multi-layered clouds. The BWR routine attempts to account for both 1) the absorption of microwave radiation by atmospheric gases and liquid water, and 2) ice scattering of microwave radiation. However, the algorithm is currently designed to retrieve only in cloud-free areas and areas with non-precipitating clouds. There is no built-in routine to account for liquid or ice precipitation. Also, the algorithm only allows for a single liquid cloud layer and a single ice cloud layer, a scenario that will often not be representative of actual conditions. Future work should modify the BWR routine to better account for precipitation effects and multi-layered clouds.

For several moisture plumes that passed over Hawaii, BWR-derived relative humidity profiles were compared to nearby rawinsonde relative humidity profiles. These comparisons showed relatively good agreement (within 10-20%) between the two datasets in conditions with little upper-level moisture. When upper-level moisture was present, however, the agreement between the two datasets decreased substantially (with differences up to 50%). In those places where there was satisfactory agreement, the moistening/drying trends indicated by the rawinsonde profiles were also seen in the BWR profiles, albeit at greatly reduced amplitudes. The moisture minima/maxima in the BWR profiles were either at or somewhat below (about 100-200 mb) the corresponding minima/maxima in the rawinsonde profiles.

It would be advantageous to investigate moisture plume activity over a longer study period (more years). First, a longer study period would allow one to better define the

winter patterns of moisture plume activity, removing as much short-term noise as is possible. A second reason for a longer study period is that there would be more case studies with which to develop composites of moisture plumes. From these composites, it might be possible to better define the general moisture characteristics of the plumes. Also, the use of longer datasets would allow for the study of variations in plume activity with the ENSO cycle.

This study indicates that the BWR algorithm performs satisfactorily in extratropical regions. The performance of the algorithm is generally good in cloud-free conditions. However, in conditions where thick cloudiness and/or precipitation exist, modifications must be made to BWR. The most crucial modifications should allow BWR to better account for the effects of precipitation and multi-layered clouds. Also, the BWR could be modified to use input data from the AMSU microwave sensors, which have better horizontal resolution than the SSM/T-2 sensor. This would allow one to better capture horizontal variations in moisture fields.

8. References

Anderson, R. K., and V. J. Oliver, 1970: Some Examples of the Use of Synchronous Satellite Pictures for Studying Changes in Tropical Cloudiness, *Proc. Symp. On Tropical Meteorology*, Honolulu, Amer. Meteor. Soc., E XII 1-6.

Bjerknes, J., 1966: A possible response of the atmospheric Hadley circulation to equatorial anomalies of ocean temperature, *Tellus*, **18**, 820-829.

Bolton, D., 1980: The computation of equivalent potential temperature,*Mon. Wea. Rev.*, **108**, 1046-1053.

Coe, T. E., 1992: Modeling TOVS Radiance of Synoptic Systems, M.S. Thesis, Texas A&M University, 178 pp.

De Felice, P., and A. Viltard, 1976: Aerojet subtropical d'hiver et nuages associes, *La Meteorol., VI Serie*, **6**, 223-225.

Falcone, V. J., and co-authors, 1992: SSM/T-2 calibration and validation data analysis, Environmental Research Papers, No. 111, PL-TR-92-2293, 108 pp.

Forsythe, J. M., personal communication, June, 1999.

Greenwald, T. J., S. A. Christopher, and J. Chou, 1997: SSM/I and GOES-8 imager comparisons of cloud liquid water path over water: Assessment of sub-field of view effects in microwave retrievals, *J. Geophys. Res.*, **102**, 19585-19586.

Hill, H. W., 1969: A synoptic study of a large-scale meridional trough in theTasman Sea-New Zealand area, *New Zealand Journal of Science*, **12**, 576-593.

Iskenderian, H., 1995: A 10-Year Climatology of Northern Hemisphere Tropical Cloud Plumes and Their Composite Flow Patterns, *J. Climate*, **8**, 1630-1637.

Jones, A. S., and T. H. Vonder Haar, 1989: Microwave remote sensing of cloud liquid water and surface emittance over land regions, CIRA paper, Cooperative Institute for Research in the Atmosphere, Colorado State University, Fort Collins, Colorado, 145 pp.

Keen, R. A., 1985: Tropical convection and North American cyclones during the 1982-83 El Niño, *Proc. Ninth Annual Climate Diagnostics Workshop*, Corvallis, NOAA, U.S. Dept. Commerce, Washington, DC, 341-345.

Kiladis, G. N., 1985: A study of tropical-extratropical interaction associated with equatorial convection, Ph.D. Dissertation, University of Colorado, 133 pp.

Kininmonth, W. R., 1983: Variability of rainfall over northern Australia, *Variations in the Global Water Budget*, Riedel, 265-272.

Kuhnel, I., 1989: Tropical-Extratropical Cloudband Climatology Based on Satellite Data, *Intl. J. Climate*, **9**, 441-463.

Lee, T., 1995: Images of Precipitation Signatures from DMSP SSM/T-2, SSM/I, and OLS, *J. Appl. Meteor.*, **34**, 788-793.

Leute IV, F. A., and G. L. Stephens, 1993: An Analysis of Simulated and Actual SSM/T-2 Brightness Temperatures, Atmospheric Science Paper No. 533, Department of Atmospheric Science, Colorado State University, Fort Collins, CO, 99 pp.

Liebmann, B., and D. L. Hartmann, 1984: An Observational Study of Tropical-Midlatitude Interaction on Intraseasonal Time Scales during Winter, *J. Atmos. Sci.*, **41**(23), 3333-3350.

Lietzke, C. E., 1998: Satellite moisture profiling of the tropical eastern Pacific convergence zone, Ph.D. Dissertation, Colorado State University, 126 pp.

Lietzke, C. E., personal communication, January, 1999.

Lietzke, C. E., C. Deser, and T. H. Vonder Haar, 2000: Evolutionary structure of the eastern Pacific double ITCZ based on satellite moisture profile retrievals, submitted to *J. Climate*.

Lim, H., and C. P. Chang, 1987: On the dynamics of midlatitude-tropical interactions and the winter monsoon, in Chang, C. P., and T. N. Krishnamurti (eds.), *Monsoon Meteorology*, Oxford University Press, UK, pp. 405-434.

McGuirk, J. P., A. H. Thompson, and N. R. Smith, 1987: Moisture bursts over the tropical Pacific Ocean, *Mon. Wea. Rev.*, **115**, 787-798.

McGuirk, J. P., A. H. Thompson, and J. R. Schaefer, 1988: An Eastern Pacific Tropical Plume, *Mon. Wea. Rev.*, **116**, 2505-2521.

McGuirk, J. P., and D. J. Ulsh, 1990: Evolution of Tropical Plumes in VAS Water Vapor Imagery, *Mon. Wea. Rev.*, **118**, 1758-1766.

McGuirk, J. P., 1993: Impact of Increased TOVS signal on the NMC Global Spectral Model: A Tropical-Plume Case Study, *Mon. Wea. Rev.*, **121**, 695-712.

Mecikalski, J. R., and G. J. Tripoli, 1998: Inertial Available Kinetic Energy and the Dynamics of Tropical Plume Formation, *Mon. Wea. Rev.*, **126**, 2200-2216.

Peixoto, J. P., and A. H. Oort, 1992: *Physics of Climate*. American Institute of Physics Press, 520 pp.

Philander, S. G., 1990: *El Niño, La Niña, and the Southern Oscillation*. Academic Press, 293 pp.

Press, W. H., S. A., Teukolsky, W. T. Vetterling, and B. P. Flannery, 1992: *Numerical Recipes in FORTRAN: the art of scientific computing.* Cambridge University Press, UK.

Randel, D. L., T. H. Vonder Haar, M. A. Ringerud, G. L. Stephens, T. J. Greenwald, and C. L. Combs, 1996: A New Global Water Vapor Dataset. *Bull. Amer. Meteor. Soc.*, **77**(6), 1233-1246.

Rasmussen, E. M., and P. A. Arkin, 1993: A global view of large-scale precipitation variability, *J. Climate*, **6**, 1495-1522.

Rex, D. F., 1952: Blocking action in the middle troposphere and its effects upon regional climate II: The climatology of blocking action. *Tellus*, **2**, 275-301.

Riehl, H., 1950: On the Role of the Tropics in the General Circulation of the Atmosphere, *Tellus*, **2**(1), 1-17.

Sautter, D. C., 1988: Synoptic-Scale East Asian Cold Surge-Induced Phenomena, M.S. Thesis, Texas A&M University, 104 pp.

Schaefer, J. R., 1985: Observing the Synoptic Structure of Two Moisture Bursts, M.S. Thesis, Texas A&M University, 145 pp.

Schroeder, T. A., 1983: The Subtropical Jet Stream and Severe Local Storms--A View from the Tropics, *Preprints: 13th Conference on Severe Local Storms*, Tulsa, Amer. Met. Soc., 161-162.

Smith, N. R., 1986: A Climatology of Tropical Moisture Bursts in the Eastern North Pacific Ocean, M.S. Thesis, Texas A&M University, 77 pp.

Stockton, J. R., 1986: The Structure of a Late-Spring Moisture Burst,M.S. Thesis, Texas A&M University, 90 pp.

Thepenier, R., and D. Cruette, 1981: Formation of Cloud Bands Associated with the American Subtropical Jet Stream and Their Interaction with Midlatitude Synoptic Disturbances Reaching Europe, *Mon. Wea. Rev.*, **109**, 2209-2220.

Thiao, W., R. A. Scofield, and J. Robinson, 1993: The relationship between water vapor plumes and extreme rainfall events during the summer season, NOAA Technical Report NESDIS 67, 69 pp.

Thompson, A. H., and J. P. McGuirk, 1987: Application of Satellite Data to Tropic-Subtropic Moisture Coupling, NASA Contractor Report 4092, 116 pp.

Ulsh, D. J., 1988: Moisture Burst Structure in Satellite Water Vapor Imagery, M.S. Thesis, Texas A&M University, 101 pp.

Webster, P. J., and M. Dong, 1992: The structure of low frequency phenomena in the tropics and its interaction with the extratropics, *Advances in Atmospheric Sciences*, **9**(1), 1-16.

Zwatz-Meise, W., and G. Hailzl, 1980: Interpretation of so-called shear bands in satellite images, *Arch. Meteor. Geophys. Bioclimatol, Ser. B*, **28**, 299-315.

Appendix – 1: Statistical summaries of moisture plume case studies

Table A.1. Summary statistics of cloud liquid water (gm^{-3}) for all of the case studies.

		Maximum	Mean	Standard Dev.	Coeff. of Variance
Classic	3/18/95	1.04	0.09	0.16	1.71
	4/27/95	1.38	0.09	0.16	1.74
	4/29/95	1.09	0.06	0.13	2.32
	1/23/96	0.69	0.11	0.10	0.89
	1/25/96	0.92	0.13	0.15	1.11
	1/28/96	0.91	0.06	0.10	1.75
	2/25/96	1.10	0.13	0.14	1.14
	3/4/96	1.14	0.09	0.14	1.47
	3/25/96*	0.45	0.07	0.09	1.44
	3/28/96	0.90	0.09	0.15	1.54
Subtropical	3/10/95	1.36	0.17	0.24	1.42
	3/13/95	1.45	0.15	0.29	1.96
	4/3/95	1.22	0.11	0.22	1.93
	4/9/95	1.52	0.19	0.32	1.65
	1/5/96	1.25	0.17	0.23	1.38
	1/7/96	1.38	0.11	0.20	1.89
	1/31/96	0.24	0.03	0.04	1.40
	2/8/96*	1.33	0.18	0.29	1.60
	4/6/96	1.35	0.16	0.30	1.85
	4/14/96	1.68	0.14	0.29	2.02
Trop.-polar	3/7/95	1.31	0.15	0.19	1.30
	1/1/96*	1.22	0.13	0.22	1.65
	1/10/96	1.25	0.23	0.30	1.27
	1/23/96	1.25	0.13	0.17	1.32
	1/25/96	1.28	0.15	0.19	1.29
	1/28/96	1.28	0.15	0.23	1.49
	1/29/96	1.34	0.16	0.19	1.21
	2/19/96	1.09	0.12	0.19	1.66
	2/21/96	1.00	0.12	0.18	1.49
	3/8/96	1.13	0.09	0.18	1.92

Table A.2. Same as Table A.1, except for cloud ice water (gm^{-3}).

		Maximum	Mean	Standard Dev.	Coeff. of Variance
Classic	3/18/95	0.60	0.06	0.10	1.77
	4/27/95	0.60	0.04	0.06	1.61
	4/29/95	0.60	0.05	0.08	1.77
	1/23/96	0.60	0.03	0.07	2.09
	1/25/96	0.60	0.04	0.07	1.59
	1/28/96	0.60	0.04	0.06	1.60
	2/25/96	0.60	0.03	0.04	1.30
	3/4/96	0.60	0.05	0.09	1.86
	3/25/96*	0.55	0.03	0.05	1.56
	3/28/96	0.60	0.05	0.09	1.83
Subtropical	3/10/95	0.60	0.05	0.06	1.13
	3/13/95	0.52	0.03	0.04	1.44
	4/3/95	0.22	0.02	0.02	1.36
	4/9/95	0.60	0.03	0.06	1.81
	1/5/96	0.60	0.03	0.06	2.15
	1/7/96	0.60	0.04	0.06	1.63
	1/31/96	0.29	0.06	0.05	0.71
	2/8/96*	0.60	0.02	0.05	2.13
	4/6/96	0.60	0.03	0.07	2.03
	4/14/96	0.58	0.03	0.06	2.08
Trop.-polar	3/7/95	0.60	0.06	0.10	1.63
	1/1/96*	0.60	0.03	0.06	2.07
	1/10/96	0.60	0.03	0.07	2.59
	1/23/96	0.60	0.04	0.08	2.08
	1/25/96	0.60	0.02	0.06	2.66
	1/28/96	0.60	0.05	0.08	1.71
	1/29/96	0.60	0.04	0.05	1.29
	2/19/96	0.60	0.02	0.05	2.50
	2/21/96	0.60	0.02	0.05	1.90
	3/8/96	0.60	0.05	0.09	1.70

Table A.3. Summary stats. of 1000-mb moisture transport ($gkg^{-1}ms^{-1}$) for all cases.

		Maximum	Mean	Standard Dev.	Coeff. of Variance
Classic	3/18/95	182.08	82.59	46.62	0.56
	4/27/95	133.42	49.96	28.97	0.58
	4/29/95	162.21	56.05	30.66	0.55
	1/23/96	156.38	75.10	33.44	0.45
	1/25/96	201.63	107.80	54.59	0.51
	1/28/96	276.51	143.09	69.65	0.49
	2/25/96	190.21	89.49	44.72	0.50
	3/4/96	178.57	45.81	34.41	0.75
	3/25/96*	217.03	61.12	29.75	0.49
	3/28/96	149.45	55.56	32.53	0.59
Subtropical	3/10/95	154.65	44.19	33.91	0.77
	3/13/95	148.51	36.86	32.80	0.89
	4/3/95	200.98	49.99	38.13	0.76
	4/9/95	116.45	36.40	22.74	0.62
	1/5/96	106.04	30.65	20.81	0.68
	1/7/96	78.17	19.44	13.28	0.68
	1/31/96	154.40	71.15	37.89	0.53
	2/8/96*	155.40	42.66	32.38	0.76
	4/6/96	112.77	40.25	22.33	0.55
Trop.-polar	4/14/96	98.80	32.18	16.75	0.52
	3/7/95	154.46	41.18	26.88	0.65
	1/1/96*	128.16	30.52	22.01	0.72
	1/10/96	145.83	26.98	17.76	0.66
	1/23/96	133.37	33.96	29.26	0.86
	1/25/96	187.05	49.64	33.88	0.68
	1/28/96	206.57	43.51	34.22	0.79
	1/29/96	182.84	52.28	39.39	0.75
	2/19/96	119.18	43.29	23.92	0.55
	2/21/96	156.50	62.03	37.88	0.61
	3/8/96	157.61	38.05	32.20	0.85

Table A.4. Same as Table A.3, except for 850-mb moisture transport ($gkg^{-1}ms^{-1}$).

		Maximum	Mean	Standard Dev.	Coeff. of Variance
Classic	3/18/95	129.48	51.07	30.22	0.59
	4/27/95	300.98	50.22	41.28	0.82
	4/29/95	351.06	92.15	74.48	0.81
	1/23/96	264.55	72.84	41.39	0.57
	1/25/96	175.93	83.98	42.77	0.51
	1/28/96	227.36	80.66	65.64	0.81
	2/25/96	232.98	84.32	36.87	0.44
	3/4/96	227.73	52.64	36.32	0.69
	3/25/96*	224.71	89.10	38.75	0.43
	3/28/96	256.76	54.82	31.24	0.57
Subtropical	3/10/95	184.98	49.47	34.50	0.70
	3/13/95	228.60	30.64	34.33	1.12
	4/3/95	261.40	49.60	39.59	0.80
	4/9/95	115.32	41.25	23.34	0.57
	1/5/96	248.92	47.94	47.20	0.98
	1/7/96	129.99	27.09	23.54	0.87
	1/31/96	170.90	84.01	46.84	0.56
	2/8/96*	253.92	57.78	47.78	0.83
	4/6/96	102.86	37.46	19.21	0.51
Trop.-polar	4/14/96	96.85	28.81	18.24	0.63
	3/7/95	253.89	48.01	34.42	0.72
	1/1/96*	198.10	38.06	26.87	0.71
	1/10/96	135.52	27.87	17.67	0.63
	1/23/96	115.54	32.12	25.21	0.79
	1/25/96	255.90	55.77	46.73	0.84
	1/28/96	198.61	44.83	34.44	0.77
	1/29/96	183.91	51.21	36.93	0.72
	2/19/96	216.57	65.57	34.56	0.53
	2/21/96	212.44	77.10	49.09	0.64
	3/8/96	227.07	45.12	44.16	0.98

Table A.5. Same as Table A.3, except for 700-mb moisture transport ($gkg^{-1}ms^{-1}$).

		Maximum	Mean	Standard Dev.	Coeff. of Variance
Classic	3/18/95	74.61	23.08	12.41	0.54
	4/27/95	198.00	46.29	25.65	0.55
	4/29/95	226.45	65.79	42.26	0.64
	1/23/96	124.22	33.14	24.65	0.74
	1/25/96	145.99	52.57	26.57	0.51
	1/28/96	218.26	51.72	48.49	0.94
	2/25/96	140.28	33.96	25.98	0.77
	3/4/96	238.15	57.73	43.45	0.75
	3/25/96*	210.28	51.57	42.40	0.82
	3/28/96	127.07	36.84	23.68	0.64
Subtropical	3/10/95	111.28	27.92	19.49	0.70
	3/13/95	98.44	36.92	20.33	0.55
	4/3/95	125.69	37.69	24.01	0.64
	4/9/95	168.01	44.84	31.58	0.70
	1/5/96	124.43	20.29	16.73	0.82
	1/7/96	102.04	21.52	19.74	0.92
	1/31/96	81.38	34.45	19.52	0.57
	2/8/96*	276.69	50.74	50.44	0.99
	4/6/96	272.16	58.82	53.48	0.91
Trop.-polar	4/14/96	134.10	31.35	30.19	0.96
	3/7/95	167.91	47.67	33.46	0.70
	1/1/96*	201.42	40.14	32.13	0.80
	1/10/96	108.38	21.22	16.14	0.76
	1/23/96	174.33	40.92	33.69	0.82
	1/25/96	139.58	30.89	24.82	0.81
	1/28/96	157.43	39.30	31.27	0.80
	1/29/96	162.12	27.27	26.84	0.98
	2/19/96	240.43	78.03	40.66	0.52
	2/21/96	239.07	62.92	53.01	0.84
	3/8/96	253.05	38.79	46.67	1.20

Table A.6. Same as Table A.3, except for 500-mb moisture transport ($gkg^{-1}ms^{-1}$).

		Maximum	Mean	Standard Dev.	Coeff. of Variance
Classic	3/18/95	116.74	24.39	21.54	0.88
	4/27/95	152.36	30.36	25.69	0.85
	4/29/95	87.36	34.08	19.17	0.56
	1/23/96	124.37	23.40	18.54	0.79
	1/25/96	100.14	22.96	20.46	0.89
	1/28/96	91.15	17.89	15.18	0.85
	2/25/96	139.46	24.51	22.10	0.90
	3/4/96	217.04	43.11	48.71	1.13
	3/25/96*	193.43	56.30	53.54	0.95
	3/28/96	105.73	34.28	28.42	0.83
Subtropical	3/10/95	43.45	10.10	9.77	0.97
	3/13/95	81.12	17.21	14.45	0.84
	4/3/95	84.63	19.50	14.52	0.74
	4/9/95	139.89	15.83	17.74	1.12
	1/5/96	46.93	5.06	6.31	1.25
	1/7/96	62.37	7.77	11.60	1.49
	1/31/96	125.87	17.63	28.17	1.60
	2/8/96*	161.70	25.27	28.48	1.13
	4/6/96	123.89	23.67	25.94	1.10
Trop.-polar	4/14/96	105.82	20.32	23.06	1.13
	3/7/95	159.04	35.46	35.98	1.01
	1/1/96*	118.28	23.96	21.32	0.89
	1/10/96	93.64	12.19	12.84	1.05
	1/23/96	178.10	35.49	33.66	0.95
	1/25/96	110.45	22.85	20.47	0.90
	1/28/96	112.33	28.15	25.67	0.91
	1/29/96	115.34	18.64	25.15	1.35
	2/19/96	232.59	68.16	51.08	0.75
	2/21/96	206.18	56.37	51.31	0.91
	3/8/96	165.56	25.06	42.70	1.70

Table A.7. Same as Table A.3, except for 400-mb moisture transport ($gkg^{-1}ms^{-1}$).

		Maximum	Mean	Standard Dev.	Coeff. of Variance
Classic	3/18/95	62.50	11.11	13.35	1.20
	4/27/95	53.34	13.25	13.73	1.04
	4/29/95	55.02	16.17	14.46	0.89
	1/23/96	45.22	7.38	9.15	1.24
	1/25/96	79.25	9.13	13.46	1.47
	1/28/96	34.51	9.18	8.16	0.89
	2/25/96	57.55	12.61	11.62	0.92
	3/4/96	120.11	14.75	19.46	1.32
	3/25/96*	136.89	33.06	37.08	1.12
	3/28/96	78.79	23.30	19.21	0.82
Subtropical	3/10/95	11.33	0.68	1.51	2.21
	3/13/95	23.82	2.49	3.45	1.39
	4/3/95	55.61	5.90	6.67	1.13
	4/9/95	59.07	3.53	5.97	1.69
	1/5/96	10.25	0.95	1.38	1.46
	1/7/96	28.40	1.35	3.10	2.29
	1/31/96	42.10	4.31	10.02	2.33
	2/8/96*	45.35	6.62	7.67	1.16
	4/6/96	31.09	4.70	5.10	1.09
Trop.-polar	4/14/96	41.41	7.21	9.02	1.25
	3/7/95	130.73	15.83	24.42	1.54
	1/1/96*	48.57	7.67	9.53	1.24
	1/10/96	50.19	3.85	5.67	1.47
	1/23/96	116.55	11.61	16.97	1.46
	1/25/96	55.24	9.35	9.84	1.05
	1/28/96	61.59	9.62	10.77	1.12
	1/29/96	57.00	6.75	10.78	1.60
	2/19/96	133.10	31.94	24.80	0.78
	2/21/96	98.04	23.94	17.62	0.74
	3/8/96	60.82	6.40	11.04	1.72

Table A.8. Same as Table A.3, except for 300-mb moisture transport ($gkg^{-1}ms^{-1}$).

		Maximum	Mean	Standard Dev.	Coeff. of Variance
Classic	3/18/95	21.14	6.25	5.77	0.92
	4/27/95	29.30	6.34	7.45	1.18
	4/29/95	39.58	9.93	9.38	0.94
	1/23/96	26.14	3.49	4.86	1.39
	1/25/96	45.21	4.78	7.37	1.54
	1/28/96	26.26	5.75	5.49	0.96
	2/25/96	32.22	7.87	8.41	1.07
	3/4/96	54.87	7.29	9.39	1.29
	3/25/96*	62.82	13.15	14.87	1.13
	3/28/96	50.16	13.76	11.03	0.80
Subtropical	3/10/95	8.85	0.28	0.75	2.70
	3/13/95	14.88	0.79	1.32	1.68
	4/3/95	40.62	3.92	5.87	1.50
	4/9/95	18.29	1.66	2.06	1.24
	1/5/96	5.73	0.41	0.61	1.48
	1/7/96	26.91	0.83	1.78	2.14
	1/31/96	29.48	1.74	5.24	3.02
	2/8/96*	21.06	3.87	4.51	1.17
	4/6/96	24.33	2.12	2.28	1.08
Trop.-polar	4/14/96	29.25	4.74	5.27	1.11
	3/7/95	55.85	5.89	10.66	1.81
	1/1/96*	26.58	3.40	5.29	1.56
	1/10/96	20.15	1.85	2.55	1.38
	1/23/96	59.54	5.42	9.16	1.69
	1/25/96	30.02	5.44	6.04	1.11
	1/28/96	27.16	4.08	5.95	1.46
	1/29/96	21.57	2.09	3.80	1.81
	2/19/96	43.37	12.39	9.16	0.74
	2/21/96	42.06	12.30	7.71	0.63
	3/8/96	22.40	2.09	3.23	1.54

Table A.9. Moisture transport over tropospheric column ($gm^{-1}s^{-1}$).

		Maximum	Mean	Standard Dev.	Coeff. of Variance
Classic	3/18/95	$4.70*10^5$	$2.52*10^5$	$9.81*10^4$	0.39
	4/27/95	$7.80*10^5$	$2.69*10^5$	$1.01*10^5$	0.38
	4/29/95	$9.53*10^5$	$3.86*10^5$	$1.64*10^5$	0.42
	1/23/96	$7.66*10^5$	$2.88*10^5$	$1.15*10^5$	0.40
	1/25/96	$6.39*10^5$	$3.76*10^5$	$1.32*10^5$	0.35
	1/28/96	$1.05*10^6$	$4.00*10^5$	$2.36*10^5$	0.59
	2/25/96	$7.18*10^5$	$3.33*10^5$	$1.08*10^5$	0.32
	3/4/96	$9.59*10^5$	$3.08*10^5$	$1.57*10^5$	0.51
	3/25/96*	$1.13*10^6$	$4.10*10^5$	$2.40*10^5$	0.59
	3/28/96	$7.49*10^5$	$2.88*10^5$	$1.13*10^5$	0.39
Subtropical	3/10/95	$5.39*10^5$	$1.84*10^5$	$8.60*10^4$	0.47
	3/13/95	$5.14*10^5$	$1.76*10^5$	$1.01*10^5$	0.58
	4/3/95	$6.69*10^5$	$2.29*10^5$	$1.18*10^5$	0.52
	4/9/95	$6.02*10^5$	$2.06*10^5$	$1.09*10^5$	0.53
	1/5/96	$5.23*10^5$	$1.49*10^5$	$1.02*10^5$	0.69
	1/7/96	$4.56*10^5$	$1.12*10^5$	$7.21*10^4$	0.65
	1/31/96	$5.39*10^5$	$2.91*10^5$	$1.21*10^5$	0.41
	2/8/96*	$1.10*10^6$	$2.65*10^5$	$2.07*10^5$	0.78
	4/6/96	$7.95*10^5$	$2.40*10^5$	$1.52*10^5$	0.63
Trop.-polar	4/14/96	$5.38*10^5$	$1.71*10^5$	$1.20*10^5$	0.70
	3/7/95	$1.02*10^6$	$2.68*10^5$	$1.44*10^5$	0.54
	1/1/96*	$7.10*10^5$	$2.03*10^5$	$1.21*10^5$	0.60
	1/10/96	$4.45*10^5$	$1.29*10^5$	$7.12*10^4$	0.55
	1/23/96	$7.76*10^5$	$2.19*10^5$	$1.52*10^5$	0.70
	1/25/96	$6.67*10^5$	$2.35*10^5$	$1.31*10^5$	0.56
	1/28/96	$6.62*10^5$	$2.33*10^5$	$1.29*10^5$	0.55
	1/29/96	$6.96*10^5$	$2.13*10^5$	$1.31*10^5$	0.62
	2/19/96	$1.06*10^6$	$4.16*10^5$	$1.88*10^5$	0.45
	2/21/96	$1.12*10^6$	$4.02*10^5$	$2.14*10^5$	0.53
	3/8/96	$8.92*10^5$	$2.18*10^5$	$1.65*10^5$	0.76